UNIVERSITY OF OKLAHOMA

GRADUATE COLLEGE

INVESTIGATIONS OF CARTILAGE LUBRICITY AND INTERACTIONS BETWEEN CARBON NANOTUBES AND PHOSPHOLIPID BILAYERS

A DISSERTATION

SUBMITTED TO THE GRADUATE FACULTY

in partial fulfillment of the requirements for the

Degree of

DOCTOR OF PHILOSOPHY

By

LIU SHI
Norman, Oklahoma
2012

INVESTIGATIONS OF CARTILAGE LUBRICITY AND INTERACTIONS BETWEEN CARBON NANOTUBES AND PHOSPHOLIPID BILAYERS

A DISSERTATION APPROVED FOR THE
SCHOOL OF CHEMICAL, BIOLOGICAL AND MATERIALS ENGINEERING

BY

_____
Dr. Alberto Striolo, Chair

_____
Dr. Brian P. Grady

_____
Dr. Rong Gan

_____
Dr. Edgar A. O'Rear

_____
Dr. Vassilios I. Sikavitsas

This dissertation is dedicated to my parents, Zhongyan Shi and Ruizhi Sun, who have supported me all the way since the beginning of my studies.

Also, this dissertation is dedicated to my wife, Nina Xu, who has been a great source of motivation and inspiration.

Acknowledgements

The completion of my Ph.D would not have been possible without the help and support of many people.

First and foremost I want to thank my advisor Dr. Alberto Striolo, who has not only guided me and taught me a lot to complete my academic research, but also helped me to grow as an independent thinker. My experience at the University of Oklahoma would have not been the same without his guidance.

I also want to express my gratitude to Dr. Brian P. Grady, Dr. Rong Gan, Dr. Edgar A. O'Rear and Dr. Vassilios I. Sikavitsas for serving in my committee. I appreciate the time they dedicated to me, and their suggestions for a successful dissertation.

In addition, I would like to thank Dr. Daniel E. Resasco, Dr. Matthias U. Nollert and all other professors for providing access to the laboratory instruments and valuable discussions.

A special thank goes to Greg Strout and Dachuan Shi for their continuous support of freeze-fracture transmission electron microscope experiments.

Finally, I would like to thank all other members of Dr. Striolo's group for teaching me valuable knowledge about simulation.

This research work would not have been feasible without the financial support by National Science Foundation (NSF), by the Oklahoma Center for the Advancement of Science and Technology (OCAST), by the Oklahoma Regents for Higher Education, and by the Vice President for Research at the University of Oklahoma. I also want to thank the generous allocations of computing time provided by the OU Supercomputing

Center for Education and Research (OSCER) in Norman, Oklahoma and the National Energy Research Scientific Computing Center (NERSC) in Berkeley, California.

Table of Contents

List of Tables

List of Figures

Abstract

Because one of the principal functions of articular cartilage in joints is to provide support in diarthrodial joints, transmitting loads with minimum friction and wear, it is likely that understanding the lubrication mechanism in articular cartilage will lead to therapeutic strategies to relieve mild symptomatic osteoarthritis, and possibly to improve the efficacy and expected lifetime of prosthetic implants. For this reason, we used a pin-on-disc tribometer to measure the friction coefficient of both pristine and mechanically damaged cartilage samples in the presence of different lubricant solutions. We find that the experimental set-up allows us to assess different lubrication mechanisms active in cartilage. Among the lubricants considered, 100mg/ml of 100,000 Da polyethylene oxide (PEO) in phosphate buffered saline (PBS) appears to be as effective as synovial fluid (SF), especially on the mechanically-damaged cartilage. It is possible that the viscosity of the lubricant enhances cartilage lubrication via the interstitial fluid pressurization mechanism, maximized by the experimental set up adopted in our friction tests.

We also conducted experiments to investigate how single walled carbon nanotubes (SWNTs) interact with phospholipid membranes. The work will both contribute to prevent adverse health effects due to SWNTs, and enable the applicability of SWNTs in advanced scientific areas such as controlled drug delivery, tissue (i.e., cartilage) culture and regeneration, and/or cancer therapy. Our primary results suggest that the presence of liposomes can keep SWNTs dispersed in water at low surfactant concentration. It is likely that individual or slightly bundled SWNTs interact with

phospholipid membranes without significant disruption of the structure of phospholipid bilayer.

1. Introduction

Diarthrodial joints, such as the knee and elbow, consist of bone, articular cartilage, ligaments, tendons, muscle and the joint capsule. The surfaces of the two bones at the diarthrodial joints are covered by articular cartilage. The purpose of this tissue is to provide a suitable surface for lubrication and wear prevention. The full structured cartilage is composed of collagen type II (10-20%), water and electrolytes (68-85%), proteoglycans (5-10%), and chondrocytes.[1] In a simplistic description, cartilage can be understood as a sponge in which the solid, highly charged phase provides support and confines the fluid phase within small cavities. The pore sizes in the cartilage are different. The effective pore size is in the range of 2.0-6.5 nm.[2]

Cartilage has a heterogeneous structure divided in four layers: the superficial tangential zone (STZ) with 10-20% of the cartilage thickness, the middle zone with ~60% of the cartilage thickness, the deep zone with ~30% of the cartilage thickness, and the calcified cartilage zone where the cartilage interfaces with the bone. Cartilage tissues in the four zones differ in collagen organizations as well as in the amounts of proteoglycans. A schematic diagram of these zones is shown in Figure 1-1. The STZ zone is the thinnest zone of articular cartilage. It provides a smooth surface for the two bones to slide against each other. It is composed of flattened chondrocytes. Of all the layers, it has the highest concentration of collagen and the lowest concentration of proteoglycans, making it very resistant to shear stresses. The collagen fibers in the STZ of the cartilage have the orientation parallel to the surface and perpendicular to the deeper zones. Below the STZ layer is the middle layer, which is mechanically designed

to absorb shocks and distribute the load efficiently. The middle layer is composed of rounded chondrocytes. The collagen fibers are arranged randomly, and the proteoglycan content increases. In the deep zone, the chondrocytes tend to line up in columns parallel to the collagen fibers and the cell volume is at its lowest. The water level is the lowest. The collagen fibers in the deep zone are nearly perpendicular to the interface. The deepest layer is the calcified zone which anchors the articular cartilage to the bone. The collagen fibers in this zone are arranged perpendicular to the articular surface and linked to a calcified matrix.

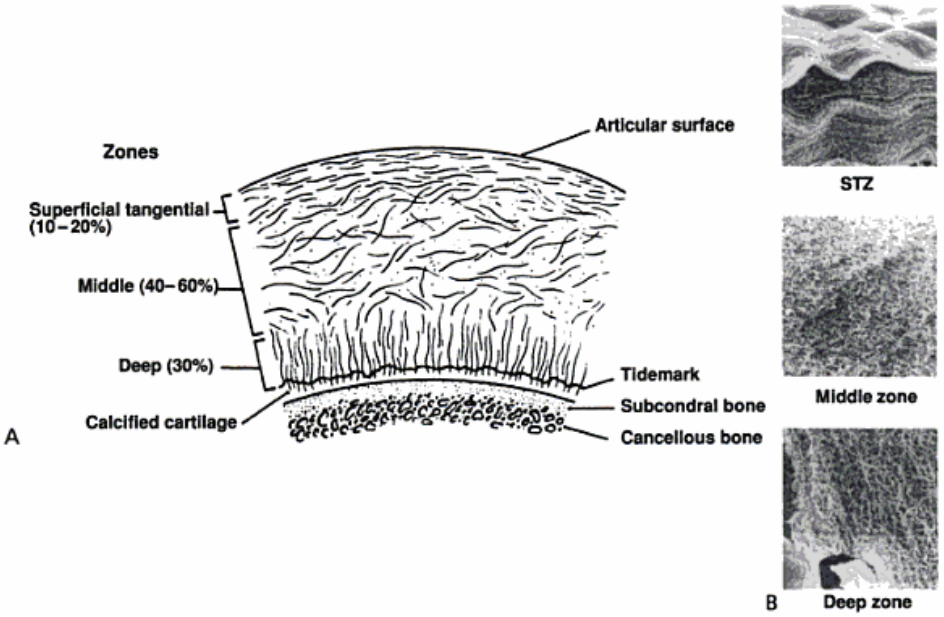

Figure 1-1 Schematic diagram of articular cartilage showing zone structures (A). Corresponding scanning electron microscopy collagen fibrillar arrangement (B). Figure is reproduced from Ref.[1]

There is no blood supply to the articular cartilage. Articular cartilage receives oxygen and other nutrients mainly from the surrounding joint fluid. When the load is

applied on a joint, the interstitial fluid containing waste products is squeezed out of cartilage and when the load is removed, the synovial fluid (SF) with nutrients and oxygen flows back into articular cartilage. Unfortunately, once articular cartilage is injured, cartilage has very limited ability to regenerate by itself.

SF is important in diarthrodial joint. It is secreted by synovial lining cells. One of its main functions is to provide nutrients and remove catabolic products. SF is also crucial to joint lubrication and bearing functions.[3-6] It has been shown that SF can reduce friction coefficient of cartilage effectively and afford wear protection to the cartilages. The most abundant macromolecules in SF are hyaluronic acid (HA), which is a high molecular weight anionic polysaccharide with the molecular weight from several thousands to more than 3 MDa, phospholipids, chondroitin sulfate and lubricin or called superficial zone protein (SZP). Studies have shown non-Newtonian behavior of SF. Early rheological studies of SF focused on its shear thinning property which is majorly due to the presence of high molecular weight HA. However, recent studies have shown that SF is rheopectic (i.e. the longer the fluid undergoes shearing force, the higher it viscosity).[7, 8] It is suggested that during shearing, the continuous protein network form, and this network is responsible for the observed rheopexy.

Osteoarthritis (OA) is a degenerative joint disease characterized by four main anatomical lesions: degenerative cartilage lesion (ulcerations tending ultimately to nude bone); proliferative lesion of the periosteum (bone osteophytes); degenerative bone lesion (subchondral bone sclerosis and subchondral bone lysis), and inflammatory lesion of the articular soft tissues (synovial effusion, oedema and progressive periarticular fibrosis). OA can be caused by intrinsic factors (primary OA), which have

a genetic and/or biomechanical etiology, as well as extrinsic causes (secondary OA), which are caused by external factors, such as direct trauma, overuse or repetitive motion injuries, corticosteroids, obesity, and/or ligamentous injuries, leading to joint hypermobility and instability.[9] Representative human knee joints with OA are shown in Figure 1-2. OA affects nearly 5 percent of the general population and 80 percent of people over the age of 65,[10] with 27 million patients in the US alone.[11] It is estimated that OA is the highest cause of work loss in the US. Because one of the principal functions of cartilage is to provide support in diarthrodial joints, transmitting loads with minimum friction and wear,[12] it is likely that understanding the lubrication mechanism in cartilage will lead to therapeutic strategies to relieve mild symptomatic OA, and possibly to improve the efficacy and expected lifetime of prosthetic implants. For this reason understanding the frictional properties of cartilage continues to be of enormous interest.

(a)

(b)

Figure 1-2 Representative human knee joints with early stage of osteoarthritis (a) and end-stage osteoarthritis (b). Figure is reproduced from Ref.[3]

Experiments have reported extremely low friction coefficients of joint articular cartilage, confirming that cartilage is a weight-bearing and wear-resistant natural tissue.[13] To interpret the low friction coefficient of cartilage, a number of hypotheses have been proposed, including boundary lubrication,[14-17] hydrodynamic,[18] elasto-

hydrodynamic,[19] squeeze-film,[20-22] weeping,[15, 23], boosted mechanisms,[24] and interstitial fluid pressurization.[2, 25-32]

In boundary lubrication, an extremely thin layer, perhaps one molecule thick, between the bearing cartilage surfaces holds the surface projections slightly apart. A boundary lubricant is typically a molecule that coats the surface of a bearing and produces low friction due to molecular-molecular repulsive forces. Recent results suggest phospholipids and lubricins in the SF are likely to be boundary lubricants for cartilage.[6, 33, 34]

Hydrodynamic lubrication is a way to achieve extended fluid pressure to hold up the body weight and separate the joint surfaces by using parallel rather than perpendicular to the motion between them. As one surface moves across the other, friction between adjacent fluid molecules drags the intervening fluid into the space between them, creating hydrodynamic pressure that forces them apart. The friction force essentially depends on the fluid properties.[35] Elasto-hydrodynamic refers to the situation in which the bearing surfaces have a low elastic modulus (e.g. soft articular cartilage), so that they deform significantly under the pressures produced in the lubricating fluid as it passes over them.[36]

The high viscosity of SF seemingly makes SF an ideal candidate for a lubricant, which is thought to keep the articular surfaces from touching directly by providing an intervening fluid film, pressurized by the entraining velocity of the joint surfaces. For example, when a person runs and swings his/her leg forward, the joint is minimally loaded, allowing the cartilage surfaces to separate and minimizing the friction. When the leg is on its stance phase, body weight pushes the femoral condyles down through

the SF toward the tibial side of the joint. When the contact is made, frictional forces greatly increase. The viscosity of the fluid resists the descending femur and increases the amount of time required for the two sides of the joint to meet. In the meantime, friction remains low. The bearing surface separation produced by such load and unload cycles is called squeeze-film lubrication.[31, 35] The squeeze-film thicknesses between cartilage disc and a rigid counterface under stationary load can be predicted by a simplified equation:[37]

$$h = a^2 \sqrt{\frac{3\pi\eta}{4Wt}} \tag{1-1}$$

In Eq. (1-1), h is the squeeze film thickness; a is contact radius; η is viscosity; W is normal load; t is squeeze film time.

McCutchen proposed that interstitial fluid confined in the cartilage got pressurized as a result of joint compressive loading, thus weeping out of the cartilage to maintain a fluid film layer between the cartilage surfaces. This weeping of fluid under pressure was hypothesized to contribute to separation of the joint surfaces, which is known as weeping lubrication mechanism.[15, 23]

Besides squeeze-film and weeping lubrication, Walker et al. proposed the boosted lubrication. Because of the microscopic ridges and groves on the surfaces, when the two cartilage surfaces are pressed together, pools of SF are trapped and fluid is forced back to the cartilage rather than out of the cartilage.[24]

Weeping lubrication is based on the hypothesis that there is a fluid film between the two surfaces. If the cartilage surfaces come to direct contact, the interstitial fluid pressurization inside the cartilage becomes the reason to support most of the contact load.[31] When most of the load is supported by interstitial fluid, only a small fraction

of load would be transferred via solid-solid contact, thus, producing a very low friction coefficient. If the interstitial fluid pressure subsides, the friction coefficient rises considerably, as the entire contact load becomes supported by solid-solid contact. Ateshian et al. related the time-dependent friction coefficient to the interstitial fluid pressurization:[30, 31]

$$\mu_{eff}(t) = \left[1 - (1-\varphi)\frac{W^P(t)}{W(t)}\right]\mu_{eq} \tag{1-2}$$

In Eq. (1-2), $W(t)$ is the applied load and $W^P(t)$ is the load supported by the interstitial fluid, hence $W^P(t)/W(t)$ is the fraction of the load supported by the interstitial fluid; φ is the fraction of the cartilage surface that is solid and provides contact between two sliding surfaces; $\mu_{eff}(t)$ is the time-dependent friction coefficient; μ_{eq} is the friction coefficient at 'steady-states', achieved after the two surfaces slide on each other for a long time.

Although many lubrication hypotheses have been proposed, the lubrication mechanism of cartilage remains not completely understood. Some of hypotheses even conflict with each other. At this point, some fundamental questions have not been answered, such as the manner in which SF acts as such a good lubricant; which components play critical roles in cartilage lubrication properties; what physiological mechanism is responsible for such low friction coefficients of cartilage. Conducting fundamental investigation of the lubricity of articular cartilage with precisely controlled system can be the way to answer such questions. Among the lubrication mechanisms of cartilage, recently results provided more and more evidences that support interstitial fluid pressurization mechanism.[30, 31, 38-40] Especially Morrell et al. demonstrated, using in vivo experiments, the importance of interstitial fluid pressurization in joint

tribology.[41] Our primary hypothesis is that the good lubrication property in natural joints is due to the sustained high interstitial fluid pressure in articular cartilages.

Towards providing additional experimental evidence for the lubricity of cartilage, a number of experiments have been conducted during this thesis. In section 2 and 3, we report experimental results for the friction coefficients of both pristine and mechanically damaged bovine articular cartilages. The mechanically damaged articular cartilages were used, because the damage of cartilage likely leads to OA. A pin-on-disc tribometer was employed to study the effects of different testing-configurations on the lubrication mechanisms of articular cartilage. To test the ability of different lubricants to reduce the friction coefficient for articular cartilage, several substances dissolved in the phosphate buffered saline (PBS), as well as SF, were used as lubricants. The friction coefficients obtained from different lubricants were compared to understand the role of each lubricant in joint lubrication. Rheological properties of lubricant solutions were found to be very important in the lubricating process. By systematically altering the composition of the PBS solution we demonstrate the importance of solution viscosity in determining the measured friction coefficient of cartilage.

In the second part of the thesis we studied the interactions between carbon nanotubes (CNTs) and phospholipid bilayers. CNTs, which belong to the carbon allotropes family, are constituted of cylinders of graphene sheets, open or closed at the extremities. CNTs can be either single walled carbon nanotubes (SWNTs), which have diameters in the range of 0.4-2.0 nm and lengths of a few micrometers, or multi-walled carbon nanotubes (MWNTs), which have diameters and lengths up to 100 nm and several micrometers, respectively. Both SWNTs and MWNTs exhibit unique physical,

chemical, and electrical properties that made them an attractive material for electronic applications, medical diagnostics, drug delivery and tissue regeneration.[42, 43]

CNTs are intriguing materials for implantation because they are conductive and have nanostructured dimensions comparable to the dimensions of proteins found in extracellular matrices.[44-46] Recent results have documented that adding CNTs in conventional three-dimensional scaffold can be beneficial for cartilage and bone regeneration.[46-49] MacGinitie et al. suggested that cartilage tissue could be efficiently regenerated when subjected to electrical stimulation.[50] Moreover, cartilage is composed of nanostructured materials (e.g. collagen is a nano-structured protein in cartilage tissue arranged in various ways depending on its location in superficial, middle or deep zones). Thus, combining these two important properties of CNTs (nano-roughness and conductivity) into one single implant may be beneficial for cartilage tissue engineering applications.

However, the enthusiasm for using CNTs in medical applications is mitigated by reports on their toxicity. CNTs exhibit cytotoxicity to both human[51, 52] and animal cells[53, 54]. Besides vitro experiments, Lam et al. conducted experiment in vivo and found that pristine hydrophobic CNTs accumulated in the lungs of rats, and possibly causing granulomas.[53]

As the literature on the subject evolved, experimental results have indicated that the toxicity of CNTs relies on multiple factors, including the purity and the type of CNTs, their functionalization,[54-56] and possibly both cell-culture media and cell type used in the experiments.[57, 58] Crouzier et al.[59] reported that purifying SWNT significantly reduced the lytic effect on red blood cells. Experiments also suggested,

perhaps not surprisingly, that the type of CNT functionalization affected cellular uptake, maybe even changed the uptake mechanism.[60, 61] Singh et al.[62] synthesized twelve polyamine-modified SWNTs and MWNTs, most of which showed reduced cytotoxicity to human lung epithelial A549 cells exposed to the CNTs for 24 and 72 hours. Although chemical functionalization appeared to alleviate the cytotoxicity of CNTs, surfactants may not provide such a benefit. In an interesting comparative study, Liu et al.[63] studied the cytotoxicity of SWNTs to bacteria. They dispersed SWNTs using both the nonionic surfactant Tween 20 and the anionic surfactant sodium cholate (SC). Tween 20 was found not to be cytotoxic, while SC was found to decrease the bacteria survival rate. It would be interesting to understand why chemical functionalization of the CNTs reduces their cytotoxicological properties, while physical functionalization using surfactants does not yield similar effects.

The results summarized above suggest that significant progress is being made in understanding the toxicity of CNTs on living cells. Unfortunately, the phenomenon is still not completely understood and sometimes even contradictory results are reported. Taking the effect of SWNT aggregation on cytotoxicity as an example, Liu et al. reported that individually dispersed SWNTs were more toxic than bundled or aggregated SWNTs;[63] while Mutlu et al. found that the toxicity of SWNTs was attributable to their aggregation.[64]

As a first step towards addressing the possible interactions between CNTs and living cells from a fundamental point of view, we have implemented a minimal model within which we investigate interactions between CNTs and phospholipid bilayers. As our results improve, the lipid bilayers can be enriched by other elements (notable

membrane proteins) to more and more closely represent living organisms. Within this thesis, the model investigated experimentally is minimal, and it only involves bilayers formed by L-α-phosphatidylcholine and cholesterol. We will answer the question: is it possible that SWNTs, dispersed in aqueous solutions, embed into cellular membranes and eventually disrupt them? Understanding how SWNTs interact with phospholipid membranes will both contribute to preventing adverse health effects due to SWNTs, and enable the applicability of SWNTs in advanced scientific areas such as controlled drug delivery, gene therapy, and maybe even tissue regeneration, including cartilage.

It has been convincingly shown that CNTs can cross the cell membrane into cytoplasm, even entering cell nucleus.[57, 61] On the other hand, the mechanisms and pathways CNTs entering cells are not answered. So far, the two most possible uptake pathways that have been suggested based on experimental observations are endocytosis and direct insertion through the lipid bilayer of cell membrane. The endocytosis can be either active (ATP driven) or passive (not involving the cell machinery).[65] In section 4, we describe experiments conducted to study the interaction between SWNTs and liposome membranes. The interactions between liposomes and SWNTs can be a simplified model for better understanding the cell uptake mechanism. Our model can only study the direct insertion or passive endocytosis mechanisms of SWNTs crossing cell membranes, because the active endocytosis is excluded. In the future, other mechanisms will be studied, as the model will be made more complex.

Finally, section 5 summarizes the conclusions from the present body of work and includes recommendations for the future research.

In addition to the material described in the body of the dissertation, during my studies at the University of Oklahoma I have also studied the self-assembly of surfactants at various interfaces. The two publications related to that research are included as appendices to this dissertation.

2. Experimental Friction Coefficients for Healthy Bovine Cartilage Measured with a Pin-On-Disc Tribometer

The material presented below was published in 2011 in volume 39, of the journal 'Annals of Biomedical Engineering'.

2.1 Abstract

The friction coefficient between wet articular cartilage surfaces was measured using a pin-on-disc tribometer adopting different testing-configurations: cartilage-on-pin vs. alumina-on-disc (CA); cartilage-on-pin vs. cartilage-on-disc (CC); and alumina-on-pin vs. cartilage-on-disc (AC). Several substances were dissolved in the phosphate buffered saline (PBS) to act as lubricants: 10,000 molecular weight (MW) polyethylene oxide (PEO), 100,000 MW PEO and chondroitin sulfate (CS), all at 100 mg/ml concentration. Scanning electron microscopy photographs of the cartilage specimens revealed limited wear due to the experiment. Conducting the experiments in PBS we provide evidence according to which a commercial pin-on-disc tribometer allows us to assess different lubrication mechanisms active in cartilage. Specifically, we find that the measured friction coefficient strongly depends on the testing configuration. Our results show that the friction coefficients measured under CC and AC testing configurations remain very low as the sliding distance increases, probably because during the pin displacement the pores present in the cartilage replenish with PBS. Under such conditions the fluid phase supports a large load fraction for long times. By systematically altering the composition of the PBS solution we demonstrate the

importance of solution viscosity in determining the measured friction coefficient. Although the friction coefficient remains low under the AC testing configuration in PBS, 100mg/ml solutions of both CS and 100,000 MW PEO in PBS further reduce the friction coefficient by ~40%. Relating the measured friction coefficient to the Hersey number, our results are consistent with a Stribeck curve, confirming that the friction coefficient of cartilage under the AC testing-configuration depends on a combination of boundary, hydrodynamic and interstitial fluid pressurization lubrication mechanisms.

2.2 Introduction

Osteoarthritis (OA) is a degenerative joint disease characterized by four main anatomical lesions: degenerative cartilage lesion (ulcerations tending ultimately to nude bone); proliferative lesion of the periosteum (bone osteophytes); degenerative bone lesion (subchondral bone sclerosis and subchondral bone lysis), and inflammatory lesion of the articular soft tissues (synovial effusion, oedema and progressive periarticular fibrosis). It affects nearly 5 percent of the general population and 80 percent of people over the age of 65,[10] with 27 million patients in the US alone.[11] Because one of the principal functions of cartilage is to provide support in diarthrodial joints, transmitting loads with minimum friction and wear,[12] it is likely that understanding the lubrication mechanism in healthy cartilage will lead to therapeutic strategies to relieve mild symptomatic osteoarthritis, and possibly to improve the efficacy and expected lifetime of prosthetic implants. For this reason understanding the frictional properties of cartilage continues to be of enormous interest.

Although a number of experimental investigations report extremely low friction coefficients for cartilage, sometimes as low as ~0.01,[13] the physiological mechanism responsible for such low friction coefficients is not completely understood. A number of hypotheses have been proposed, including fluid film lubrication mechanisms in the flavors of hydrodynamic,[18] elasto-hydrodynamic,[19] squeeze-film,[20-22] weeping,[15, 23] and boosted mechanisms,[24] boundary lubrication,[14-17] and biphasic self-generating lubrication.[2, 25-32]

Among many factors that affect the friction coefficient for cartilage, such as sliding velocity, duration of load, loading rate, interfacial contact area, wear and so on, the presence of lubricants appears to be essential to normal functioning of the joints.[33, 66-80] Hyaluronic acid (HA),[67, 81, 82] phospholipids,[33, 34, 82] chondroitin sulfate (CS),[73, 76, 83] lubricin[84-86] – the major components of natural synovial fluid (SF) –and polyethylene oxide (PEO)[76] are reported to reduce the friction coefficient of articular cartilage. Although to explain these observations the boundary lubrication mechanism is often invoked, the mechanism by which each component present in synovial fluid facilitates lubrication, by itself or in combination with other components, is not completely understood. Gleghorn and Bonassar showed that friction coefficients measured under various experimental conditions fall within a universal Stribeck curve, which satisfactorily relates the friction coefficient with sliding speed and normal load.[4] In the classic Stribeck curve, the measured friction coefficient is a function of the Hersey number, $\eta\upsilon/N$, where η is the dynamic viscosity of the lubricant solution, υ is the sliding velocity, and N is the normal load.[87] We are not aware of any systematic study in which the Hersey number is varied by changing the viscosity of the solution in

which the experiments are conducted while keeping all other parameters constant. Some literature reports have however addressed the effect of viscosity on the measured friction coefficients, and somewhat controversial results have been reported. For example, Mori et al. found that very viscous HA lubricant solutions decrease the measured friction coefficient.[81] Others found that the measured friction coefficient does not depend on the solution viscosity.[76] Benz et al. reported that the viscosity of a fluid film containing HA is lower near the cartilage surface than in the bulk, suggesting that HA may not actually adsorb on the cartilage surface.[88] One source of uncertainty may be related to the fact that most fluids in which the friction coefficient for cartilage is measured (e.g., the synovial fluid) are non-Newtonian. Thus the viscosity used for calculating the Hersey number could be either the viscosity at a certain shear rate, or the zero-shear-rate viscosity.[76, 81]

To rationalize these observations it helps remembering that articular cartilage is a complex tissue. Cartilage shows a heterogeneous structure divided in four layers that differ in biochemical composition and molecular organization. The structural integrity of cartilage is probably responsible for its mechanical properties. In a simplistic description, cartilage can be pictured as a sponge in which a solid, highly charged phase provides support and confines a fluid phase within small cavities.[1] When a load is applied to cartilage, the fluid is pumped out of the pores. McCutchen provided evidence suggesting that, while inside the pores, the interstitial fluid contributes to maintain low friction coefficients in cartilage.[15] Hlavacek reported that the fluid escaping the pores yields a film on cartilage that quickly depletes, leaving the bearing surfaces into contact. [21, 22, 38, 40, 89-91] When the fluid film is incomplete, lubrication is provided by the

interstitial fluid. When the fluid film is intact lubrication is provided by fluid-film hydrodynamics. Ateshian et al. related the time-dependent friction coefficient to the interstitial fluid pressurization:[30, 31]

$$\mu_{eff}(t) = \left[1 - (1-\varphi)\frac{W^P(t)}{W(t)}\right]\mu_{eq} \tag{2-1}$$

In Eq. (2-1), $W(t)$ is the applied load and $W^P(t)$ is the load supported by the interstitial fluid, hence $W^P(t)/W(t)$ is the fraction of the load supported by the interstitial fluid; φ is the fraction of the cartilage surface that is solid and provides contact between two sliding surfaces; μ_{eff}(t) is the time-dependent friction coefficient; μ_{eq} is the friction coefficient at 'steady-states', achieved after the two surfaces slide on each other for a long time. The interstitial fluid can support 90% or more of the total normal load ($W^P(t)/W(t)$), depending on the solicitation. This support can reduce to zero under prolonged static loading, at 'steady-states' conditions.

During activities such as walking and running the loading environment in the lower limbs is cyclical, allowing the synovial fluid to support large loads for short intervals and to replenish the cartilage before the load applies again on any contact area.[31, 92] McCutchen reported that allowing a cartilage sample to replenish with synovial fluid for a few seconds was sufficient to restore low friction coefficients.[15] Despite this, many available experimental data are collected under continuous static loads. One exception was reported recently by Caligaris and Ateshian,[39] who built a special tribometer with which they proved that when the contact area between two sliding cartilage surface moves (i.e., 'migrating' contact area), a constant, very low friction coefficient is observed. Measuring friction coefficients under conditions in which the contact area between the cartilage samples migrates is likely to mimic

physiological conditions. Custom-made instruments, such as that designed by Caligaris and Ateshian, are suitable for such experiments, but it is possible that commercial pin-on-disc tribometers can provide the desired experimental conditions under appropriate testing configurations.

The objectives of the present work are (I) to assess whether a commercial pin-on-disc tribometer could be used to assess various lubrication mechanisms in articular cartilage; specifically, we seek to determine whether by changing the experimental set up it is possible to establish experimental conditions under which the contact area, the area on which the external load is applied, migrates on the cartilage substrate; (II) to determine the effect of solution viscosity towards reducing the measured friction coefficient; to this effect we dissolve different polymers in phosphate buffered saline (PBS) solutions; and (III) to interpret our experimental results invoking the interstitial fluid support (time-dependent friction coefficients) and the Stribeck curve (steady-states friction coefficients).

Although it is known that synovial fluid is an efficient lubricant, this fluid is not used in the present work because it was preferred to control the solution composition by carefully measuring the concentration of two compounds (PEO and CS) within PBS solutions. These compounds change the solution viscosity. The effect on the measured friction coefficient of compounds such as lubricin and phospholipids, present in natural synovial fluid, will be considered in future studies.

Our results demonstrate that a commercial pin-on-disc tribometer can be used to measure the friction coefficient for articular cartilage over time under the precise control of sliding velocity and applied load. By controlling the experimental set up we

propose a facile method to systematically probe different lubrication mechanisms. Mature bovine knee cartilage samples can be placed on the pin and/or on the disc, thus our technique is suitable for measuring friction coefficients for cartilage-on-pin vs. alumina-on-disc (CA), cartilage-on-pin vs. cartilage-on-disc (CC) and alumina-on-pin vs. cartilage-on-disc (AC) testing-configurations. In the latter two testing-configurations the contact area migrates on the cartilage surfaces, while the contact area remains constantly loaded in the CA testing configuration. Because configurations with migrating contact areas mimic the physiological cartilage behavior, they should yield low friction coefficients even when the experiments last for long times. In the second part of the paper, using the AC testing configuration we demonstrate the importance of solution viscosity in determining the measured friction coefficient for articular cartilage.

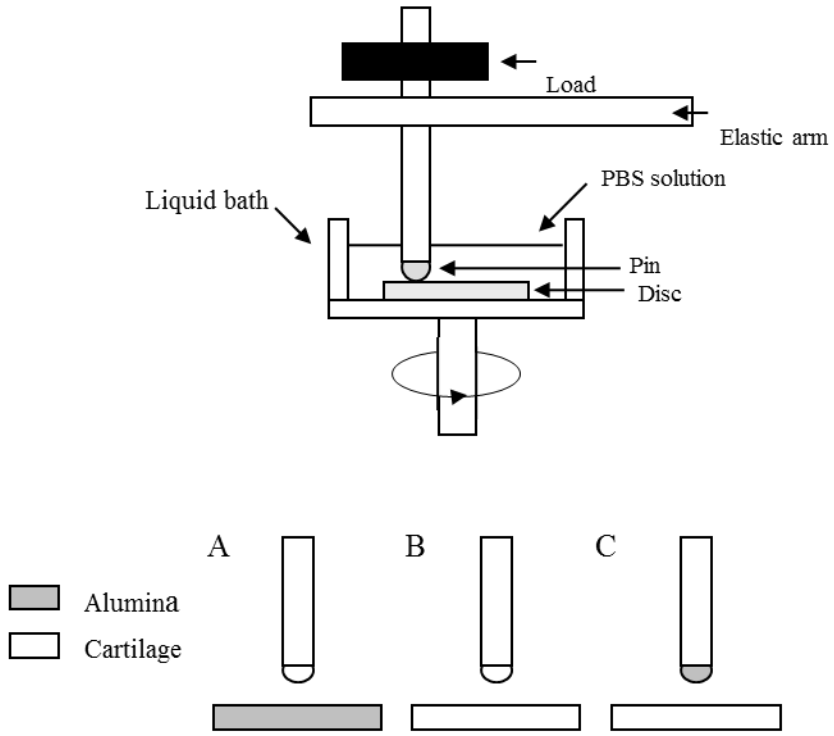

Figure 2-1 Schematic diagram of the pin-on-disc tribometer used in this study (top). The samples were immersed in PBS solutions during the experiment. The disc, together with the liquid bath, rotates with a constant velocity. The friction coefficient between pin and disc is monitored continuously by measuring the deflection of the elastic arm. On the bottom panel three testing configurations are represented: (A) cartilage-on-pin vs. alumina-on-disc (CA); (B) cartilage-on-pin vs. cartilage-on-disc (CC); (C) alumina-on-pin vs. cartilage-on-disc (AC).

2.3 Experimental Procedures

2.3.1 Cartilage Specimen Preparation

Bovine knees of age 15-30 months were purchased from Animal Technologies Inc. They were delivered within 3 days after slaughter. The knees were not frozen but stored at ~4°C until dissection. Although cartilage degrades after slaughtering, scanning

electron microscope images show smooth surface structures, suggesting little, if any, surface cartilage degradation before testing. Full depth osteochondral plugs (Ø=12mm) were harvested from lateral and medial femoral condyles using a scalpel and 12mm biopsy punches. The osteochondral plugs were trimmed to maintain a constant thickness (1.3±0.2mm) by removing the deep zone tissues with a sledge microtome (Leica SM2000 R), leaving the specimen surface intact. The cartilage samples were washed with PBS to remove natural lubricants. After preparation, the specimens were frozen and stored at -20°C in PBS solution (pH=7.4, buffer strength=150mM). To maintain uniformity in our experiments, the osteochondral plugs were further cored out using biopsy punches to reduce the cylindrical cross section to Ø=10mm or Ø=2mm. The Ø=10mm specimens were glued to the disc and those with Ø=2mm were glued to the pins (details below) to perform lubrication experiments.

2.3.2 Lubricants Preparation

Articular joints are naturally immersed in synovial fluid. This fluid is a complex mixture containing hyaluronic acid, lubricin, phospholipids, and other compounds that contribute to lubrication, as well as to other biological functions. When our experiments in the AC testing configuration are conducted for cartilage immersed in natural synovial fluid, steady-states friction coefficients of 0.040±0.004 are obtained under experimental conditions similar to those considered in the present work (sliding speed of 1 mm/s and applied normal load of 2 N). These results are not discussed herein because, in an attempt to better understand the mechanism responsible for the low friction coefficients

typically observed in cartilage, the lubricant composition is controlled as closely as possible, as described below.

In the simplest case, our experiments are conducted with the sliding surfaces immersed in PBS. To test the ability of different lubricants to reduce the friction coefficient for articular cartilage when dissolved in PBS, 4 different aqueous solution groups were prepared. Cartilage samples were immersed in the corresponding solution for 12 hour at 4°C after thawed before testing. The control solution was PBS. The other three solutions were obtained by dissolving 'lubricants' in PBS. The lubricant solutions contained 100mg/ml polyethylene oxide (PEO) of 10,000 molecular weight (MW) (Polymer Source, Inc., Dorval, Quebec, Canada), 100mg/ml PEO of 100,000 MW (Sigma-Aldrich, St. Louis, MO, USA), and 100mg/ml chondroitin sulfate (CS) from shark cartilage (Sigma-Aldrich, St. Louis, MO, USA; CS molecular weight is not known). The 'lubricants' were used as received. A SR5000 stress-controlled rheometer from Rheometric Scientific was used to measure the steady shear rate viscosity of each lubricant solution. The viscosity from each PBS solution was found to be constant over the shear rate range of 10-3000 s^{-1}, indicating that the viscosity reached the zero-shear-rate limit. The zero-shear-rate viscosity of PBS, 10,000 MW PEO, 100,000 MW PEO, and CS solutions at room temperature were found to be 0.88, 3.5, 37.2, and 36cp, respectively (details are reported in Appendix C Figure 7-25). The estimated shear rate during the lubrication experiments is always in the range of 200-5000 s^{-1}, calculated by assuming that the distance between 2 sliding cartilages in 1 μm, which corresponds to the surface roughness of cartilage.[77] The sliding speed of our lubrication experiments

is in the range of 0.2-5mm/s. The viscosities of the 4 lubricant solutions do not change within this range of shear rates.

2.3.3 Experimental Protocol: Friction Coefficient Experiments

The friction coefficient under a continuous static normal load of 2N (corresponding to a nominal contact pressure of 0.63MPa) was measured using a pin-on-disc tribometer (CSM, model S/N 18-312). The contact stress is within the physiological range during human walking activities.[41] A schematic of the experimental set up is shown in Figure 2-1. All the tests began 5 seconds after applying the load. The samples were immersed in a liquid bath during the test. The disc rotated with a constant sliding velocity of 0.2, 0.5, 1 and 5mm/s, depending on the experiment.

Friction coefficients were measured in the cartilage-on-pin vs. alumina-on-disc (CA); cartilage-on-pin vs. cartilage-on-disc (CC); and alumina-on-pin vs. cartilage-on-disc (AC) testing-configurations. A schematic of the three testing-configurations is shown in the bottom panel of Figure 2-1. The alumina disc was aluminum, while the pin was ceramic alumina. All the experiments with lubricants dissolved in PBS were performed under the AC testing-configuration, which, according to our results, better mimics physiological conditions compared to the CA testing configuration.

The friction coefficient between the contact surfaces was monitored continuously by measuring the deflection of the elastic arm that holds the pin. The data were collected as a function of time using the CSM ModelX software with an acquisition frequency of 10Hz. All tests were performed by placing the pin on the disc at a distance r=3±0.05mm from the center of the rotating plate. The experiments performed in PBS

for AC, CC, and AC testing configurations were terminated after 100 laps with a constant sliding speed of 1mm/s, corresponding to a travelled distance of 1885mm. The tests conducted with lubricants (PEO or CS) dissolved in PBS were terminated after 20 laps, corresponding to a travelled distance of 377mm (our results reveal that friction coefficient does not change after 20 laps under the AC testing-configuration). During one lap the friction coefficient shows a cyclic variation, which is due in part to the unevenness of the prepared sample, and, in large part, to intrinsic vibrations experienced by the instrument elastic arm during the operation. The average friction coefficient in each lap is reported in what follows. All experiments were performed at room conditions. For each test the data reported herein are the average from 10 independent measurements conducted at the same conditions.

We measured the contact area in the AC testing configuration by dying the pin (alumina sphere) and then measuring the colored trace on the cartilage glued on the disc. The contact area was found to have an average width of ~2mm. To keep the contact area consistent when experiments are performed on the various testing-configurations of Figure 2-1, we cut the cartilages glued on the pin (alumina sphere) into plugs of diameter 2mm. Because the size of the contact interface, ~2mm, is much smaller than the size of the spherical support on the pin, which has a diameter of 8mm, we can reasonably assume that the contact interfaces are flat for all the cases considered herein. Etsion et al. developed a theoretical model to study the effect of dwell time on the junction growth of a creeping polymer sphere in contact with a rigid flat surface, which may represent a spherical cartilage surface pressed onto a flat metal surface.[93, 94] According to Etsion et al. model, the contact interface does not change during our

experiment, because of the low applied pressures.[41] We also conducted one test experiment under the CA testing configuration in which the cartilage sample was glued on a flat pin. Results did not differ qualitatively from those obtained using a spherical support on the pin.

2.3.4 Cartilage Surface Characterization

Following examples from literature,[95-98] scanning electron microscopy (SEM) has been used to characterize articular cartilage surfaces. Specimens were fixed in 2% glutaraldehyde and 0.1M PBS for 24 hours, following by further fixation in 1% osmium tetroxide for 1.5 hours. Specimens were dehydrated using ethanol and critical-point dried with a Tousimis autosamdri-814 critical point drier. Then the Anatech Ltd. Hummer VI sputtering system was used to coat the cartilage specimen with 8nm of gold. SEM images were obtained using a JEOL JSM-840A instrument before and after conducting our friction-coefficient experiments to visualize and quantify wear.

2.3.5 Data Interpretation

We applied the interstitial fluid pressurization model as proposed by Ateshian and coworkers to analyze our results for the measured time-dependent friction coefficient μ_{eff} under different testing configurations. Although immature bovine specimens were used to derive Eq. (2-1), it should be remembered that McCutchen used mature shoulder leg pig cartilage samples when he originally demonstrated the importance of interstitial fluid support (weeping fluid lubrication).[12] Our hypothesis is that the model can be applied to the friction coefficient measurement for healthy mature bovine cartilage

specimens. Following Torzilli, φ was considered equal to 0.1, corresponding to the solid content of the superficial zone of immature bovine articular cartilage.[99] The model of Eq. (2-1) was proposed to analyze the friction coefficient measured in a friction device with intermittent linear sliding between the surfaces, under constant applied load. This testing-configuration is similar to the CA testing-configuration shown in Figure 2-1. In this work we assume the model of Eq. (2-1) suitable to interpret the friction results obtained using not only the CA but also the CC and AC testing-configurations. The accuracy of this assumption is assessed by comparing our experimental results to model fits.

All quantities in Eq. (2-1) are function of time, except $\mu_{eq.}$ Our experimental set up allows us to measure $\mu_{eff}(t)$ as a function of constant load W. Unfortunately, we have no access to $W^P(t)$,the load supported by the interstitial fluid. However, we observe that according to Eq.(2-1) the measured friction coefficient increases as the load supported by the interstitial fluid W^P decreases. When $W^P = 0$, $\mu_{eff} = \mu_{eq.}$ We assume that μ_{eq} obtained at the end of the CA testing-configuration experiment corresponds to μ_{eq} also for the experiments conducted in the CC and AC testing configurations. Knowing this value, we can calculate $W^P(t)$ by Eq.(2-1) when the experimental $\mu_{eff}(t)$ is known. This procedure seems reasonable for the AC testing configuration, but μ_{eq} is expected to be somewhat lower in the CC configuration because two cartilage surfaces slide on each other.

2.3.6 Statistical Analysis

The mean and standard deviation were calculated and the statistical significance of the differences in friction coefficient was determined. A two-way analysis of variance (ANOVA) with Tukey's HSD post hoc test was used to compare the initial and steady-states friction coefficient values among different testing configurations. The effect of lubricant type and applied speed on the friction coefficient of cartilage was determined by a two-way ANOVA with Tukey's HSD post hoc test. All statistical analyses were carried out using PASW Statistics 18 (SPSS Inc., Chicago, IL); α was set to be 0.05 and the statistical significance was accepted for $p<0.05$.

2.4 Results and Discussions

2.4.1 Surface Characterization of Cartilage

We used SEM to characterize the cartilage surfaces before and after the friction experiment. Figure 2-2 A and B show the 40˚ tilt and top view SEM images of an intact articular cartilage surface, respectively. The images show a smooth cartilage surface with some underlying chondrocytes, indicating a healthy and flat sample. Figure 2-2 C is the top view of a cartilage sample after one experiment conducted in the AC testing configuration. Visual analysis reveals an abrasion on the surface due to the continuous sliding of the alumina ball onto the cartilage sample for 100 laps. The width of the abrasion (~2mm) is consistent with our early estimation. Figure 2-2 D is 40˚ tilt view SEM image at the intact-worn cartilage interface. The left side of this image is the intact cartilage, while the abrasion lies on the right of the broken line. The abrasion visualized

by SEM is very shallow, suggesting that our experiments only produce minor wear on the cartilage samples probably because of the small applied load. All cartilage samples used for our studies appear smooth and healthy suggesting that limited, if any, degradation has occurred before testing. The extent of wear due to conducting our experiments appears limited. This could be further reduced if smooth alumina balls were used for the experiment. Because no experimental observation is available in the literature for cartilage wear under the experimental conditions considered herein, in particular when the AC testing configuration is implemented in a pin-on-disc tribometer, comparison regarding wear results is not possible. For completeness, we point out that when the experiments are conducted for longer times, the extend of wear increases. The cartilage samples eventually degrade if the experiments are conducted for 1 hour or longer. These latter results are strongly dependent on the sample used. Statistical analysis of such results is beyond the scopes of the present work.

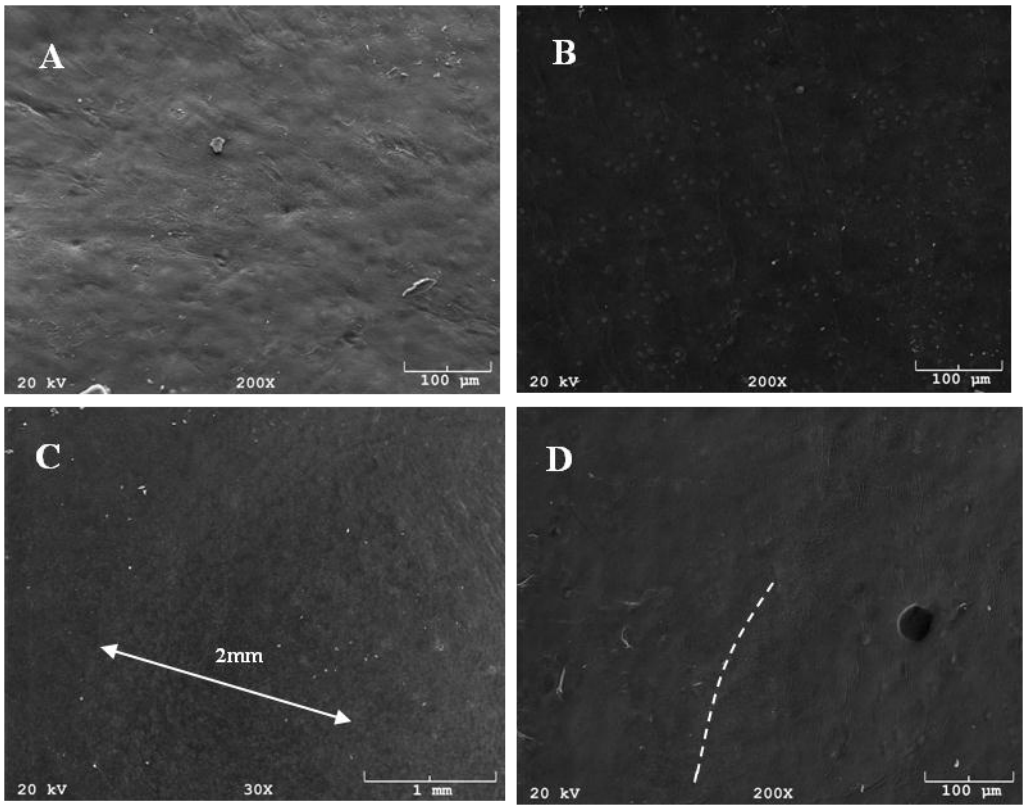

Figure 2-2 SEM images of intact and worn articular cartilage surfaces. A is 40˚ tilt view of untreated cartilage; B is the top view of untreated cartilage; C is top view of the worn area of cartilage after 100 laps; D is the 40° tilt view of the intact-worn interface of cartilage after 100 laps (the intact surface is on the left of the broken line).

To test the effect of unavoidable wear on the friction coefficient measured for cartilage during the experiment, we measured the friction coefficient for each cartilage plug twice under the same testing configuration. In between the two experiments the cartilage plugs were allowed to relax in PBS solution for 2 hours without applied load. The slight wear on the surface during the experiment shown by our SEM results shown in Figure 2-2 was found to have limited effect on the measured friction coefficient. In very rare cases the friction coefficient measured in two experiments on the same

cartilage sample showed large deviations. Data are presented here only if the measured friction coefficients from the two experiments are consistent (±10%).

2.4.2 Testing-Configuration Effects

The experimental results for the friction coefficient and the corresponding fraction of load supported by the interstitial fluid in the CA testing configuration are shown in Figure 2-3. All error bars, not shown in Figure 2-3 to Figure 2-5 for clarity, are included in Table 2-1. The friction coefficient was found to increase with time from a minimum of ~ 0.099±0.014 to a plateau value of ~ 0.271±0.015. The plateau is reached within ~ 750s after starting the experiment. According to the biphasic lubrication model of Eq. (2-1), as the measured friction coefficient increases the fraction of load supported by the interstitial fluid decreases from ~ 71% at the beginning of the experiment to ~0 at the end of it.

In Figure 2-3 we also show the results obtained when a flat pin was used to hold a cartilage sample. These data, represented by the empty triangles, are consistent with those obtained using a sphere to support the cartilage (filled spheres). The only noticeable difference is that the friction coefficient at steady-states is slightly larger on the former than on the latter case. According to results reported by Merkher et al.,[68] this difference is consistent with a slightly larger contact area when the flat pin is used, despite the fact that a cartilage plug of 2 mm diameter was used in both experiments.

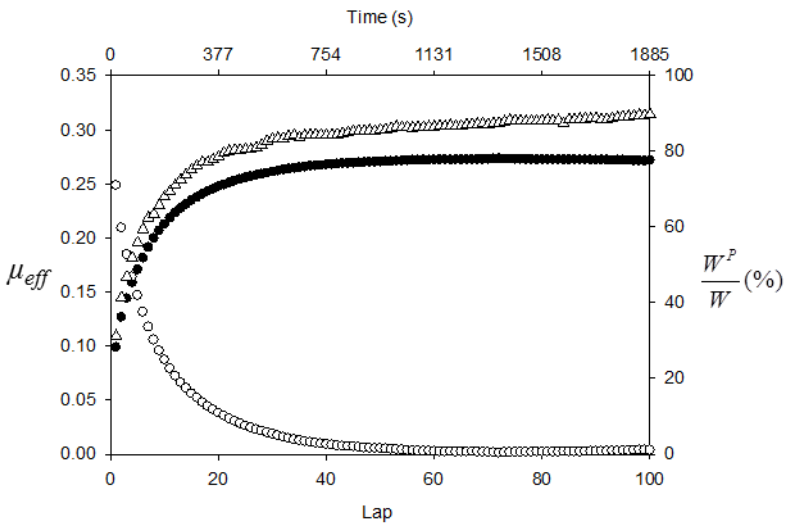

Figure 2-3 Time-dependent friction coefficient, μ_{eff}, and the portion of load supported by interstitial fluid, W^P/W, obtained in the cartilage-on-pin vs. alumina-on-disc testing configuration (see Figure 2-1 for details). During the friction experiment 1885 seconds correspond to a sliding distance of 1.885 m and 100 laps. Filled circles are for the measured friction coefficient; empty circles are for the fraction of load supported by the interstitial fluid. Empty triangles are for the friction coefficient measured when the cartilage was supported by a flat pin. No estimation for the fraction of load supported by the interstitial fluid was attempted in the latter case.

In Figure 2-4 we report the measured friction coefficient, as well as the estimated portion of load supported by interstitial fluid, obtained in the CC testing configuration. The shape of the friction coefficient curve is similar to that obtained under the CA testing configuration. However at steady-sates μ_{eff} (0.071±0.017) is only ~15% larger than at the beginning of the experiment, when μ_{eff} ~ 0.062±0.021. The corresponding fraction of load supported by the interstitial fluid, obtained assuming that μ_{eq} is equal to that measured in Figure 2-3, remains high during the entire experiment. It decays from ~85.7% at the beginning of the experiment to ~82.5% in ~500 s, at steady states.

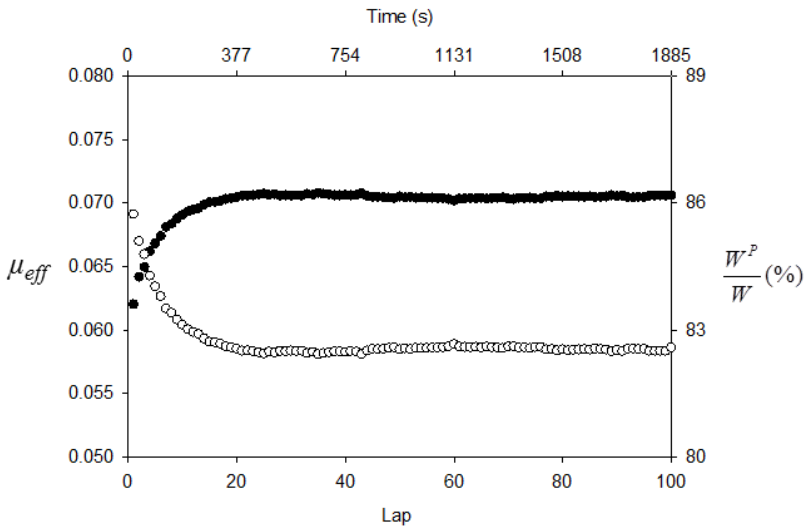

Figure 2-4 Time-dependent friction coefficient, μ_{eff}, and portion of load supported by interstitial fluid, W^P/W, measured in the cartilage-on-pin vs. cartilage-on-disc testing configuration. Filled circles are for the measured friction coefficient; empty circles are for the fraction of load supported by the interstitial fluid.

In Figure 2-5 we report the measured friction coefficient, together with the estimated portion of load supported by the interstitial fluid, obtained in the AC testing configuration. The effective friction coefficient remains low during the whole experiment. The value reached at steady-states, ~0.064±0.017, is similar to that observed under the CC testing configuration (Figure 2-4). The main difference between the result shown in Figure 2-5 and those shown in Figures 2-3 and 2-4 consists in the shape of the μ_{eff} vs. time curve. The measured friction coefficient starts from a relatively high value at the beginning of the experiment (~ 0.070±0.019) and decreases with time to reach a plateau of ~0.064±0.017. Correspondingly, the estimated fraction of load supported by the interstitial fluid increases from ~ 82.7% to 85.0%.

In Table 2-1 we summarize the results presented in Figure 2-3, 2-4, and 2-5 by reporting the friction coefficient measured at the beginning of each experiment, $\mu_{initial}$, as well as the one observed at steady-states, μ_{eq}, for the three testing configurations considered. We also report the estimated fraction of load supported by the interstitial fluid pressurization at the beginning of the experiment, $(W^P / W)_{initial}$, and at steady-states, $(W^P / W)_{eq}$. The number of trials required to reach steady state varies in the 3 testing configurations, reflecting changes in lubrication mechanisms. More details are discussed in section 2.4.4.

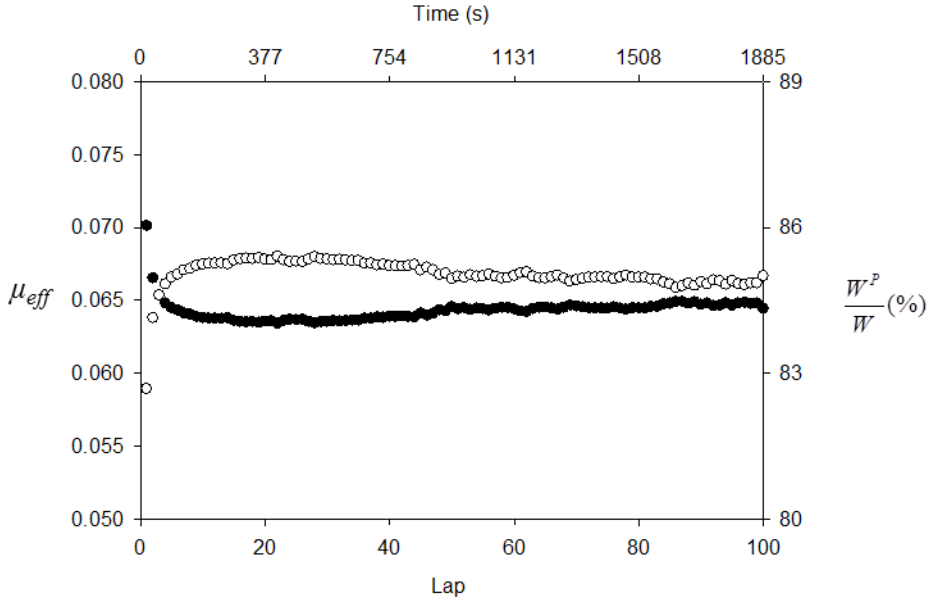

Figure 2-5 Time-dependent friction coefficient, μ_{eff}, and portion of load supported by interstitial fluid, W^P/W, measured in the alumina-on-pin vs. cartilage-on-disc testing configuration. Filled circles are for the measured friction coefficient; empty circles are for the fraction of load supported by the interstitial fluid.

Table 2-1 Initial and steady-states values for the measured friction coefficient ($\mu_{initial}$ and μ_{eq}, respectively) and for the estimated fraction of load supported by the interstitial fluid in the three testing configurations considered. * p<0.01 for CA vs. CC or AC; ** p<0.001 for CA vs. CC or AC; † p<0.001 for initial vs. steady states.

	CA	CC	AC
$\mu_{initial}$	0.099± 0.014†	0.062± 0.021*	0.070± 0.019*
μ_{eq}	0.271± 0.015†	0.071± 0.017**	0.064± 0.017**
$(W^P / W)_{initial}$	71.0%†	85.7%*	82.7%*
$(W^P / W)_{eq}$	1.0%†	82.5%**	85.0%**

2.4.3 Lubricant and Sliding-Speed Effects

To understand the ability of different polymers dissolved within PBS to reduce the measured friction coefficient, we measured the friction coefficient of cartilage lubricated with 4 solutions: (1) PBS, which acts as control; (2) 100mg/ml 10,000 MW PEO in PBS; (3) 100mg/ml 100,000 MW PEO in PBS; and (4) 100mg/ml CS in PBS. For these experiments we only considered the AC testing configuration, in which the alumina-on-pin slides on the cartilage-on-disc.

For brevity, we do not report each individual time-dependent μ_{eff} obtained with the 4 solutions at sliding speed of 1mm/s and normal load of 2N. All the curves follow the features described in Figure 2-5. μ_{eff} however, strongly depends on the lubricants. The friction coefficients of cartilage lubricated with 100mg/ml 100,000 MW PEO and 100mg/ml CS in PBS are ~40% less than those measured in PBS both at the beginning of the experiment and at steady-states. Comparing the results obtained with PEO of different molecular weights, it is found that the higher molecular weight PEO decreases the friction coefficient more significantly than the low-molecular-weight one does. This

difference is due to the solution viscosity, which is 37.2cp for the 100,000 MW PEO, but only 3.5cp for the 10,000 MW PEO. Although PEO is very different than HA, it is interesting to point out that the importance of solution viscosity found in our experiments is consistent with the results reported by Mori et al. Those researchers found that very viscous HA lubricants can decrease the friction coefficient of cartilage.[81]

Because several literature reports revealed that friction coefficient for cartilage depends on sliding speed,[4, 68, 100] we generated a mesh plot to investigate the friction coefficient, μ_{eff}, of cartilage in the 4 solutions just described over a range of sliding speeds (0.2, 0.5, 1 and 5 mm/s). For these experiments we only considered the AC testing configuration in which an alumina sphere slides on the cartilage sample.

The friction coefficient of cartilage in PBS over a range of sliding speeds and lap number is reported in Figure 2-6 A. At any sliding speed, μ_{eff} changes as the lap number (travelled distance) increases, following the trend discussed in Figure 2-5, i.e. μ_{eff} starts from a high value and decreases to a plateau within a few laps. The friction coefficient decreases as the sliding speed increases. The decrease of the measured μ_{eff} is more dramatic when the sliding speed increases from 0.2mm/s to 1mm/s, than in the high-speed range when the sliding speed reaches 5mm/s. μ_{eff} decreases from the maximum of 0.095±0.020, obtained at the beginning of the experiment performed at the slowest sliding speed, 0.2mm/s, to the minimum of 0.044±0.016 at the end of the experiment conducted at the highest sliding speed, 5mm/s.

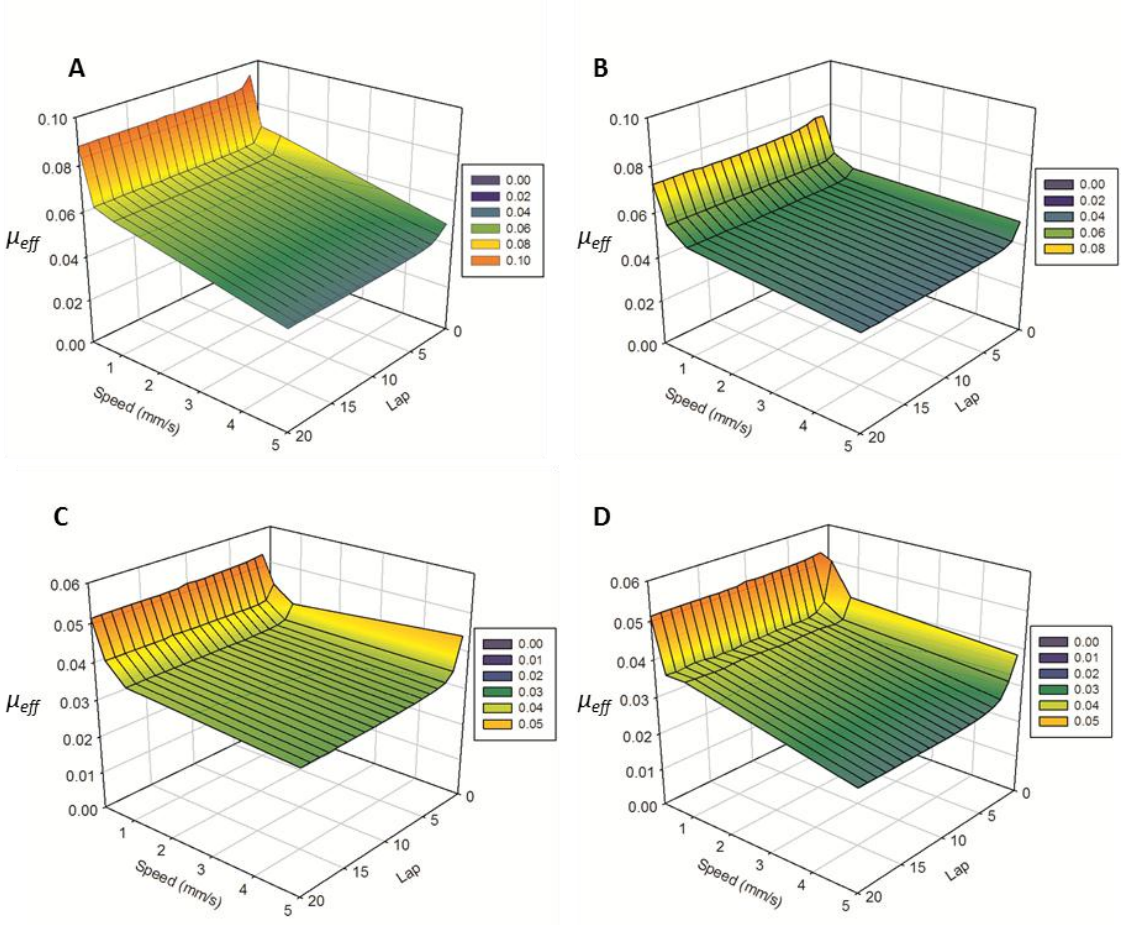

Figure 2-6 Friction coefficient, μ_{eff}, measured in the AC testing configuration over a range of sliding speeds and laps. Panel A is for cartilage lubricated with PBS; B is for cartilage lubricated with 100mg/ml 10,000 MW PEO in PBS; C is for cartilage lubricated with 100mg/ml 100,000 MW PEO in PBS; D is for cartilage lubricated with 100mg/ml CS in PBS.

The friction coefficient, μ_{eff}, of cartilage lubricated with 100mg/ml 10,000 MW PEO in PBS over a range of sliding speeds and lap numbers is reported in Figure 2-6 B. The shape of the plot is similar to that observed in PBS (Figure 2-6 A). The friction coefficient of cartilage in 10,000 MW PEO solution is not significantly lower than that measured in PBS. μ_{eff} decreases from 0.076±0.028 at the beginning of the experiment

performed at the slowest sliding speed, 0.2mm/s, to the minimum of 0.043±0.020 at the end of the experiment conducted at the highest sliding speed, 5mm/s.

The friction coefficient of cartilage lubricated with 100mg/ml 100,000 MW PEO in PBS over a range of sliding speeds and lap numbers is reported in Figure 2-6 C. The plot follows the same trend observed from both PBS and 10,000 MW PEO solutions, although μ_{eff} is significantly lower than those reported above. μ_{eff} decreases from the maximum of 0.053±0.012 obtained at the beginning of the experiment performed at the slowest sliding speed, 0.2mm/s, to the minimum of 0.033±0.010 at the end of the experiment conducted at 5mm/s.

The friction coefficient of cartilage lubricated with 100mg/ml CS in PBS is reported in Figure 2-6 D. The plot follows the trend discussed above. As the sliding speed increases above 2mm/s the measured friction coefficient decreases only slightly. μ_{eff} decreases from the maximum of 0.064±0.018 at the beginning of the experiment performed at the slowest sliding speed, 0.2mm/s, to the minimum of 0.028±0.003 at the end of the experiment conducted at the highest sliding speed, 5mm/s.

2.4.4. Discussions

The first objective of our study is to assess testing-configuration effects on the measured friction coefficient for cartilage. A summary of our experimental results is reported in Table 2-1. The results from the CA configuration are consistent with previous results from McCutchen,[15] Ateshian et al.,[31] and Krishnan et al.[30] These results confirm that the interstitial fluid pressurization is a primary mechanism in the regulation of the friction response of articular cartilage at short times after a load is

applied. As long as the interstitial fluid pressure remains high, the measured friction coefficient is low. When the pressure sustained by the interstitial fluid reduces to zero, the friction coefficient reaches its steady-states value.

We point out the cartilage in our CA experiments is supported on a sphere, not on a flat pin. Although it is possible that as our experiment progresses the contact area changes due to deformation of the supported cartilage, geometrical considerations suggest that the contact area between cartilage on pin and disc is almost flat. Experiments conducted for a cartilage plug supported by a flat pin (see Figure 2-3) confirm that our interpretation does not depend on the geometry of the pin.

More importantly, when the friction experiment is performed under the CC and AC testing configurations, the measured friction coefficient remains low during the entire experiment. The friction coefficient at steady-states (μ_{eq}) in these two configurations is ~ 25% that measured in the CA configuration. One reason for this low friction coefficient is the testing configuration itself. The CC and AC configurations allow cyclical loading on the cartilage. This type of loading, analogous to the migrating contact area discussed by Caligaris et al.,[39] reasonably mimics the physiological conditions in diarthrodial joints, allowing the PBS solution to diffuse back into the cartilage before the load is applied again on the same contact area. For completeness, it should be pointed out that McCutchen had also observed that allowing the cartilage to 'resoak' for a few seconds in between friction experiments yields lower friction coefficients.[12] Our CC and AC testing configurations allow the various cartilage regions compressed by the load to resoak before the load returns. Based on Eq. (2-1), the estimated fluid load supports remain above 80% during the experiment in both CC and

AC testing configurations. This result is in contrast to what observed for the CA testing configuration, in which case the friction coefficient rises significantly with time. This happens because in the CA configurations the constantly applied load on the cartilage forces the interstitial fluid to escape out of the cartilage matrix. As the loading time increases the interstitial fluid support decreases due to the lack of fluid phase.

The measured friction coefficient μ_{eff} increases with time for both the CA and CC testing configurations, while it slightly decreases over time in the AC testing configuration. During the time in between when the load is applied and when the experiment starts (5 seconds), a certain amount of fluid escapes from the cartilage glued on the disc. Thus the high onset friction coefficient in the AC testing configuration is likely due to the depletion of fluid phase in the contact area of cartilage on the disc. This possibility is consistent with results reported by Foster and Fisher.[77] As the sliding distance increases, the fluid phase diffuses back to the pores present in the cartilage sample glued on the disc during the migrating contact area displacement, yielding lower steady-states friction coefficient.

The experimental procedure discussed above could be improved to extend results and methods to those attainable under physiological conditions. First, to limit the inevitable necrosis, the freshest cartilage samples available should be used. And second, the experiments could be conducted under a controlled temperature environment mimicking body temperature. It is possible that trimming the osteochondral plugs does not conserve structural integrity, leading to changes of cartilage physical properties. However, when large cartilage samples are trimmed and then glued on the disc of pin-on-disc instruments, the surface area subject to trimming tends to be far from that tested

during the friction experiment, as shown in Figure 2-2. Experiments conducted under the AC testing configuration should not be affected by this limitation.

The applicability of the interstitial fluid pressurization model to interpret the results presented herein implies that lubrication in joints can be improved by increasing the load fraction supported by the interstitial fluid pressurization. More interestingly, our results indicate a different lubrication mechanism of cartilage under the AC testing-configuration from that of CA and CC testing configurations. The further study of the lubrication mechanism of cartilage under AC testing configuration could lead to better understanding cartilage lubrication.

We investigated how the presence of lubricants within the PBS solution, as well as changes in sliding speed, affects the measured friction coefficient. The comparison of initial and steady-states friction coefficients from different testing speeds and lubricants in PBS are reported in Figure 2-7 A and Figure 2-7 B, respectively. Because the AC configuration was used in all cases, the interstitial fluid supports part of the load in all cases, and the friction coefficients remain low. The initial friction coefficient is larger than the steady-states friction coefficient for all experiments.

Both the initial and steady-states friction coefficients decrease as the sliding speed increases. This finding agrees with other reports, although the typical testing configuration adopted in those other reports was similar to our CA. This suggests that the effect of the sliding speed on the measured friction coefficient might be independent on the testing configuration.[4, 68, 100]

Comparing the effects of lubricants, we find that both 100,000 MW PEO and CS, when dissolved within PBS, are very efficient lubricants for articular cartilage, since

they reduce both initial and steady-states friction coefficients by ~40% (the effect appears stronger at slower sliding speeds). The ability of 10,000 MW PEO to reduce the friction coefficient is less pronounced. Literature data agree in that CS lowers the friction coefficient measured for cartilage.[73, 76, 83] However, it should be pointed out that these literature reports refer to experiments conducted under conditions, comparable to the CA testing configuration, in which boundary lubrication is expected. Our results for PEO disagree in part with those reported by Basalo et al.,[76] who observed that PEO solutions reduce the friction coefficient for cartilage independently on their viscosity. The difference between ours and Basalo et al.'s findings could be due either to the difference of testing configuration implemented, or to the molecular weight of PEO used. Basalo et al. conducted their experiments under a CA configuration, while our data are obtained under the AC configuration. As we discussed above, these two testing configurations could promote different lubrication mechanisms. More important, however, is that Basalo et al. changed the viscosity of the PBS solution by dissolving different amounts of 20,000 MW PEO in PBS. Consequently, the viscosities in Basalo et al.'s work ranged from 16.7cp (133mg PEO per ml of solution) to 24.4cp (170mg/ml). By changing the PEO molecular weight, we increased the PBS solutions viscosity from 3.5cp (10,000 MW PEO) to 37.2cp (100,000 MW PEO). Although it is possible that the PEO molecular weight affects the lubrication mechanisms, it is likely that Basalo et al. did not observe significant changes in the measured friction coefficient because the viscosity of their solutions did not change significantly.

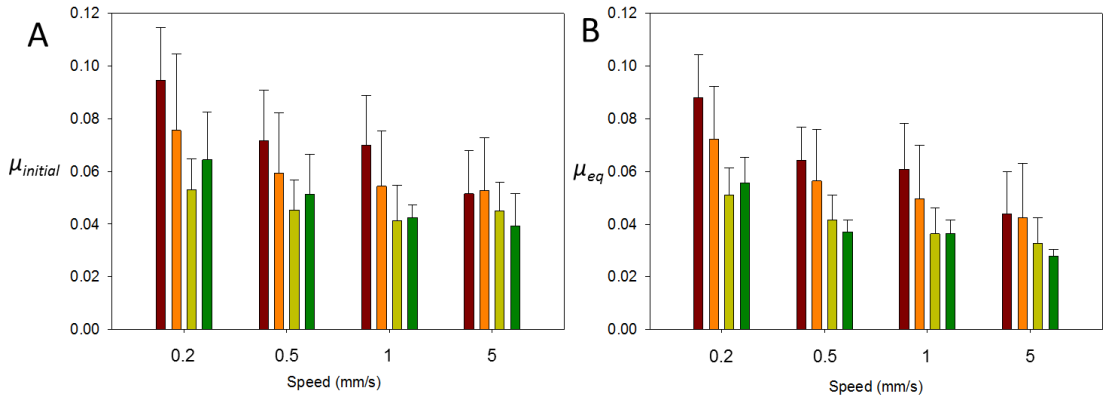

Figure 2-7 Comparison of the friction coefficient measured in the AC testing configuration when cartilage was lubricated with 4 different PBS solutions. Maroon represents PBS; orange represents 100mg/ml 10,000 MW PEO in PBS; yellow represents 100mg/ml 100,000 MW PEO in PBS; green represents 100mg/ml CS in PBS. A is the initial friction coefficient, $\mu_{initial}$; B is the steady-states friction coefficient, μ_{eq}. $p<0.05$ for 0.2mm/s vs. other speed; $p<0.05$ for PBS vs. other lubricants.

To further analyze our results, in Figure 2-8 we plot the steady-states friction coefficient, μ_{eq} in Figure 2-7 B, as a function of the Hersey number, $\eta\upsilon/N$. In this analysis η is the zero-shear-rate viscosity of the corresponding lubricant PBS solution; υ is the sliding velocity; N is the static normal load. The fact that all experimental data collapse into a single curve demonstrates the importance of solution viscosity, normal load and sliding speed in determining cartilage lubrication. The curve in Figure 2-8 can be divided in two parts. In the first part, μ_{eq} decreases as the Hersey number increases, indicating a 'mixed lubrication region' where boundary and fluid-film lubrication mechanisms act together. At these conditions lubrication depends on majorly surface chemistry (boundary lubrication) and partial fluid hydrodynamics. In the second part, μ_{eq} does not change much as the Hersey number increases, indicating that, although

both hydrodynamics and boundary lubrication mechanisms act simultaneously, hydrodynamics effects become more important in comparison to that in the first part of the Hersey plot. For clarity, we point out that the hydrodynamic lubrication may be exaggerated by the continuous circular motion in our experiment set up.

The plot of Figure 2-8 is consistent with the classical Stribeck curve, except that even at very low speeds (0.2mm/s) and solution viscosities (0.88cp for PBS), i.e., at very low Hersey numbers, our curve does not show a 'boundary-mode region' in which μ is invariant as the Hersey number changes. This observation suggests that when the cartilage is completely hydrated under the AC testing configuration considered herein, boundary lubrication never dominate the lubrication mechanism by itself. Gleghorn et al. reported a boundary region in their findings. This disagreement is due to the different testing configurations employed and the different lubrication mechanisms that prevail under the various testing configurations. The data of Gleghorn et al. were collected at steady-states using a CA configuration. It is likely that Gleghorn et al.'s data show a boundary region in the Stribeck plot because the CA configuration leads to direct contact between cartilage and disc when the interstitial fluid is dissipated at steady-states. In our work, at steady-states the cartilage glued on the disc always contains enough fluid at the migrating contact area and no boundary region is observed. Our results suggest that experiments conducted in the AC testing configuration (this work) provide a complementary understanding of cartilage lubrication when combined with experiments conducted in configurations consistent with the CA testing configuration (e.g., the contribution by Gleghorn et al.) It is however possible that changing the Hersey number by increasing the normal load (not attempted herein) could trigger to a

larger extent the boundary lubrication mechanism, which is not evident from our results. Another difference between the curve in Figure 2-8 and the classical Stribeck curve is that the friction coefficient in our experiments does not increase slowly as Hersey number reaches very high values, as expected should hydrodynamic lubrication be the only acting mechanism. This suggests that, within the experimental conditions tested herein, the fluid hydrodynamics under the AC configuration never dominate the lubrication mechanism of articular cartilage.

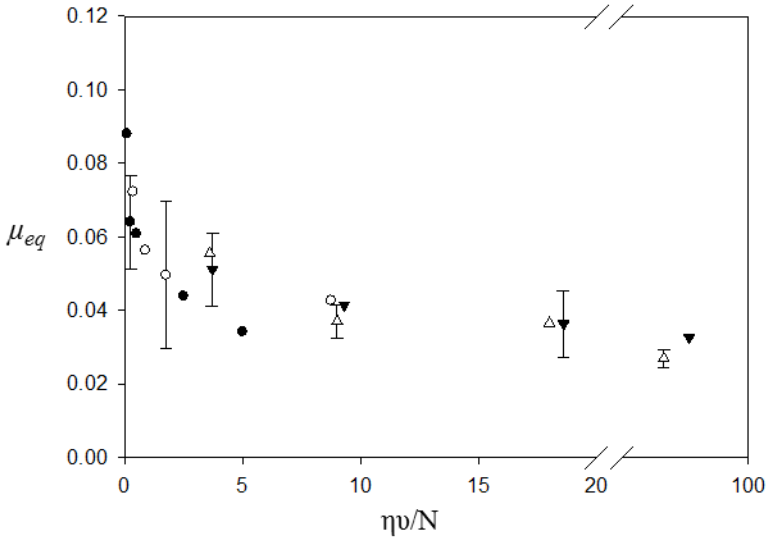

Figure 2-8 Stribeck curve obtained by plotting the steady-states friction coefficient, μ_{eq}, measured in the AC testing configuration, as a function of the Hersey number (ηυ/N). Filled circles are for experiments conducted in PBS; empty circles are data obtained when 100mg/ml 10,000 MW PEO is dissolved in PBS; filled inverted triangles are for 100mg/ml 100,000 MW PEO in PBS; empty triangles are for 100mg/ml CS in PBS. Only representative error bars are shown for clarity.

3. Friction Coefficients for Mechanically-Damaged Bovine Articular Cartilage

The material presented below was published in 2012 in volume 109, issue 7, of the journal 'Biotechnology and Bioengineering'.

3.1 Abstract

We used a pin-on-disc tribometer to measure the friction coefficient of both pristine and mechanically damaged cartilage samples in the presence of different lubricant solutions. The experimental set up maximizes the lubrication mechanism due to interstitial fluid pressurization. In phosphate buffer solution (PBS), the measured friction coefficient increases with the level of damage. The main result is that when poly(ethylene oxide) (PEO) or hyaluronic acid (HA) are dissolved in PBS, or when synovial fluid (SF) is used as lubricant, the friction coefficients measured for damaged cartilage samples are only slightly larger than those obtained for pristine cartilage samples, indicating that the surface damage is in part alleviated by the presence of the various lubricants. Among the lubricants considered, 100mg/ml of 100,000 Da MW PEO in PBS appears to be as effective as SF. We attempted to discriminate the lubrication mechanism enhanced by the various compounds. The lubricants viscosity was measured at shear rates comparable to those employed in the friction experiments, and a quartz crystal microbalance with dissipation monitoring was used to study the adsorption of PEO, HA, and SF components on collagen type II adlayers pre-formed on

hydroxyapatite. Under the shear rates considered the viscosity of synovial fluid is slightly larger than that of PBS, but lower than that of lubricant formulations containing HA or PEO. Neither PEO nor HA showed strong adsorption on collagen adlayers, while evidence of adsorption was found for synovial fluid. Combined, these results suggest that synovial fluid is likely to enhance boundary lubrication. It is possible that all three formulations enhance lubrication via the interstitial fluid pressurization mechanism, maximized by the experimental set up adopted in our friction tests.

3.2 Introduction

Articular cartilage is a weight-bearing and wear-resistant natural tissue with experimentally reported extremely low friction coefficients.[13] It is composed of 68-85% water, 10-20% extracellular matrix (mostly collagen type II fiber), 5-10% proteoglycans, salts, and chondrocytes. Structural and composition properties change within a cartilage sample, and superficial, middle, and deep zones can be identified[1]. A number of lubrication mechanisms have been proposed to explain cartilage lubrication. These include hydrodynamic,[18] elasto-hydrodynamic,[19] squeeze-film,[20-22] weeping,[23, 101] boosted,[24] boundary,[14-17] and interstitial fluid pressurization.[2, 25, 26]

We recently measured the friction coefficient for mature bovine knee cartilage using a commercial pin-on-disc tribometer.[102] Depending on the experimental set up, the instrument can probe migrating as well as non-migrating contact area mechanisms. By comparing the friction coefficient as a function of time in the two experimental set

ups, we found strong evidence suggesting the importance of the interstitial fluid pressurization for lubricating cartilage. The 'migrating contact area' testing configuration allows the area on the cartilage on which pressure is applied (contact area) to change during sliding, while in the 'non-migrating' mode the cartilage area that is pressurized remains so during the entire experiment. Because of this difference, under migrating contact area conditions the lubrication due to interstitial fluid pressurization is maximized. Note that Morrell et al. demonstrated, using in vivo experiments, the importance of interstitial fluid pressurization in joint tribology.[41] Because maintaining high interstitial fluid pressurization is required for obtaining measurements with physiological relevance, we only consider the experimental set up that allows the contact area to migrate in the present study.

Caligaris et al. designed a novel experimental set-up, which implements a migrating contact area mechanism, to study the friction of cartilage immersed in synovial fluid (SF). They reported continuously low friction coefficients.[3, 39] When the experimental set up employed in our pin-on-disc apparatus probes the migrating contact area mechanism, the results obtained are semi-quantitatively similar to those obtained by Caligaris et al.

Most literature reports on cartilage lubrication are conducted on samples with pristine surface properties. In this work we quantify the friction coefficient, measured under the migrating contact area mode, for cartilage samples whose surface has been mechanically damaged. The results are compared to those obtained for pristine samples under the same experimental conditions. Because of the slow regeneration typical of

cartilage, damaged cartilage likely leads to osteoarthritis (OA). Our experiments will test whether mechanically damaged surface yields higher friction coefficients.

Under the migrating contact area configuration the pressurization of the interstitial fluid is maintained at elevated levels during the entire experiment. We use this experimental set up to test the importance of other lubrication mechanisms while the interstitial fluid pressurization is maintained elevated, with focus on boundary lubrication and the viscosity of the lubricants. Identifying the lubrication mechanisms most effective at lowering friction coefficients for mechanically damaged cartilage samples could help design formulations to mitigate mild OA symptoms. Boundary lubrication occurs when the fluid film separating two surfaces is thinner than the surface asperities. About 10% of the total area contributes to cartilage-cartilage contact under physiological conditions.[41, 103] It is expected that boundary lubrication becomes more important when high loads and slow sliding velocities are applied. It has been reported that boundary lubrication is important to prevent precocious joint degeneration when joint movement is not sufficient to establish hydrodynamic lubrication.[86, 104] The lubricant viscosity could affect hydrodynamic and elasto-hydrodynamic lubrication. However, hydrodynamic lubrication is precluded in the natural joint by the absence of unidirectional motion, and elasto-hydrodynamic lubrication appears not likely to occur based on pressure data.[41, 105] Although it is possible that hydrodynamic lubrication is present in our experiments because of the continuous circular motion, the natural roughness present on cartilage, thicker than the expected fluid film formed on the material, rules out the possibility of hydrodynamic lubrication.

It is however possible that the viscosity of the lubricant formulation affects the permeability of cartilage to interstitial fluid.

To probe different lubrication mechanisms we change the composition of the lubricant solution, following in spirit Schmidt et al.[5, 6] These Authors probed the boundary lubrication mechanism for cartilage by increasing the concentration in PBS of various compounds typically present in synovial fluid (SF). SF is a complex aqueous mixture that contains, among other components, hyaluronic acid (HA), surface-active phospholipids (SAPL), superficial zone protein (SZP, also referred to as lubricin). HA,[67, 81, 82] SAPL,[33, 34, 82] and SZP[84-86] have all been found to reduce the friction coefficient for cartilage. Several SF components have been proposed as possible boundary lubricants, including SZP, HA and SAPL[84, 106, 107] although Chan et al. argued that only SZP plays a major role, while the effects of HA and SAPL are marginal.[86] Schmidt et al. reported that HA and SZP have synergistic lubrication effects when boundary lubrication is probed.[5] It should be pointed out, for completeness, that good lubrication is necessary, but not sufficient to maintain healthy cartilage in joints[108]. For example, Rhee et al. showed that in the absence of lubricin normal mice joints degenerate as the mice age,[109] and diseases might compromise the tissue integrity independently on weight-bearing activities.

Because most of the experimental data just summarized have been obtained under non-migrating contact area conditions, it is of interest to understand the mechanism by which each SF component lubricates cartilage when the pressurization of the interstitial fluid is maintained elevated (migrating contact area conditions). We consider here HA, dissolved in PBS, and we compare the friction coefficient measured for this solution to

that measured in SF. HA is one of the SF compounds that is usually associated, among other biological function, with lubricating capabilities. It is also used in formulations to manage mild OA. We also consider a PBS solution containing polyethylene oxide (PEO) to assess the lubricating properties of a synthetic polymer. Both HA and PEO used in this study are hydrophilic linear molecules with comparable MW (~300,000 and 100,000 Da, respectively), although HA is a polyelectrolyte and PEO is only partially charged. Comparing the lubricating properties of these two compounds could allow us to discover effective formulations for OA management.

In an attempt to assess whether components from the lubricant formulations adsorb on cartilage, and therefore are likely to provide boundary lubrication, we employed a quartz crystal microbalance with dissipation (QCM-D). We prepared an adlayer of pre-adsorbed collagen type II on a hydroxyapatite sensor as a crude model for cartilage. QCM-D determines, with high sensitivity, the adsorption of various compounds onto a surface[110-112] QCM-D provides real-time measurements of frequency, and dissipation. Changes in vibration frequency are due mainly to the adsorption of compounds, while dissipation reflects changes in viscoelastic properties.[110-113]

3.3 Experimental Procedures

3.3.1 Experimental Protocol: Friction Coefficient Experiments

We conducted the friction coefficient experiment under the alumina-on-pin vs. cartilage-on-disc (AC) testing configuration using a pin-on-disc tribometer (CSM,

model S/N 18-312). The experimental set up is described in section 2. All lubrication experiments were conducted at ambient conditions. In section 2, we concluded that the AC configuration probes lubrication within migrating contact area conditions, which maintains high interstitial fluid pressurization, consistently with what has been observed to happen during in-vivo experiments,[41] although physiological conditions cannot be reproduced because of practical limitations (e.g., the cartilage sample is used post-mortem, alumina-cartilage contacts are sampled rather than cartilage-cartilage ones, a cartilage plug is used without the deep tissue). The hard material used for the pin (alumina sphere) is intended to mimic a prosthetic device. When cartilage specimens are placed both on the pin and on the disc, lower friction coefficients than those reported in this work are typically expected.

The friction coefficient (μ=friction force/normal load) was measured under a continuous static normal load of 2 N (corresponding to an estimated nominal contact pressure of 0.63 MPa on a flat contact area of 2 mm in diameter, within the physiological range during human walking activities[41]). The constant sliding velocity of 1 mm/s was used for all experiments, following published literature for comparison.[3, 39, 74, 76, 114] The friction coefficient was monitored continuously by measuring the deflection of the elastic arm that holds the pin. Following our established protocol,[102] all friction tests were terminated after 20 laps, corresponding to a travelled distance of 377 mm. The average friction coefficient measured during the 1st lap is reported as the initial friction coefficient, μ_{ini}. The plateau friction coefficient obtained by the 20th lap is reported as the steady-state friction coefficient, μ_{eq}. Friction coefficients reported herein are average values from at least 8 independent

measurements conducted using 4 different cartilage samples (twice on each cartilage sample). All cartilage samples used in this work were obtained from three knees, and extracted from lateral and medial femoral condyles. The 4 samples used for determining one friction coefficient were not necessarily from the same knee. All experiments were conducted at ambient conditions.

3.3.2 Cartilage Specimen Preparation

Bovine knees of 15-30 months were purchased from Animal Technologies Inc. They were delivered within 3 days after slaughter. The knees were not frozen, but stored at ~4°C until dissection. Ball et al. reported that human osteochondral allografts show very limited decay within 7 days when stored at ~4°C.[115] Full depth osteochondral plugs (Ø=10 mm) were harvested from lateral and medial femoral condyles using a scalpel and 10mm biopsy punches. These osteochondral plugs were about 3 mm thick with deep zone tissues and then trimmed to maintain a constant thickness (1.3±0.2 mm) by removing the deep zone tissues parallel to the intact surface with a sledge microtome (Leica SM2000 R). After preparation, the specimens were frozen and stored at -20°C in PBS (pH 7.4) for no longer than 2 months.[3, 39, 73, 74, 77, 78, 107, 116] It has been reported that storing articular cartilage at -20°C does not alter its mechanical properties.[117] 18.2 MΩ cm resistivity water was used to prepare PBS. The frozen cartilage plugs were thawed and soaked in PBS for 12 hours at 4°C before use. The plugs, of thickness 1.1-1.5 mm, were glued using cyanoacrylate glue on the alumina surface of the plate for testing in the AC configurations.

To prepare the damaged cartilage samples a sharp pin was used to inflict a circular incision, limited to the superficial zone, on some of the cartilage samples. The procedure was performed on the day the friction experiments were conducted. One cartilage sample was mechanically damaged yielding three degrees of impairment. On type I damaged cartilage samples only one circular incision was produced; on type II and on type III cartilage samples two and three circular incisions were inflicted, respectively (see Figure 3-1). The inflicted cuts did not remove the superficial cartilage tissue in the regions neighboring the cuts. It is possible that collagen fibers were rearranged near the cuts, although such perturbation was not quantified. We recognize that the damages inflicted with our procedure do not resemble those due to typical joint injuries. However, by inflicting a circular incision of constant diameter and centered on the sample center it is possible to continuously monitor the friction coefficient using our pin-on-disc tribometer, and therefore obtain reliable and reproducible results. This would not be possible with other types of surface damages (e.g., a pinhole). Despite limitations, our experimental set-up allows us to study the effects of superficial zone integrity on cartilage lubrication. It should be stressed that no data exist in the literature for the friction coefficient of damaged cartilage samples measured under migrating contact area conditions, which are probed by our experiments. Compared to alternative approaches, e.g. employing OA cartilage samples,[3] our superficial cuts allow us to test the effect of damages restricted to the superficial cartilage zone on the measured friction coefficient. Only type II damaged cartilages were used to measure friction coefficients using lubricant solutions other than PBS.

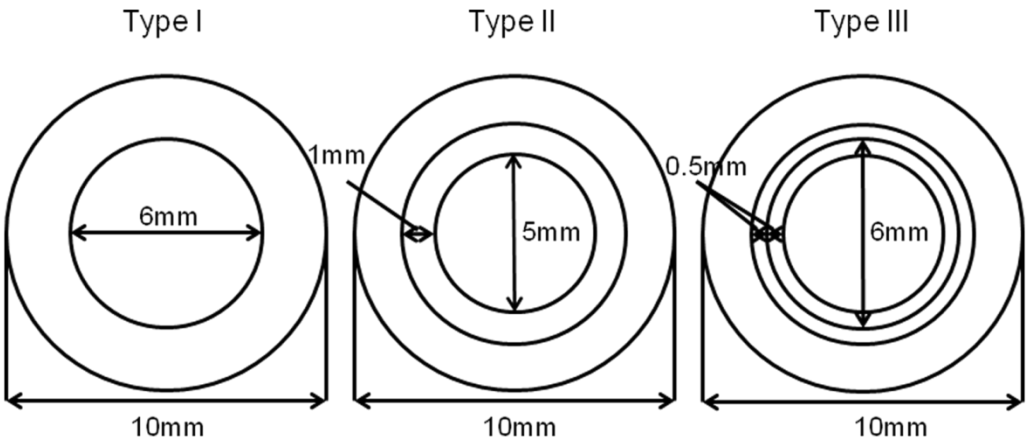

Figure 3-1 Schematic diagram of three damaged cartilage surfaces. Because the width of the migrating contact area is ~2 mm, during the friction experiments the pin-surface contact always includes the circular incisions.

3.3.3 Cartilage Surface Characterization

A Nikon SMZ-10 camera was used to image the 10-mm diameter cartilage samples on which the incisions had been performed. Wet samples were dabbed dry with a lint-free towel, then depth measurements of the incisions were performed using a Nikon Optiphot 66 microscope with a brightfield/darkfield (BD) plan 20× differential interference contrast (DIC) objective lens (depth of field 3.5 μm). First, we focused on the bottom of an incision by adjusting the stage z-position. Then, we focused on the surface of the cartilage adjacent to the incision. The difference in the stage z-position gives the incision depth. The total estimated error is ~3 microns.

3.3.4 Lubricants Preparation

Four aqueous solution groups were prepared: (1) The control solution was PBS. (2) Bovine synovial fluid (SF) purchased from Animal Technologies Inc. was used directly as lubricant. (3,4) The other two solutions were obtained by dissolving PEO or HA in PBS. These solutions contained 100mg/ml 100,000 Da MW PEO (Sigma-Aldrich, St. Louis, MO, USA), and 10 mg/ml HA sodium substitute (Sigma-Aldrich, St. Louis, MO, USA, obtained from bovine vitreous humor). The HA used for this work was of MW ~300,000 Da, chosen to be comparable to the PEO MW. PEO was chosen because it is often used in biomedical applications, and because when used as lubricant for pristine cartilage, the 100,000 Da MW PEO solution yields much lower friction coefficients than PBS.[102] PEO and HA were used as received.

3.3.5 Solution Viscosities

A MERLIN self-contained rotational viscometer (REOLOGICA Instruments, Borden Town, NJ) was used to measure the steady shear-rate viscosity of each solution. The 25 mm bob and cup system with narrow gap was employed to measure viscosities at high shear rates at 25˚C. The viscosity of PBS and that of 100,000Da PEO in PBS were found to be constant over the shear rate range of ten to thousands s^{-1}. In this range the viscosity of PBS was ~1 cp. The viscosity of PBS containing PEO was ~80 cp. The lubricant formulations containing HA and SF show shear thinning, i.e. the viscosity decreases as the shear rate increases. The shear rate during the lubrication experiments is estimated in ~ 1000 s^{-1}, calculated by assuming a distance of 1 μm between alumina pin and cartilage sample, which corresponds to the cartilage surface roughness.[77] The

sliding speed of our lubrication experiments is 1 mm/s. The viscosity of PBS containing HA and that of SF at the shear rate of 1000 s^{-1} are ~75 (comparable to that of PBS containing PEO) and ~8 cp, respectively. It should be pointed out that PBS containing HA shows viscosities larger than ~80 cp at low shear rates, while SF has maximum viscosity of ~65 cp found at the shear rate of 20 s^{-1}. Details are reported in Appendix C Figure 7-26.

3.3.6 Quartz Crystal Microbalance with Dissipation (QCM-D)

All adsorption experiments were conducted at T=25±0.05°C by a QCM-D, model E4, purchased from Q-Sense AB. Because the QCM-D data depend on solution viscosity and density, all lubricant solutions were diluted in PBS and showed viscosity and density similar to those of PBS. Both PEO and HA solutions were diluted to the concentration of 1 mg/ml for the QCM-D experiments. SF was diluted 20 times with PBS, after being clarified by centrifugation at 20,000×g at 4˚C for 30 minutes. Centrifugation was necessary to avoid interference between dust and QCM-D sensors. No centrifugation was performed for the SF used in lubrication experiments. Collagen type II (Sigma C1188) was first dissolved in 0.5 M acetic acid at 1 mg/ml, and then diluted to 50 μg/ml with PBS (pH ~6). All substrates used were 10 nm hydroxyapatite (QSX 327), purchased from Q-Sense AB.

Every measurement started by first obtaining a baseline for the hydroxyapatite crystals in contact with PBS. Then the PBS solution containing collagen was pumped through the QCM-D sensors for 1 hour to form a collagen adlayer. After 6-7 hours, PBS was pumped through the chamber for 30 minutes to wash away all unbounded collagen.

After ~2 hours one of the PBS lubricant solutions was injected for 1 hour to study the adsorption of PEO, HA, and SF on the collagen adlayer. Solutions were pumped through the instrument using an Ismatec peristaltic pump at a constant flow rate of 75 µl/min. QCM-D experiments were repeated at least twice.

3.3.7 Statistical Analysis

Mean and standard deviation were calculated and the statistical significance of the differences in the friction coefficients measured was determined. A one-way analysis of variance (ANOVA) with Tukey's HSD post hoc test was used to compare the steady-state and initial friction coefficients for the various cartilage samples. Differences between the friction coefficients obtained under different lubricant solutions on type II damaged cartilages were analyzed in the same manner. All statistical analyses were carried out using PASW Statistics 18 (SPSS Inc., Chicago, IL); α was set to 0.05 and the statistical significance was accepted for $p<0.05$.

3.4 Results and Discussions

3.4.1 Cartilage Characterization

The surface morphology of type III mechanically damaged cartilages is shown in Figure 3-2. The damaged cartilage shows circumferential incisions, which are irregular, with both straight and jagged portions. The upper and lower insets are DIC images from two different positions. For both insets the left image is focused on the incision bottom, and the right is focused on the surrounding cartilage. The stage z-position difference

from the upper inset gives an incision depth of 40±3 μm, that from the lower inset 68±3 μm. Although the incision depth is not constant within a sample, most of the damaged cartilage samples yield incision depths no deeper than about 100μm (less than 10% of the thickness of the cartilage plug glued to the alumina plate).

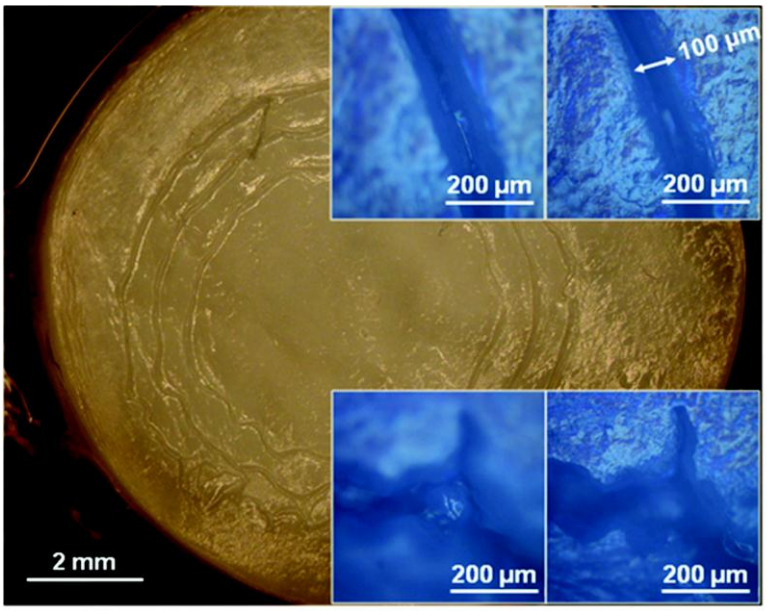

Figure 3-2 Low magnification stereo zoom image of an entire 10-mm diameter wet sample of type III damaged cartilage showing circumferential incisions. The insets show higher magnification images. The left (right) inset has the bottom (surrounding surface) of the incision in focus. The upper and lower insets are for two different positions within one incision.

3.4.2 Friction Coefficients

In Figure 3-3 we report the measured friction coefficient for pristine and mechanically damaged cartilage samples in PBS. For the pristine cartilage μ_{eff} is found to decrease with time from a maximum of 0.065±0.016 to a steady-state value (μ_{eq}) of 0.050±0.006. The plateau is reached within 10 laps after starting the experiment, consistent with our prior results[102]. Although the time-dependent friction coefficients

for type I and type II damaged cartilages show similar profiles as obtained for pristine cartilage, the measured μ increases with the number of incisions. The initial μ for type I and type II cartilages are 0.066±0.010 and 0.074±0.013; and μ_{eq} are 0.055±0.008 and 0.062±0.007, respectively. For type III damaged cartilage, the results show an irregular behavior. The initial μ is larger than those measured for all other samples (0.084±0.014), it then decreases as the lap number increases to ~5, but then it increases irregularly as the lap number increases further. This erratic behavior is probably due to incipient wear, although such possibility has not been quantified, as discussed below.

We investigated how different lubricant formulations affect the measured friction coefficient. The steady-state friction coefficients from pristine cartilage samples lubricated with 4 solutions are reported in Figure 3-4, left. SF, as well as lubricant formulations containing HA and 100,000Da PEO decrease μ_{eq} compared to results obtained in PBS. The friction coefficient decreases from 0.050±0.006 in PBS to 0.040±0.003 in SF, 0.041±0.005 in HA and 0.037±0.003 in PEO.

We only conducted friction coefficients experiments in solutions other than PBS for type II damaged cartilage samples because these samples show the largest μ_{eq} while maintaining a dependency of the measured μ as a function of lap number similar to that observed in pristine cartilage (Figure 3-3). In Figure 3-4, right, we compare μ_{eq} measured for type II damaged cartilage samples in all the lubricant solutions considered. μ_{eq} decreases from 0.062±0.007 in PBS to 0.043±0.003 in SF, 0.047±0.004 in HA and 0.039±0.002 in PEO.

The trends observed when the initial friction coefficients are considered for both intact and damaged cartilages are similar to those just discussed, and are reported in the

bottom panels of Figure 3-4. The main difference is that the initial friction coefficient is always larger than the steady-state one

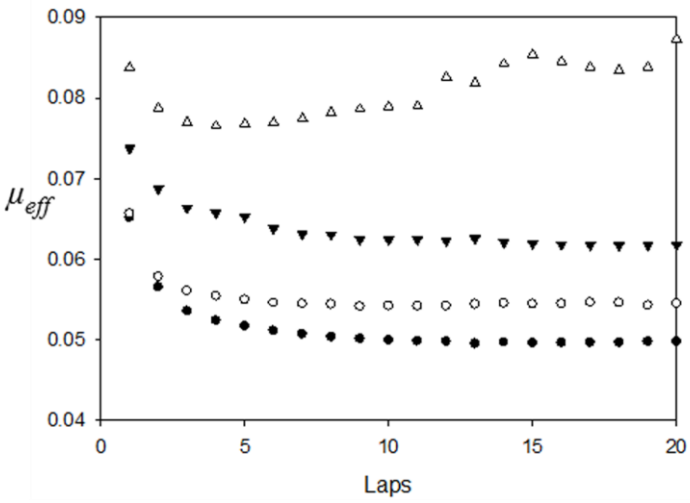

Figure 3-3 Time-dependent friction coefficient, μ_{eff}, obtained in the alumina-on-pin vs. cartilage-on-disc testing configuration. During the friction experiment 20 laps correspond to a sliding distance of 0.377 m and 377 seconds. Filled circles (●) are for the friction coefficient from pristine cartilage samples; empty circles (○) are for type I cartilage; black inverse triangles (▼) are for type II cartilage; empty triangles (Δ) are for type III cartilage. $p<0.05$ for steady-state friction coefficient of pristine vs. damaged (type II, III) cartilage samples. Error bars are not shown for clarity, but they are reported in the text. The experiments were conducted at ambient conditions.

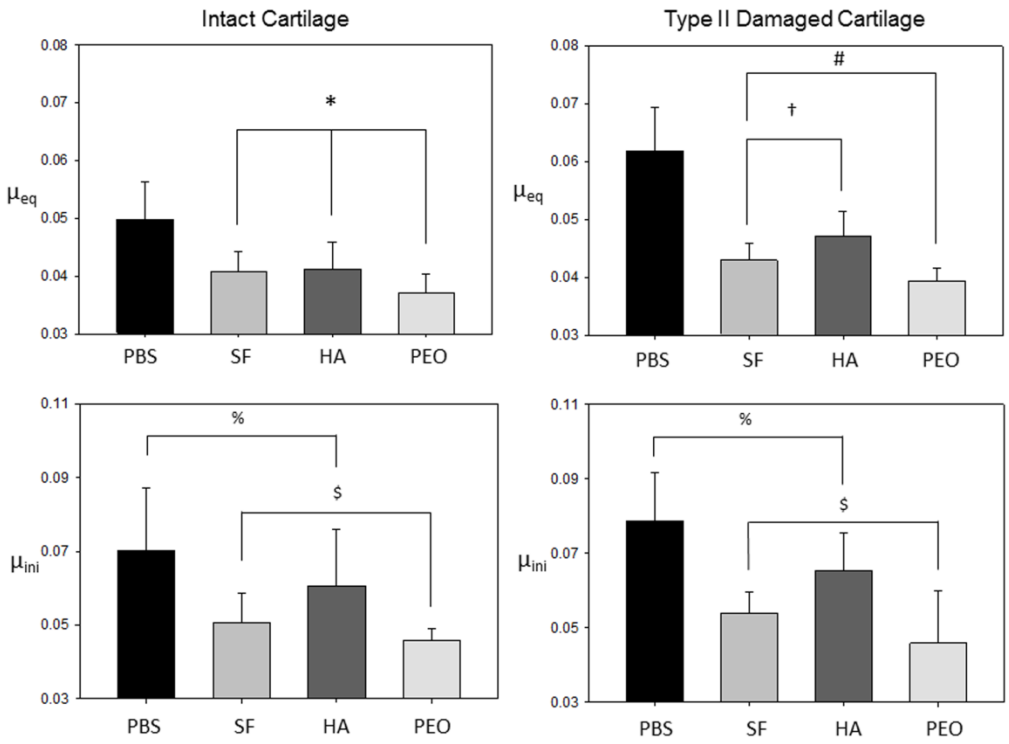

Figure 3-4 Left: comparison among steady-state and initial friction coefficients, μ_{eq} and μ_{ini}, measured for pristine cartilage samples lubricated with 4 different solutions. For μ_{eq}, $p<0.01$ for PBS vs. other lubricants; $p>0.05$ for *, % and $. Right: comparison among μ_{eq} and μ_{ini}, measured for type II damaged cartilage samples. For μ_{eq}, $p<0.01$ for PBS vs. other lubricants and $p<0.05$ for PEO vs. HA; $p>0.05$ for †, #, % and $. The experiments were conducted at ambient conditions.

3.4.3 Quartz Crystal Microbalance with Dissipation Measurements

The QCM-D signals (frequency and dissipation) at the 9th harmonic as a function of time are shown in Figure 3-5 for 2 separate experiments. The experimental results shown on the left panel are obtained by injecting the following sequence of solutions: (I) collagen type II, (II) PBS, and (III) 100,000Da PEO in PBS. The data can be divided in 3 regions. In region I the frequency decreases as a function of time, because collagen

type II adsorbs on the hydroxyapatite surface. After ~7 hours, Δf and ΔD no longer change. At ~8 hours PBS was injected to wash the surface of unbounded collagen (region II). The frequency increases because collagen molecules desorb. For completeness, it should be noted that the solution pH changes from ~6 to 7.4 during the PBS wash. The pH change could be responsible for collagen desorption. The pH will then remain constant for the subsequent steps. The collagen type II adlayer remaining on the hydroxyapatite surface was considered as a crude representation of a cartilage surface, despite a number of clear differences (e.g., the adlayer is thin compared to cartilage, it is only composed by collagen type II molecules, etc.) After washing is complete, the PEO solution is injected. The data (region III) show no clear change in either Δf or ΔD. These data suggest that at the condition considered herein PEO does not adsorb on the collagen adlayer. Results obtained when the HA solution in PBS was used instead of the PEO solution are analogous to those just discussed, and are consistent with no HA adsorption on the collagen adlayer.

The experimental results shown on the right panel of Figure 3-5 are obtained by injecting the following sequence of solutions: (I) collagen type II, (II) PBS, and (III) a PBS solution of SF. As shown in Figure 3-5, right panel, the QCM-D results obtained when SF was injected after the PBS wash are more complicated. In region III the frequency decreases from the values observed after the PBS wash, reaches a minimum, and then increases.

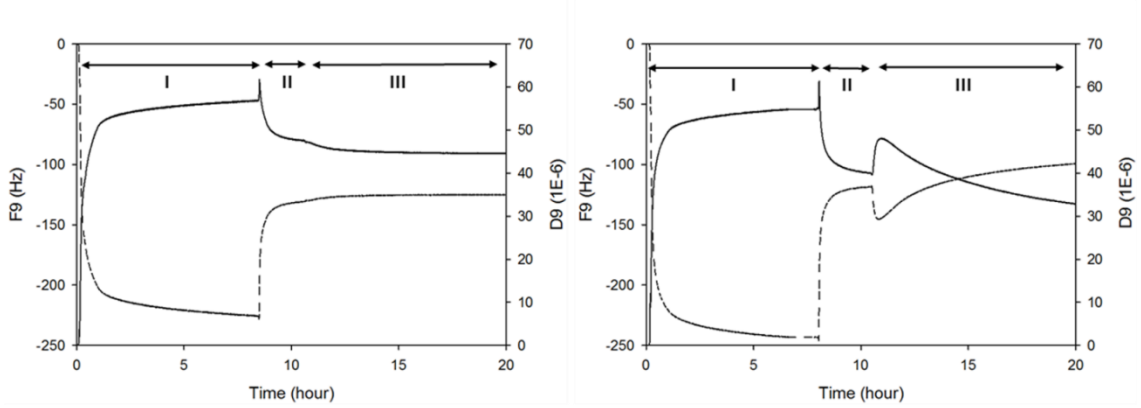

Figure 3-5 Frequency and dissipation shift at the 9th harmonic (n=9) measured by QCM-D as a function of time, while various PBS solutions were injected on a hydroxyapatite crystal. Dash line corresponds to frequency; solid line corresponds to dissipation. The left panel is for the following sequence of injected PBS solutions: collagen type II, PBS wash, and PEO. The right panel is for data obtained when instead of the PEO solution, a PBS solution of SF was injected after the wash step. In all cases T= 25±0.05°C.

3.4.4 Discussions

Time-dependent friction coefficient data collected for pristine cartilage samples in PBS under the AC testing configuration are similar to those discussed at length in our prior work,[102] and are consistent with those reported by Caligaris and Ateshian.[39] These results are consistent with the widely accepted notion that the structure of healthy cartilage, by itself, is responsible for the typical extremely low friction coefficients.[16] It should however be pointed out that in our experiments motion is unidirectional, while physiological articular motion is not. Complex experimental apparatuses able to measure instantaneous friction coefficients would be required to test cartilage

lubrication in multi-directional motion. Such apparatuses could also be used to measure friction coefficient in correspondence of localized cartilage damages, e.g., pin holes.

When the cartilage samples bear mechanically-inflicted incisions, the measured friction coefficients increase with the number of incisions. These results appear to be in conflict with a recent report by Caligaris et al.[3] These Authors measured the friction coefficient for cartilage samples degraded, to different degrees, because of osteoarthritis, OA. Visual inspection, mechanical testing and biochemical essay were used to quantify the level of OA degeneration. The friction coefficients measured in PBS showed no correlation with the level of OA degeneration. Those measured in SF also did not show correlation with the level of OA degeneration, although they were lower than those measured in PBS. Mechanical testing included stress-strain curves, but the integrity of the cartilage surfaces was only observed visually (significant surface degradation was visible). It is possible that the discrepancy between our observations (the friction coefficient measured in PBS increases as cartilage is mechanically damaged) and those of Caligaris et al. (no correlation was found between friction coefficient and OA degeneration) is due to the incisions inflicted in our samples. Note that the incisions are located within the contact area between the alumina sphere and the cartilage. Such incisions are expected to increase the cartilage surface roughness, and could compromise, to some extent, the lubrication due to interstitial fluid pressurization.

It should be pointed out that OA affects not only the cartilage tissue, but the SF composition as well.[118] To quantify how OA affects cartilage lubrication, one should conduct experiments in which synovial fluid extracted from OA joints is employed. The

results presented herein are limited to the quantification of lubrication capabilities of HA and PEO dissolved in PBS as compared to those observed for SF.

When three incisions are inflicted within the contact area between the alumina sphere and cartilage, the large measured friction coefficient shows erratic behavior. It is possible that these many incisions promote cartilage wear during the friction experiments. We did not further characterize wear during our experiments, although we recognize its importance in OA management.[119] Because static friction coefficients could help rationalize wear, we reported in Figure 3-4, bottom panels, data for the friction coefficients measured at the beginning of our experiments (μ_{ini}). The trend is analogous to that observed for μ_{eq} and therefore not discussed further for brevity.

In the presence of SF and lubricant formulations containing PEO or HA the friction coefficient of both intact and damaged cartilage samples decrease significantly compared to results in PBS. The friction coefficients obtained in our experiments in PBS and SF, ~0.5 and ~0.4, are larger than, but comparable to those reported by Caligaris et al. (~0.25 and ~0.2 in PBS and SF, respectively[3]) The difference could be due to different contact stress (Caligaris et al. employed ~0.2 MPa, while in our experiments the contact stress is ~0.63 MPa), to the different level of cartilage surface damage, and to the different experimental set up. No data are reported in the literature for friction coefficients measured under the migrating contact area experimental set up for cartilage (either intact or damaged) in the presence of lubricant formulations containing HA or PEO.

When SF, or PBS solutions containing HA or PEO are used, the steady-state friction coefficients measured for mechanically damaged cartilage are only marginally

larger than those measured for the pristine samples. It appears that the level of surface damage inflicted on the cartilage samples used in our experiments is large enough to yield different friction coefficient when PBS is the lubricant, but not when SF, or PBS augmented by HA or PEO are used. Further, our results suggest that, although the structure of cartilage is for the most part responsible for the lubrication of the pristine material, when the mechanical integrity of the sample is compromised, lubrication mechanisms due to the components present in the interstitial fluid might become essential. Our data suggest that the lubrication ability of HA is slightly less than that of SF, probably because SF contains many effective lubrication components including SZP and SAPL, in addition to HA. This interpretation is consistent with available data, obtained under the non-migrating contact area configuration, according to which HA and SZP have synergistic lubrication effects.[5]

Our results show that the synthetic polymer PEO is an effective lubricant for both pristine and damaged cartilage samples. For pristine cartilage, this finding agrees with previous data from our group[102] and others[76], although data from Basalo et al. were obtained under the non-migrating contact area configuration. No literature data are available to compare the friction coefficients reported here for PEO on damaged cartilage. Understanding the mechanism by which PEO provides such excellent lubrication could aid osteoarthritis management, and also could lead to the design of high performance lubricants for advanced applications. Toward this objective future work should consider the friction coefficient at the cartilage-cartilage interface [68, 120] as well as cartilage wear.[119]

The experimental set up used here is designed to enhance the interstitial fluid pressurization. HA and PEO affect PBS viscosity,[81, 88, 121, 122] which is responsible for load transfer across the interfaces, and might affect the cartilage permeability to interstitial fluid. Under experimental configurations designed to test boundary lubrication, HA was found to provide lubrication both by itself and in synergism with lubricin.[5] In the case of pristine cartilage samples, our prior results show that increasing the viscosity of the lubricating solution can lower the measured friction coefficients.[102] Our friction coefficient results for both pristine and mechanically damaged cartilage samples in the presence of HA and PEO could be explained by the increased viscosity of the PBS solutions due to the dissolution of these compounds. Because increasing the HA and PEO MW increases solution viscosity, it is expected that employing higher-MW samples of both polymers would lower the measured friction coefficient for both pristine and mechanically damaged cartilage. Note that data along these lines were reported for PEO and pristine cartilage.[102] However, the viscosity of SF, under the shear rates considered in our experiments, while slightly larger than that of PBS, is much lower than that of PBS solutions containing HA and PEO (see Materials and Methods). Thus viscosity alone cannot explain our data.

Our QCM-D results show that neither HA nor PEO strongly adsorb on collagen type II, under the experimental conditions considered. We point out that the HA concentration in the formulations used in our QCM-D experiments (1 mg/ml) is within the range of HA concentration in human SF.[123, 124] The lack of HA adsorption on collagen is likely due to electrostatic repulsions between negatively charged collagen

and anionic HA molecules. The fact that HA and PEO do not seem to adsorb on collagen adlayers suggests, but cannot prove, that boundary lubrication is not responsible for the low friction coefficients measured in the presence of these two lubricants. In fact, experiments by others show that HA provides lubrication via a boundary mechanism.[5] QCM-D observations could complement other investigations available in the literature conducted to identify lubrication mechanisms in cartilage.[88, 108, 125]

The QCM-D results collected for SF show evidence of adsorption on collagen. This adsorption is most likely due to lubricin, as it has been reported that lubricin concentration is higher on cartilage than in SF[107] and that lubricin yields networks on cartilage surfaces.[80] The QCM-D results are also consistent with a reconstruction of the collagen molecules within the adlayer, which could occur as a consequence of SAPL or lubricin adsorption. Following this rearrangement, the collagen adlayer becomes stiffer, maybe loses some collagen molecules, and some of the water molecules trapped within the adlayer are expelled. These results are consistent with boundary, but also with interstitial fluid pressurization lubrication mechanisms, as SF could increase the interstitial fluid osmotic pressure and affect the cartilage permeability to interstitial fluid.

In conclusion, our results suggest that several phenomena contribute to lubricate cartilage. The tissue is highly hydrated, favoring the pressurization of interstitial fluid pressurization. This mechanism can be enhanced by increasing the viscosity of the interstitial fluid, and maybe also via interactions between compounds present in the

interstitial fluid and the molecular components of cartilage. A detailed understanding of such phenomena will allow researchers to manage mild osteoarthritis.

4. Interactions between Single Walled Carbon Nanotubes (SWNTs) and Phospholipid Bilayers

4.1 Introduction

Carbon nanotubes (CNTs), a member of the carbon allotropes family, are constituted of cylinders of graphene sheets, open or closed at the extremities. CNTs can be either single walled carbon nanotubes (SWNTs), which have diameters in the range of 0.4-2.0 nm and lengths of a few micrometers, or multi-walled carbon nanotubes (MWNTs), which have diameters and lengths up to 100 nm and several micrometers, respectively. Both SWNTs and MWNTs exhibit unique physical, chemical, and electrical properties that made them an attractive material for electronic applications, medical diagnostics and drug delivery.[42, 43] Experimental data suggests that CNTs can deliver drugs, antigens, and genes into both prokaryotic and mammalian cells[58, 60, 126-129]. CNTs translocate the plasma membrane of human cell lines such as HeLa and epithelial carcinoma cells.[57, 130]

The enthusiasm for using CNTs in medical applications was mitigated by reports on their toxicity. For example, SWNTs exhibit cytotoxicity to human[51, 52] and animal cells[53, 54]. Besides in vitro experiments, Lam et al. conducted experiment in vivo and found that pristine hydrophobic CNTs accumulated in the lungs of rats, and possibly cause granulomas[53].

As the literature on the subject evolves, experimental results have indicated that the toxicity of CNTs relies on multiple factors, including the purity and the type of CNTs, their functionalization,[54-56] and possibly both cell-culture media and cell type

used in the experiments.[57, 58] Crouzier et al.[59] reported that purifying SWNT significantly reduced the lytic effect on red blood cells. Kang et al.[131] assessed the antibacterial effects of well-purified and characterized CNTs towards Escherichia coli and found that SWNTs were much more toxic than MWNTs. An interesting follow up study by Vecitis et al.[132] took advantage of recent developments in density gradient ultracentrifugation techniques for the separation of metallic and semi-conductive SWNTs of similar length and diameter. When samples containing <5%, ~30%, or >95% metallic SWNTs were compared, the authors found that the cytotoxicity towards Escherichia coli increased with the fraction of metallic SWNTs.

Experiments also suggested, perhaps not surprisingly, that the type of CNT functionalization affected cellular uptake, maybe even changed the uptake mechanism.[60, 61] Singh et al.[62] synthesized twelve polyamine-modified SWNTs and MWNTs, most of which showed reduced cytotoxicity for human lung epithelial A549 cells exposed to the CNTs for 24 and 72 hours. Some of these CNTs managed to efficiently complex siRNA, as assessed by gel electrophoresis, and were internalized by A549 cells, reinforcing the possibility of using these materials for gene delivery and silencing. Although chemical functionalization appeared to alleviate the cytotoxicity of CNTs, surfactants may not provide such a benefit. In an interesting comparative study, Liu et al.[63] studied the cytotoxicity of SWNTs to bacteria. They dispersed SWNTs using both the nonionic surfactant Tween 20 and the anionic surfactant sodium cholate (SC). Tween 20 was found not to be cytotoxic, while SC was found to decrease the bacteria survival rate. It would be interesting to understand why chemical

functionalization of the CNTs reduces their cytotoxicological properties, while physical functionalization using surfactants does not yield similar effects.

The results summarized above suggest that significant progress is being made in understanding the toxicity of CNTs on living cells. Unfortunately, the phenomenon is still not completely understood and sometimes even contradictory results are reported. Taking the effect of SWNT aggregation on cytotoxicity as an example, Liu et al. reported that individually dispersed SWNTs were more toxic than bundled or aggregated SWNTs;[63] while Mutlu et al. found that the toxicity of SWNTs was attributable to their aggregation.[64]

A number of detailed theoretical studies have been conducted to investigate the interaction between CNTs as well as that of other nanomaterials, and phospholipid membranes, specifically phospholipid membranes, in order to understand from a fundamental point of view the experimental data summarized above. For example, Wallace and Sansom[133] simulated one CNT moved at constant velocity across a di-palmitoyl-phosphatidylcholine (DPPC) bilayer and found that as the CNT pierced the membranes it extracted lipid molecules from the bilayer. The lipid molecules could adsorb on the exterior as well as in the interior of the CNT, suggesting the possibility of pore blocking due to the lipid molecules. Hofinger et al.[134] recently simulated CNTs in the phospholipid bilayers. The nanotubes were found to preferentially reside within the membrane. When the CNTs were short (length of 2nm), they aligned parallel to the lipid molecules (perpendicular to the membrane), but as the nanotube length increased the CNTs preferentially placed parallel to the membrane. A few experimental studies have also been conducted to document the interactions between nano-materials and

phospholipid membranes. For example, Rasch et al. reported cryogenic TEM images that prove that gold nanoparticles can be loaded within liposome membranes.[135] Karchemski et al. found that surface functionalized CNTs could conjugate to liposomes by an amide bond between the carboxylic groups from functionalized CNTs and the amine groups from the L-α-phosphatidylethanolamine, using cryogenic TEM.[136]

To complement the data available in the literature, we have conducted experiments to study the interaction between SWNTs and phospholipid membranes. The phospholipid membranes, prepared in the form of liposomes, are considered as a minimal model for cellular membranes. The nanotubes will be purified and characterized to the best of our abilities, to prevent effects due for example to impurities from interfering with the interpretation of our results. The SWNTs are stabilized in aqueous dispersions using the surfactant sodium dodecyl benzene sulfonate (SDBS). To separate the effect of SDBS on the liposomes, dialysis experiments and a number of control tests are conducted. Because SDBS is effective at stabilizing aqueous dispersions of carbon nanotubes at low ionic strength, our experiments are conducted at such conditions. Preliminary experiments in phosphate buffer saline (PBS) lead to SWNTs precipitation. We seek to answer the question: Is it possible that SWNTs, dispersed in aqueous solutions, adsorb into phospholipid membranes and eventually disrupt them? Understanding how SWNTs interact with phospholipid membranes will both contribute to preventing adverse health effects due to SWNTs, and enable the applicability of SWNTs in advanced scientific areas such as controlled drug delivery and/or gene and cancer therapy.

4.2 Experimental Procedures

4.2.1 Materials

The high purity SWNTs (CNT>98%, SWNT 80-95%, (6,5) SWNT 30-40%) were provided by SouthWest Nanotechonologies Inc. (SWeNT). They were used as received without further purification. However, please note that the residual catalysts in the sample can be removed during the dispersion treatment of SWNTs.[137] The average diameter of the SWNTs present in the samples used for our experiments is ~0.8nm, as estimated based on their chiralities.

Egg L-α-phosphatidylcholine **(**egg-PC) and cholesterol were purchased from Avanti Polar Lipids Inc. (purity>99%). Calcein dye and sodium dodecyl benzene sulfonate (SDBS) (purity>98%) were purchased from Sigma-Aldrich and Tokyo Kasei Kogyo Co. Ltd., respectively, and used as received.

Sephadex-25 desalt columns (HiTrap^{TM}) were purchased from GE Healthcare. Dialysis membranes with the molecular weight cut off of 8,000-10,000 were obtained from spectrum laboratories Inc. 18.2 MΩ cm resistivity water was used for all applications in this work. All other chemicals were obtained from Sigma-Aldrich.

4.2.2 Preparation of Liposome Suspensions

The liposome suspensions for dialysis were prepared following a sonication method.[138, 139] In the sonication method 20mg egg L-α-phosphatidylcholine (egg-PC) and 2mg cholesterol were mixed in 5mg chloroform in a glass tube. Then the chloroform was removed under a nitrogen stream at room temperature to obtain a dry

film of lipid mixture. The dry film of lipid mixture was kept under vacuum to avoid oxidation as well as further remove chloroform and other impurities. Prior to use the dry lipid film was hydrated using 22ml water for 30 minutes followed by 30 minutes sonication using a horn sonic dismembrator at 25% power output (Model 500, Fisher Scientific). The 1mg/ml liposome suspension was finally extruded through a polycarbon membrane with the pore size of 400nm (Avanti Polar Lipids Inc.) at room temperature to obtain the liposome suspension.

The liposomes for dye-leakage experiments were prepared following a freeze/thaw process.[140] The freeze/thaw method is described below in the section 4.2.5.

All liposomes were composed of egg-PC and cholesterol. PC is the major component of biological membranes. Cholesterol is used to increase the stability of the phospholipid bilayer.[141, 142]

4.2.3 Preparation of SWNT Dispersions

SWNTs were dispersed in water using the sonication method proposed by Tan and Resasco[143]. 5mg of SWNTs and 125mg of SDBS were added to 25ml of water in a 95ml vial. The aqueous system was sonicated for 1 hour with a horn sonic dismembrator at 25% power output (Model 500, Fisher Scientific). The suspension was then centrifuged in an automatic centrifuge (Centrifuge 5424, Eppendorf) at 15,000 rpm for 30 minutes. Then the upper supernatant dispersion was collected and further processed with a second cycle of sonication and centrifugation. The upper supernatant dispersion collected after the second centrifugation was used as the SWNT dispersion

for our experiments. The SWNT dispersions so obtained were used within the first 2 weeks after preparation.

4.2.4 Dialysis

We attempted to remove SDBS by the dialysis method to minimize the effects of surfactants on liposomes and therefore to study exclusively the interactions between liposomes and pristine SWNTs. Several dialysis experiments were conducted, including (a) mixtures containing liposome suspensions and SWNT dispersions (LIPO+SWNT); (b) mixtures containing water and SWNT dispersions (W+SWNT); and (c) mixtures containing water and 5mg/ml SDBS aqueous solutions (W+SDBS). The aqueous solution of 5mg/ml of SDBS was used because the SWNT dispersions were prepared with the same SDBS concentration. All the above mixtures were produced by combining a 1:1 volume ratio (e.g., 1 ml of water and 1 ml of SWNT dispersion). A fourth dialysis set of experiments (d) was conducted by mixing the liposome suspension and the SWNT dispersion at the volume ratio of 4:1 (4_LIPO+SWNT).

2ml mixtures of LIPO+SWNT, W+SWNT and W+SDBS or 1.25ml mixture of 4_LIPO+SWNT were dialyzed through dialysis membrane (hydrophilic cellulose ester membrane, purchased from Spectrum$^{@}$ Laboratories Inc.) in 200ml water, respectively, under gentle shaking. The molecular weight cut off of the dialysis membrane was 8,000-10,000, which should allow SDBS molecules to diffuse across the membrane while preventing the cross of both SWNTs and liposomes.

During the dialysis experiment the SDBS concentration in the bulk water was monitored by UV-vis spectrophotometer (UV-2450PC, Shimadzu) at the wavelength of

223nm. We will monitor the absorbance intensities at 223nm in the bulk as a function of dialysis time. The SDBS concentration can be calculated based on its absorbance intensity. By knowing the initial SDBS concentration of inside the dialysis cell before dialysis, the liquid volume within the dialysis cell, the liquid volume of the bulk water out of the dialysis cell, and the change of SDBS concentration in the bulk water out of the cell during the experiment, we calculated the SDBS concentrations inside the dialysis cell.

4.2.5 Dye-leakage from Liposomes

To monitor the disruption of liposomes, we encapsulated a fluorescent dye (calcein) within liposomes for conducting leakage measurements. 2.5ml chloroform solution containing 10mg egg-PC and 1mg cholesterol was mixed in a 10ml round-bottom flask. Chloroform was then removed at room temperature using a nitrogen stream, while forming a dry film of lipid mixture. The dry film was kept in a vacuum chamber to avoid oxidation as well as further remove cholesterol and other impurities. The dried film was then hydrated with 2ml 40mM aqueous calcein solution for 30 minutes. The calcein aqueous solution was adjusted to pH=~7.4 by sodium hydroxide before being used. The mixture was vortexed for 3 minutes and then subjected through five cycles of freeze/thaw by using liquid nitrogen and warm water. In between each cycle, the solution was sonicated using a bath sonicator (Model 08855-10, Cole Parmer) for 1 minute. After the five freeze/thaw processes, the liposome suspension was extruded through a polycarbon membrane with pore size of 400 nm (Avanti Polar Lipids Inc.) at room temperature. The non-trapped calcein was removed by eluting

through a size-exclusion Sephadex G-25 column. The liposome suspension collected from the exclusion column was diluted 10-fold with water prior to any leakage experiments.

Calcein leakage from the liposomes was monitored by recording the increase of fluorescence intensity at 528nm (excitation at 495nm, slit width 20) using a plate reader (Synergy HT, Bio-Tek), after adding 5μl reagent to 300μl of liposome suspension. Pure water, 0.2% Triton X-100 (polyoxyethylene 10 isoctylphenyl ether) in aqueous solution, SDBS in aqueous solution, SWNT dispersions, and SWNT dispersion with a low SDBS concentration were used as additions. The SWNT dispersion with a low SDBS concentration was obtained by a 4-day dialysis of 2ml W+SWNT sample in 200ml water. Triton X-100 was chosen to conduct a control experiment because this surfactant is known to disrupt phospholipid bilayers, hence causing calcein leakage.[140]

To calibrate the calcein leakage results, we used two test experiments. The first was expected to show no leakage, the second is expected to show maximum leakage. In the first experiment 300μl of the liposome suspension were added to 5μl of pure water. The results showed no change of fluorescence intensity within 4 minutes, and the correspondent fluorescence was used to define 0% leakage. Complete liposome disruption was achieved by adding 5μl of the 0.2% Triton X-100 aqueous solution to 300μl of the liposome suspension. The fluorescence reading intensity after 4 minutes was used to benchmark '100% leakage'. The leakage readings obtained during other experiments are reported below as "% leakage", which is the fraction of the total leakage caused by Triton X-100.

4.2.6 Characterization Techniques

SWNTs were characterized by UV-vis (UV-2450PC, Shimadzu) and Raman spectroscopies (JY Horiba LabRam 800). The Raman spectrum was detected using dry SWNTs after sonication. To prevent interference, excess SDBS was removed by a 4-day dialysis. NIR fluorescence spectra were measured with a NS2 nanospectralyzer (Applied NanoFluorescence, Houston, TX) to determine the dispersion quality of SWNT dispersions. The results were obtained using 532nm and 783nm diode laser excitations.

Dynamic light scattering (DLS) was employed to estimate the size of liposomes in water. Transmission electron microscopy (TEM) with negative stain was used to visualize liposomes in water. For the TEM with negative stain method, lacey carbon copper TEM grids (Electron Microscopy Sciences) were used to adsorb liposomes from the liposome suspension. The liposome samples were then stained in 2 % uranyl acetate aqueous solution for 30 seconds and dried at room temperature. The specimens were observed on a JEOL JEM-2000FX instrument with an accelerating voltage of 200kV.

The freeze-fracture TEM was used to visualize systems composed by liposomes and SWNTs in water. The samples used for these experiments were LIPO+SWNT on the 4^{th} day of dialysis. Freeze-fracture samples were prepared by plunging the sample into a liquid Freon 22 bath cooled by liquid nitrogen. This process is expected to vitrify the water inside the sample. The samples were then fractured in vacuum with a microtome. The fractured samples were replicated with approximately 5nm platinum deposition at a 45 degree angle, followed by ~100nm carbon deposition normal to the surface. The replicas were dissolved in chromic acid (50% sulfuric acid, 10% sodium

dichromate and water) at room temperature for about 24 hours, and then washed in distilled water 3 times to removed residual impurities before being collected on copper TEM grids (Electron Microscopy Sciences). The specimens were then analyzed using a JEOL JEM-2000FX instrument with an accelerating voltage of 200kV.

4.3 Results and Discussions

4.3.1 Liposome Suspensions

One picture of one liposome suspension in which the liposomes are composed of egg-PC and cholesterol following the sonication method is shown in Figure 4-1 A. The sample exhibits the opalescence characteristic of liposome suspensions. Because the liposomes are roughly spherical, dynamic light scattering (DLS) was used to estimate their size. The results show that the average diameter of the liposomes from at least 10 different batches is ~150±40nm. According to the literatures, the liposomes which have the diameter of 200nm or smaller should represent uni-lamellar liposomes.[135] Figure 4-1 B is a TEM image of liposomes using the negative stain method. The diameters of the liposomes observed in TEM images are consistent with the estimates from DLS experiments, although a wide range of diameters are observed, from ~20nm to ~400nm. However, visual inspection of the TEM images suggests that liposomes larger than 250nm are very few in our samples. The liposomes made from the freeze-thaw method have a similar average diameter to those from the sonication method after the column extrusion (data not shown for brevity).

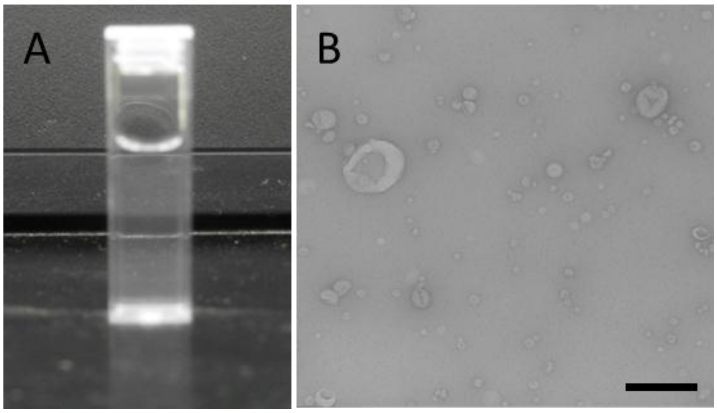

Figure 4-1 Picture of one sample containing a liposome suspension prepared by sonication method (A). TEM image of liposomes with negative stain method (B). The scale bar on the right panel is 200nm.

4.3.2 SWNT Dispersions

One picture of an aqueous dispersion containing SWNTs stabilized by SDBS is shown in Figure 4-2 A. Most SWNTs in the dispersion are expected to be individual or in small bundles according to the literature.[143] The SWNT dispersion is stable in the presence of SDBS for as long as 2 months. For consistency, all the SWNT dispersions used in the present work were used within 2 weeks after preparation to ensure high dispersion quality. One representative Raman spectrum obtained from the dry SWNTs after sonication is reported in Figure 4-2 B. Raman spectroscopy is typically employed to evaluate the quality of SWNTs and to estimate the presence of defects based on two characteristic bands, an intense band centered below 1600cm^{-1}, typical of sp2 carbon atoms (G band), and a smaller band centered at around 1300cm^{-1}, typical of sp3 carbon atoms and associated with defects (D band). In our case, the G/D band ratio is very high, indicating a low amount of impurities and imperfections in the SWNTs used for the present work. Typical UV-vis absorption spectra obtained from our SWNT

dispersions show the characteristic peaks of (6,5) SWNTs centered at ~567nm and ~978nm (see Figure 4-2 C). Because the majority of SWNTs in the samples used in our experiments are (6,5), we will only track the featured peaks of (6,5) SWNT in the SWNT dispersion, assuming the results of (6,5) SWNT can represent for all SWNTs.

It is worth mentioning that, according to our experiments, egg-PC lipids do not disperse SWNTs in water as effectively as SDBS.

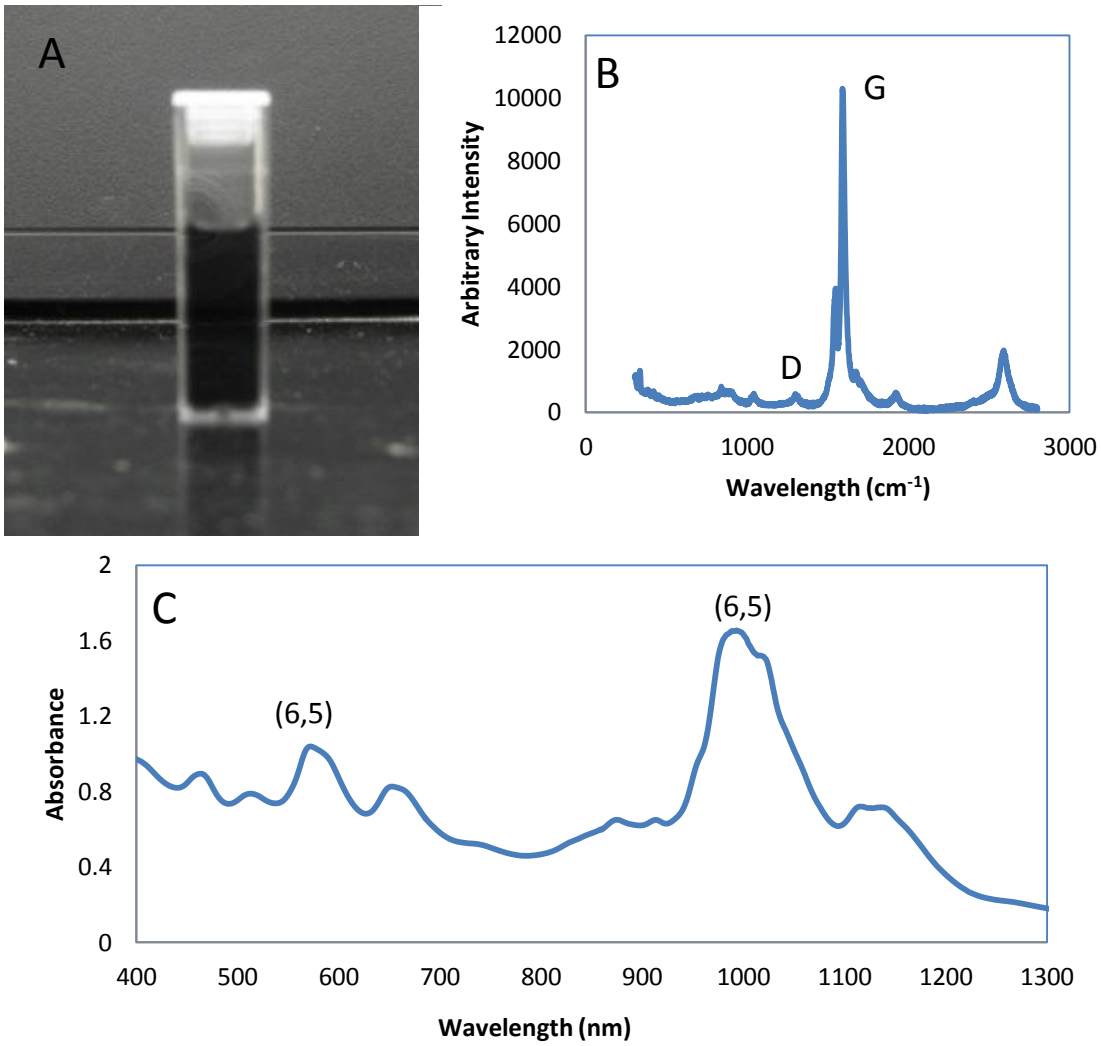

Figure 4-2 Picture of a cuvette containing an aqueous dispersion of SWNTs stabilized by SDBS surfactants (A). Representative Raman spectrum of dry SWNTs after sonication (B). Representative UV-vis absorption spectrum of an aqueous SWNT dispersion (C). Highlighted are the peaks representative of the D and G bands in panel B and those characteristic of (6,5) SWNTs in panel C.

4.3.3 Dialysis

In Figure 4-3 we provide visual pictures of the dialysis cells containing either W+SWNT (panels A1 to A3) or LIPO+SWNT samples (panels B1 to B3). Panels 1, 2, and 3 are obtained at different times during the dialysis experiments. Explicitly, panels

A1 and B1 are representative images of the samples as prepared, before the dialysis is initiated. The pictures in panels A2 and B2 are obtained on the 5th day of dialysis, and those in panels A3 and B3 are obtained at the end of the dialysis experiment, and they represent the dialysis membranes with no dispersion. In Figure 4-3 A1 and B1, the two mixtures look similar to each other before dialysis. In Figure 4-3 A2 we found the agglomeration of SWNT from the W+SWNT sample on the 5^{th} day of dialysis. No visible agglomerates of SWNT were observed in the first 4 days of dialysis for the W+SWNT system. One picture of stable dispersion of SWNT from LIPO+SWNT sample on the 5^{th} day of dialysis is reported in Figure 4-3 B2. The SWNT dispersion with liposomes in Figure 4-3 B2 is stable for about one month at ambient conditions without the formation of visible agglomerates. Figure 4-3 A3 and B3 are obtained from the dialysis cells after removing the solutions in A2 and B2. The results show that there are no visible SWNT agglomerates on the dialysis membrane.

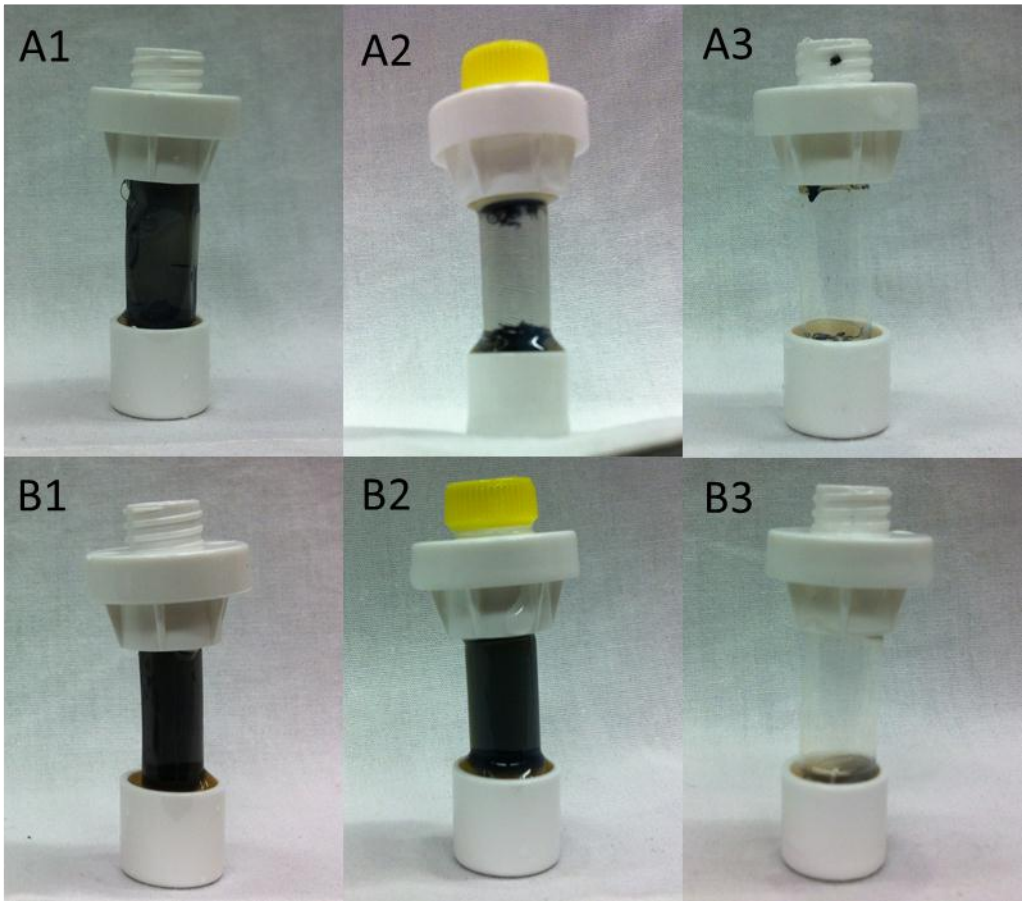

Figure 4-3 Pictures of W+SWNT (panels A1 to A3) and LIPO+SWNT samples (panels B1 to B3) before, during, and after dialysis. Pictures A1 and B1 are the two samples within the dialysis cells before dialysis; pictures A2 and B2 are for the two samples on the 5th day of dialysis; pictures A3 and B3 are for the dialysis cells after the SWNT dispersions of panels A2 and B2 have been removed. See section 4.2.4 for details on system composition.

We employed UV-vis spectroscopy to monitor the concentration of SWNTs, liposomes, and SDBS in the bulk water outside of the dialysis cell. The representative peaks are centered at ~567nm for (6,5) SWNTs,[143] at ~205nm for egg-PC,[144] and at ~223nm for SDBS.[145] Not surprisingly, we did not observe the characteristic absorbance of (6,5) SWNTs and egg-PCs in the bulk solution. This observation is

consistent with the fact that the dialysis membranes do not allow either liposomes or SWNTs to diffuse out of the dialysis bag.

The concentration of SDBS in the bulk water can be determined by the maximum absorbance at 223nm. We first obtained a standard calibration curve for SDBS concentration (shown in Figure 4-4). The curve shows linearity up to the concentration of 0.06mg/ml (the nonlinear part observed at higher SDBS concentration is not shown for clarity), which is consistent with literature.[145] For all systems considered, except 4_LOPO+SWNT, the maximum SDBS concentration in the bulk water is estimated in 0.025mg/ml under the assumption that all SDBS used to stabilize the SWNTs diffuse out of the dialysis cell. This observation guarantees that UV-vis SDBS absorbance in the bulk water during our dialysis experiments is within the linear region of the calibration curve shown in Figure 4-4.

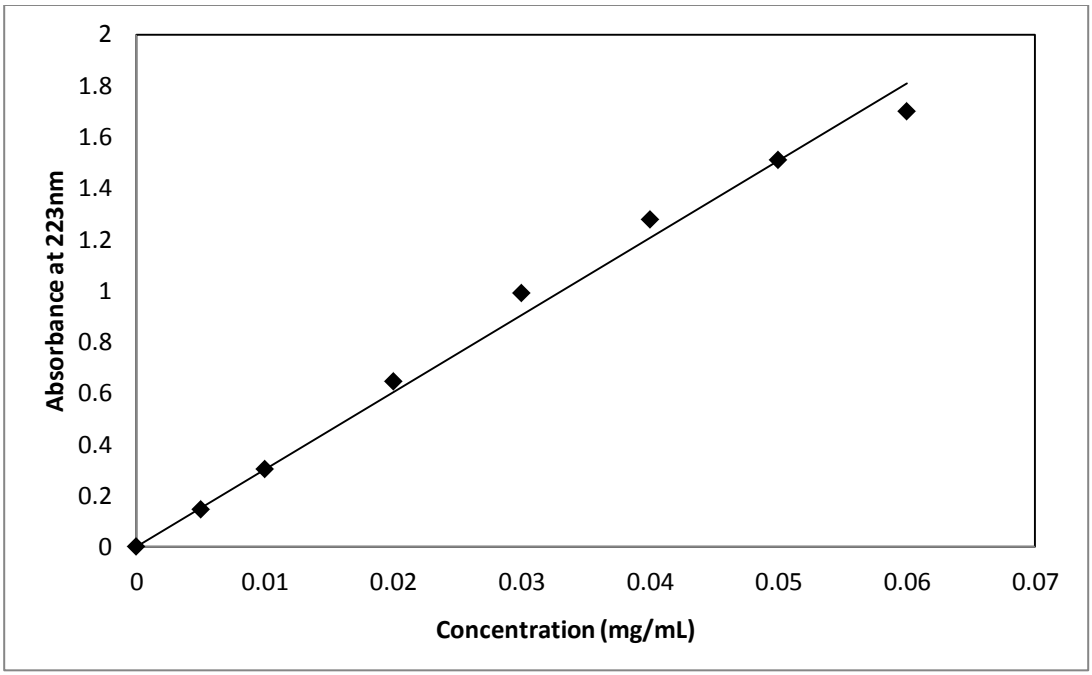

Figure 4-4 Standard calibration curve for the absorbance at 223nm vs. concentration of SDBS in water, as obtained by UV-vis spectrometer.

In Figure 4-5 top panel we reported the absorbance at 223nm in the bulk as a function of dialysis time. The SDBS concentration on the 10th day of dialysis for all 1:1 mixtures is ~0.025mg/ml, which corresponds to the absorbance intensity of ~0.82 at 223nm (Figure 4-5 top panel). For the 4_LIPO+SWNT sample, the absorbance in the bulk water is about ¼ of that from 1:1 mixtures. In all cases, the absorbance intensities increase linearly as the dialysis time increases until reaching about 90% of the maximum value in the first ~90 hours (4th day of dialysis). The result suggests most of the SDBS molecules diffused out the dialysis cell in the first 4 days of dialysis. After about 100 hours, the change of absorbance becomes little, indicating that the equilibrium state is being approached. The results shown in Figure 4-3 suggest that SWNTs start agglomerating dramatically after the 4th day of dialysis (large

agglomerates of SWNT appear on the 5th day of dialysis). For consistency, all experiments below were conducted using the samples on the 4th day of dialysis.

In Figure 4-5 bottom we report the SDBS concentration inside the dialysis cell as a function of dialysis time. The experiments in Figure 4-5 reveal that at ~90 hours the SDBS concentration within the dialysis cells is lower than the critical micelle concentration (cmc) of SDBS in water (~0.7mg/ml).[146] This observation suggests that SDBS surfactants are not effective at stabilizing SWNTs in water when the SDBS concentration is lower than its cmc. Matarredona et al. studied the adsorption isotherm of SDBS on the SWNTs.[147] The adsorption isotherm suggests that adsorbed SDBSs per SWNT under the cmc are only about 1% of that from at or above the cmc (~70mmol/g SWNT). Using their adsorption isotherm curve, we calculated SDBS adsorbed on SWNTs in our experiments at 0.5mg/ml is less than 1% of the total SDBS in the dialysis system.

After ~150 hours of dialysis, SDBS concentrations inside the dialysis cells for all cases are very low. Although at these conditions SDBS cannot stabilize SWNTs in water (there are simply not enough surfactant molecules), our results suggest that the presence of liposomes can prevent SWNTs from bundling in water at very low SDBS concentration.

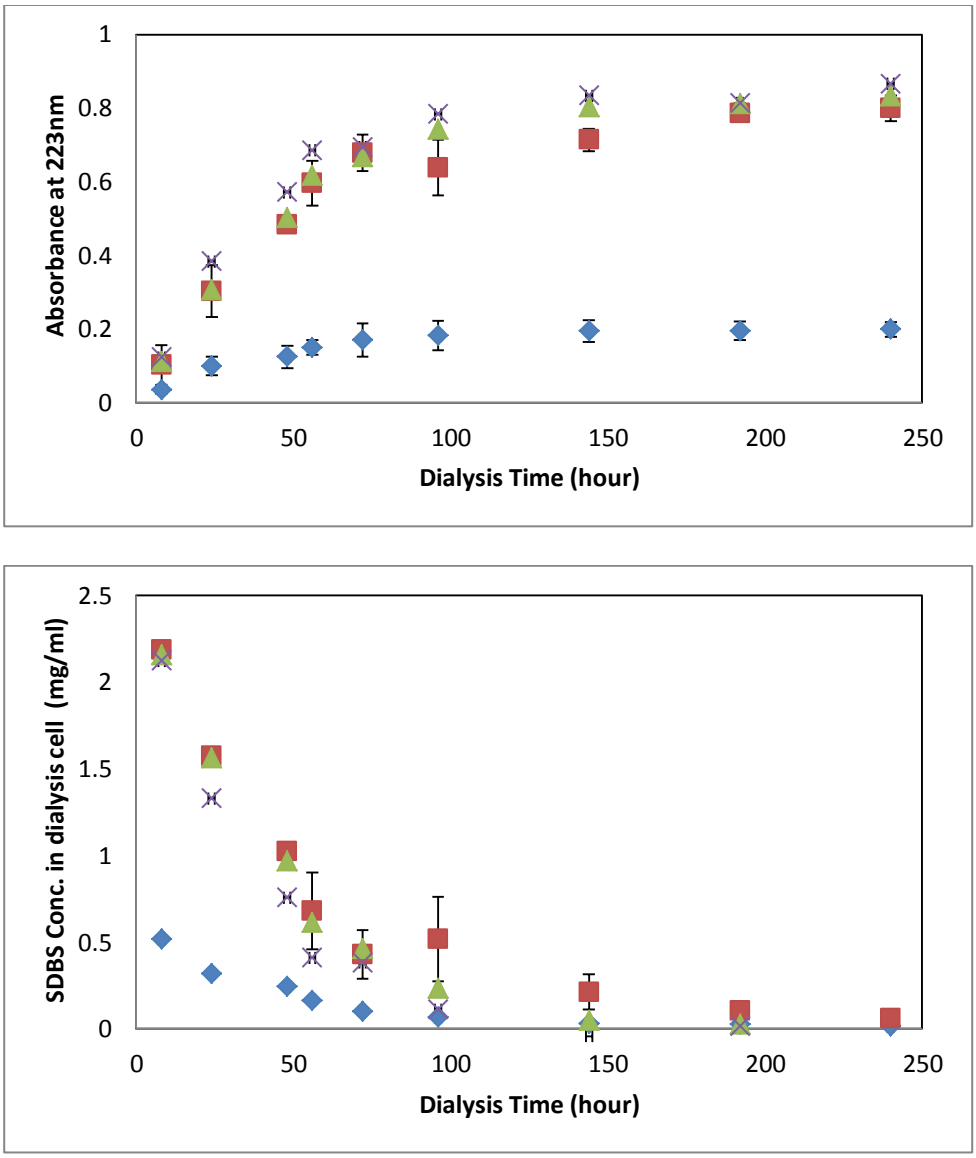

Figure 4-5 Absorbance at 223nm in the bulk out of dialysis cell (top panel) and SDBS concentration inside the dialysis cell (bottom panel) as a function of dialysis time. For clarity, only representative error bars are reported. Different symbols are for experiments conducted for different systems. Green▲ represents W+SDBS; purple x represents W+SWNT; red ■ represents LIPO+SWNT; blue ♦ represents 4_LIPO+SWNT. See section 4.2.4 for details on system composition.

Although agglomerates of SWNT were not observed from the LIPO+SWNT samples after one month or longer, it is arbitrary to conclude that individual SWNTs do not bundle during dialysis. The intensity of the fluorescence emission from SWNTs can quantify the dispersion quality of a SWNT sample.[148, 149] The fluorescence emission spectra from the W+SWNT and LIPO+SWNT samples are reported in Figure 4-6. The blue curve is from the W+SWNT sample before dialysis, which corresponds to the well-dispersed SWNT system. The fluorescence intensities from the W+SWNT sample on the 4^{th} day of dialysis (green) are quenched by almost 40% in comparison to those from the W+SWNT sample before dialysis. The result suggests low dispersion quality and bundle formation on 4^{th} day of dialysis. This result is consistent with the observation of aggregates of SWNT on the 5^{th} day of dialysis, and it suggests a nucleation and growth process for the SWNT bundles within the W+SWNT sample when the SDBS concentration is low. The intensities of fluorescence emission from the LIPO+SWNT sample obtained on the 4^{th} day of dialysis are similar to those from the LIPO+SWNT sample before dialysis (red and purple lines), indicating well-dispersed SWNTs in both systems. This finding confirms that the presence of liposomes prevents SWNTs from bundling even at very low SDBS concentration.

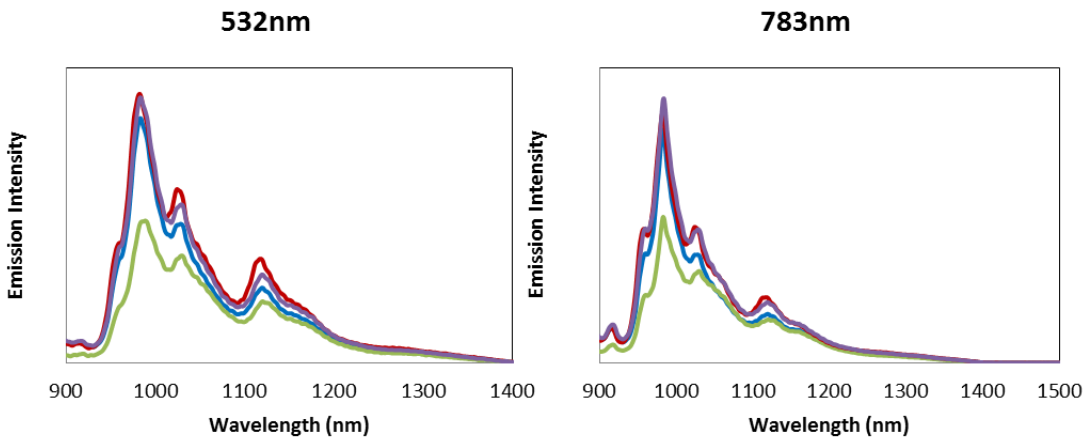

Figure 4-6 Fluorescence spectra of different SWNT systems. Different lines are for results obtained for different systems. Blue is for the W+SWNT sample before dialysis; purple is for the LIPO+SWNT sample before dialysis; green is for the W+SWNT sample on the 4th day of dialysis; red is for the LIPO+SWNT sample on the 4th day of dialysis. The results are obtained from excitation lasers at 532nm and 783nm (left and right panels, respectively). See section 4.2.4 for details on system composition.

SDBS is expected to disperse SWNTs by the ability to orient the SDBS head groups perpendicularly to the SWNTs axis, promoting long-ranged repulsive forces.[143, 150] Egg-PC does not disperse SWNTs as efficiently as SDBS according to both literature[151, 152] and our own experiments (results not discussed for brevity). One very distinct possibility that causes liposomes to stabilize SWNT dispersion is that that SWNTs interact with liposome membranes. Our hypothesis is that when SWNTs are wrapped with SDBSs, the interaction is due to electrostatic force between choline groups from liposomes and sulfonate groups from SDBS. When there are not enough SDBSs on the surfaces of SWNTs, the SWNTs can embed in the hydrophobic inners of the liposome membranes. Should liposomes adsorb onto SWNTs, they could prevent SWNTs from bundling by steric resistance.

For completeness, we point out that SDBS concentration after dialysis reported above is ~0.025mg/ml for 1:1 mixture and 0.006 for 4:1 mixture. However, SWNTs agglomerates were observed from the dialysis experiments (not shown here) in which we completely removed SDBS or reduced the concentration of liposomes. It is likely that the stable SWNT dispersion needs a minimum ratio of liposomes to SWNTs and a minimum SDBS concentration. Unfortunately, the minimum SDBS concentration necessary to stabilize SWNT dispersions in water cannot be unequivocally determined from our experiments. Statistical analysis of such results is beyond the scope of the present work but could be interesting to investigate in the future.

4.3.4 Freeze-Fracture TEM

Representative TEM images of the replicas made from LIPO+SWNT samples are shown in Figure 4-7. The replicas were obtained from samples on the 4^{th} day of dialysis. Because the replica is the coating of platinum and carbon on the fractured frozen sample, TEM images of replicas can provide evidence of how SWNTs and liposomes are structured in water. The available TEM images corroborate our earlier interpretation that liposomes interact with SWNTs in water at low SDBS concentration as discussed above. In the bottom left of Figure 4-7 there are linear dark and shadow (white) areas on the top surface of the liposome (marked by the arrow). The dark area is caused by the platinum accumulation. The shadow (white) area indicates no platinum is in this area. Thus, the linear shape is due to the presence of SWNTs on the top of the liposome. In the top left of Figure 4-7 we report one SWNT interacts with the side membrane of a liposome. In this case, the image of SWNT is not from platinum accumulation but from

the coating of carbon. In the right of Figure 4-7 one SWNT interacts with 2 different liposomes. It is important to point out that the diameter of the SWNT on the replica cannot be determined from the platinum accumulation. For the SWNT image from carbon depositions, the diameter of the SWNT on the replica is larger than that of the original SWNT. Thus, although the observed SWNTs in Figure 4-7 look like large bundled SWNTs based on their diameters, they are possibly individual SWNTs or small bundles. The observed liposomes which interact with SWNTs are nearly spherical, suggesting the interaction between SWNTs and liposomes do not cause strong rearrangement of liposome structures or break the liposomes. Although the freeze-fracture TEM images cannot distinguish if SWNTs are located in or out of the phospholipid bilayers of liposomes, our hypothesis is that SWNTs adsorb on the surface of liposomes. First of all, comparing the size of liposomes and the length of SWNTs obtained from the TEM images, SWNTs in this work are too long to embed in the liposome membrane. Even if SWNTs can embed in the phospholipid bilayer, only a small portion of one SWNT can embed in the liposome membranes. Secondly, if SWNTs are located in the liposome membrane, it should change the shape of liposomes which conflicts with our observations. The orientation of SWNTs is generally parallel to the liposome membrane based on the available TEM images.

The freeze-fracture TEM experiments still need improving. More TEM images from LIPO+SWNT samples before dialysis and with longer dialysis time are necessary to complete our interpretations.

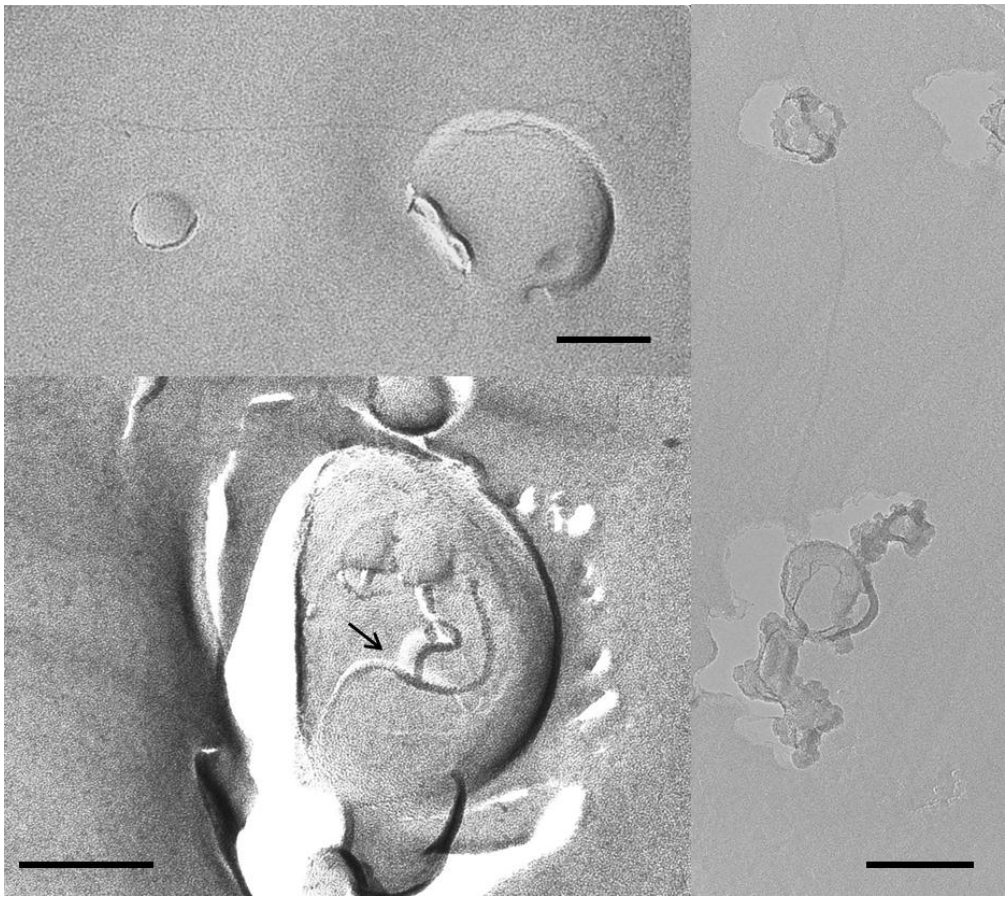

Figure 4-7 Freeze-fracture TEM images of the LIPO+SWNT sample on the 4th day of dialysis. The dark area is caused by the platinum accumulation. The shadow (white) area indicates no platinum is in this area. The highlighted arrow indicates the image of SWNTs. The scale bars are 100nm.

4.3.5 Dye-Leakage from Liposomes

During the dye-leakage experiments we added 5µl SWNT dispersion to 300µl of liposome suspensions. In Figure 4-8 we report the leakages of calcein within the first 4 minutes after adding different reagents to liposome suspensions. The leakages in the presence of SWNTs start from negative values, because SWNTs absorb a certain amount of both excitation and emission lights and subsequently the fluorescence intensities are lower than that defined as 0% of leakage. The results show that in the

addition of SDBS the leakage increases slightly as the time increases, suggest that SDBS increases the permeability of calcein through liposomes probably by perturbing the liposome membranes. However, the leakage caused by SDBS is much less in comparison to that caused by Triton X-100. The addition of SWNT dispersion also increases the leakage slightly. The increase of leakage by SWNT dispersion is likely due to SDBS, because the increase trend in the addition of SWNT dispersion (crosses in Figure 4-8) is similar to that in the addition of SDBS (triangles in Figure 4-8) and also because the increase trend is hardly observed in the addition of SWNT dispersion with a low concentration of SDBS (empty circles in Figure 4-8). No obvious observation of leakage through liposomes in the addition of SWNTs indicates that the SWNTs do not change the permeability of liposomes, at least in a short time range. The results agree with our early hypothesis that SWNTs only adsorb on the liposomes, but not embed in the liposome membranes.

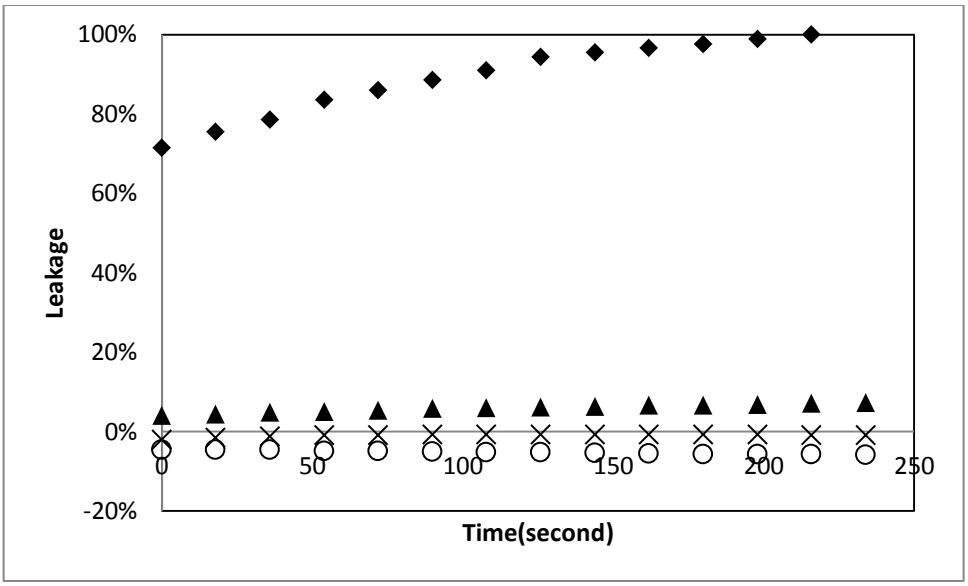

Figure 4-8 Leakage of dye through liposome membranes in the presence of different reagents. Leakage was obtained by measuring the increase of fluorescence from the solution immediately after the addition of reagent. The fluorescence after the addition of water was taken as 0% leakage, and the fluorescence 4 minutes after the addition of Triton X-100 was taken as 100% leakage. The addition of SDBS is▲; the addition of Triton X-100 is ♦; the addition of SWNT dispersion is x; the addition of SWNT dispersion with low concentration of SDBS is ○.

To complete the leakage study, we designed another leakage experiment. In the first step, we combined the liposomes containing calcein and SWNT dispersion with a volume ratio of 9:1 and followed by dialysis. Then the liposome-SWNT mixture was collected on the 4^{th} day of dialysis for a leakage experiment. Only Triton X-100 was added to the liposome-SWNT mixture after dialysis. If there is an increase of leakage, it means the interaction between SWNTs and liposomes during dialysis does not disrupt the structure of phospholipid bilayer very much. If there is no change of leakage, it suggests the perturbation of phospholipid bilayer is significant and increases the permeability of the phospholipid bilayer during the dialysis. As a consequence the

concentrations of dye inside and outside the liposomes are similar after a 4-day dialysis before adding Triton X-100. In Figure 4-9 the addition of Trion X-100 in a liposome-SWNT mixture on the 4th day of dialysis causes a further increase of leakage of calcein, indicating liposome membranes are not dramatically disrupted by SWNTs after a 4-day dialysis. This finding is consistent with the first part of the leakage experiments that the presence of SWNT dispersion does not enhance the permeability of dye through liposome membrane, possibly because SWNTs only adsorb on the liposomes.

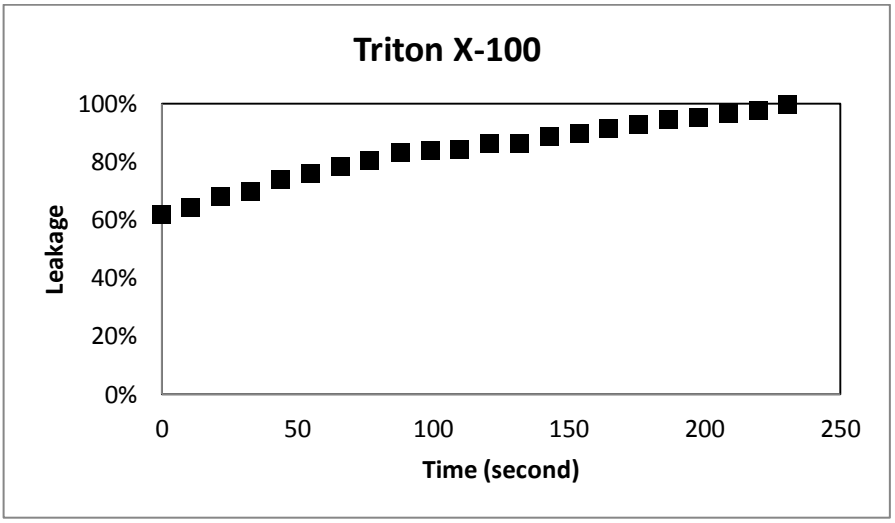

Figure 4-9 Leakage of dye through liposome membranes from the liposome-SWNT mixture on the 4th day of dialysis. Leakage was obtained by measuring the increase of fluorescence from the solution immediately after the addition of Triton X-100. The fluorescence after the addition of water was taken as 0% leakage, and the fluorescence 4 minutes after the addition of Triton X-100 was taken as 100% leakage.

Although most of the liposomes are uni-lamellar liposomes according to their size distribution, the current experiment set up allows the presence of multi-lamellar liposomes (diameter larger than 200nm) in the liposome suspension. We have also done experiments with uni-lamellar liposomes. This experiment is designed to eliminate the

possibility that SWNTs perturb the outer lamellae but not the inner lamellae of liposomes. These uni-lamellar liposomes were prepared by extruding 20 times using a 200nm membrane. The result from uni-lamellar liposomes is generally consistent with the one from Figure 4-9. The result from the uni-lamellar liposome suspension is a complement to the current study, indicating the interaction between SWNTs and liposomes will not break the any phospholipid bilayers of liposomes.

5. Conclusions and Future Directions

5.1 Cartilage Lubricity

The friction coefficient between cartilage surfaces was measured using a pin-on-disc tribometer at constant load of 2N at room conditions. Friction coefficients obtained from different testing configurations were compared. The measured friction coefficient strongly depends on the testing configuration, suggesting that using a commercial pin-on-disc tribometer and by controlling the experimental set up, different lubrication mechanisms can be assessed. The most interesting conclusion is that the friction coefficient measured when the cartilage sample is glued on the disc remains very low as the experiment proceeds (alumina-on-pin vs. cartilage-on-disc (AC) testing configuration), probably because as the pin moves on the cartilage surface (migrating contact area) the pores present in cartilage, although depleted of phosphate buttered saline (PBS) solution when the load is applied, replenish before the load is applied again on the same area. As a consequence the fluid phase supports a large fraction of the applied load, and the friction coefficient remains low. These results suggest that the AC testing-configuration could be used to assess the wear-and-tear characteristics of materials used in prosthetic devices (which should be supported on the pin), as well as possible implants designed to improve lubrication in joints. Based on our analysis, it is expected that when the AC testing configuration is implemented lubrication is provided by interstitial fluid support mechanisms.

Our results show that the friction coefficients measured for both pristine and damaged cartilage samples depend on lubricant solutions. Among the lubricants considered, 100mg/ml of 100,000 Da PEO in PBS appears to be as effective as SF, especially on the mechanically-damaged cartilage. When the steady-states friction coefficients obtained in the AC testing configuration are plotted as a function of the Hersey number, our results are consistent with a Stribeck curve, indicating that the friction coefficient of cartilage depends on the solution viscosity, η, sliding velocity, υ, and normal load, N. Although it is possible that several phenomena contribute to lubricate cartilage, it seems that interstitial fluid pressurization dominates the lubrication of cartilage as long as the tissue is highly hydrated. The interstitial fluid mechanism is enhanced by increasing the viscosity of the interstitial fluid, most likely due to the decrease of permeability of interstitial fluid in cartilages.

In our study, we only considered one polymer, linear PEO, as a potential lubricant for articular cartilage. It works unexpectedly well. Many other polymers, such as pentosan polysulfate, an artificial polymer that has been proposed as potential treatment for osteoarthritis,[153-156] can be added to the present study. It is possible that the friction coefficient of cartilage depends on the molecular structure of polymer in the lubricant solution. More studies need to be done to understand the relationship between friction coefficient and lubricant structure. Different polymer with different microstructures, functional groups, and molecular weights should be considered. Understanding the lubrication mechanism of each component may help us to find a better way to minimize the friction coefficient and abrasion of cartilage by either the combination of different lubricants, or the development of new lubricants.

Even though we employed quartz crystal microbalance with dissipation (QCM-D) to explain the interaction between cartilage and different lubricants, molecular simulations may provide a complementary tool to understand this problem, especially at the molecular level. For example, Momot used Monte Carlo simulations to study water diffusion in an idealized model of articular cartilage.[157] Modeling the molecular interactions between lubricant components and cartilage surface (probably collage type Π molecule) will allow us to know how the lubricant solution interacts with cartilage, which will help us not only distinguish boundary lubricant from others, but also investigate how the complex lubricant systems structure or self-assemble on the cartilage.

The injuries inflicted on the cartilage samples in my work were not representative of typical surface damage observed in osteoarthritic joints (see Figure 1-2). To continue the investigation of lubrication in mechanically damaged cartilage specimens it will be desirable to consider surface injuries that are similar to those observed under physiological conditions. One such injury could be a pinhole. To maximize the effects of surface damage on the measured friction coefficient of cartilage, I suggest to conducting friction experiment by repeating a forward and backward linear sliding on the damaged pinhole of the cartilage.

Because of cartilage loss, osteoarthritic patients usually suffer from significant pain and limited joint motion. So far the most popular commercial treatment is artificial joint replacements. To provide data that are more relevant from a practical point of view, we could replace the alumina samples used in the current work with materials that are actually used in prosthetic devices, for example titanium dioxide.[158] Understanding

the friction and wear between a certain material and cartilage may contribute to material and lubricant designs for osteoarthritis treatment. Our hypothesis is that the artificial material with a deformable porous-permeable structure might be able to produce low sustained friction and wear because of maximizing interstitial fluid pressurization.

In recent years, a lot of researches have focused on promoting cartilage tissue growth to repair the joint of patients instead of relying on complete joint replacement surgeries.[46-49, 159] To treat cartilage defects, a key step is the repair of its damaged extracellular matrix. Surgeons have developed several methods to achieve such a goal. For example, autologous chondrocytes implantation is a cell-based therapy already in clinical use.[160] Because engineered cartilages can be cultured in scaffolds, it will be useful to study the friction between different scaffolds and cartilages. This future study may contribute to the design of scaffold with minimum friction and abrasion. Because eventually engineered cartilage needs to interact with natural cartilage, we can also study the friction between engineered cartilage and natural cartilage.

5.2 Interactions between SWNTs and Phospholipid Bilayers

We sucessfully conducted experiments to study the interaction between SWNTs and liposome membranes via dialysis, freeze-fracture TEM, and dye-leakage experiments. We observed that SWNT dispersions are more stable in the presence of liposomes than in the absence of liposomes at a low SDBS concentration under a gentle shaking condition. Because the dialysis experiments do not allow the determination of the interaction between SWNTs and liposomes directly, we rationalize our results by

freeze-fracture TEM. The results from freeze-farcture TEM show that SWNTs interact with liposomes in water, possibly by adsorbing on to phospholipid bilayers. Sperical liposomes are observed under TEM, suggesting the interaction does not break the structure of liposome. From dye-leakage study, no obvious leakage is found upon the addition of SWNTs to liposome suspensions. This is an indication that SWNTs only adsorb on the liposome membranes and the perturbation of phospholipid bilayer caused by SWNTs is minor. Extending our observations to answer the toxicity of CNTs, it is possible that SWNTs with small diameter could adsorb onto cellular membranes, without disrupting their structure by directly penetration. Our results suggest the possibility of designing new drug-delivery devices based on the preferential interaction between CNTs and phospholipid membranes. In the newly envisioned devices drug-loaded liposomes are adsorbed onto the SWNTs. This device would allow us to load more drug in the liposomes and to use less SWNTs.

There are at least 2 factors to prevent SWNTs from embedding in the phospholipid bilayers in the current experiments. First, the presence of cholesterol enhances the stability of liposome membranes, subsequently may increase the energy barrier for SWNTs to squeeze in the phospholipid bilayers. Second, according to the TEM images, the SWNTs are too long to embed in the liposomes. In the future we should try to make liposomes without cholesterol and chop the SWNTs shorter. Our hypothesis is that short SWNTs may embed in the phospholipid bilyaers and increase the permeability of the liposomes.

Because the thickness of the phospholipid membrane is ~4.3nm, SWNTs embedded in the phospholipid membrane with large diameters may disrupt the structure

of phospholipid bilayer more significantly than SWNTs with small diameters. To test this hypothesis, however, CNTs samples mono-dispersed with the same diameter need to be available. The separation of SWNTs into single chirality remains very challenging. For example, the SWNT in current work has the high purity of SWNT, 80-95%. However, the purity of (6,5) SWTNis only 30-40%. Very recently, Liu e al. reproted a simple and effective method for large-scale chirality SWNTs separation.[161] The purity of SWNT, take (6,5) SWNT as an example, can reach 93%. In the next stage, we can first purify SWNTs and then study the interaction between each type of SWNTs and phospholipid bilayers. It will be useful to study SWNTs with a broad range of chiralities and relate the permeability of phospholipid bilayer to the diameter of SWNT embedded in the bilayer.

Both chemically and physically functionalized CNTs can be used to study their interactions with liposomes. In addition, liposomes can be also prepared with difference components to change their properties, e.g. adding phosphatidylethanolamine, phosphatidylglycerl, phosphatidylserine, etc. It is possible that the surface properties of CNTs and liposomes are critical to determine the reults.

Molecular simulations have been used to study the permeabilities of nanoparticles and drugs through phospholipid bilayers. Many modeling methods are reported, including melecular dynamics and Monte Carlo, at the atomistic and coarse-grained levels.[162-164] According to my knowledge, no simualtion has been done to study the permeability of small molecules (e.g., water or hydrophobic drugs) through phospholipid bilayers in the presence of embedded CNTs. The results from such simulations could be compared to leakage experiments. The investigation of transport

phenomena across phospholipid membranes will contribute to both the fundamental understanding of cellular biology and to the design of controlled drug-delivery devices.

6. References

1. Mow, V.C. and W.C. Hayes, in Chapter 4 'Structure and Function of Articular Cartilage and Meniscus' Basic Orthopaedic Biomechanics. 1997, Lippincott Williams: Philadelphia.

2. Ateshian, G.A., et al., An asymptotic solution for the contact of 2 biphasic cartilage layers. Journal of Biomechanics, 1994. 27(11): p. 1347-1360.

3. Caligaris, M., et al., Investigation of the frictional response of osteoarthritic human tibiofemoral joints and the potential beneficial tribological effect of healthy synovial fluid. Osteoarthritis and Cartilage, 2009. 17(10): p. 1327-1332.

4. Gleghorn, J.P. and L.J. Bonassar, Lubrication mode analysis of articular cartilage using Stribeck surfaces. Journal of Biomechanics, 2008. 41(9): p. 1910-1918.

5. Schmidt, T.A., et al., Boundary lubrication of articular cartilage: Role of synovial fluid constituents. Arthritis & Rheumatism, 2007. 56(3): p. 882-891.

6. Schmidt, T.A. and R.L. Sah, Effect of synovial fluid on boundary lubrication of articular cartilage. Osteoarthritis and Cartilage, 2007. 15(1): p. 35-47.

7. Oates, K.M.N., et al., Rheopexy of synovial fluid and protein aggregation. Journal of The Royal Society Interface, 2006. 3(6): p. 167-174.

8. O'Neill, P.L. and G.W. Stachowiak. The inverse thixotropic behaviour of synovial fluid and its relation to the lubrication of synovial joints. RAPID SCIENCE, 1996. 9:p. 222-228.

9. Wheaton, M.T. and N. Jensen, The Ligament Injury-Osteoarthritis Connection: The Role of Prolotherapy in Ligament Repair and the Prevention of Osteoarthritis. Journal of Prolotherapy, 2011. 3(4): p. 790-812.

10. Green, G., Understanding NSAIDs: from aspirin to COX-2. Clin Cornerstone, 2001. 3(5): p. 50-60.

11. Helmick, C.G., et al., Estimates of the prevalence of arthritis and other rheumatic conditions in the United States: Part I. Arthritis & Rheumatism, 2008. 58(1): p. 15-25.

12. Buckwalter, J.A., Osteoarthritis and articular-cartilage use, disuse, and abuse-experimental studies. 1995. 43: p. 13-15.

13. Charnley, J., The lubrication of animal joints in relation to surgical reconstruction by arthroplasty. Annals of the Rheumatic Diseases, 1960. 19(1): p. 10-19.

14. Dowson, D., New joints for the Millennium: wear control in total replacement hip joints. Proceedings of the Institution of Mechanical Engineers Part H-Journal of Engineering in Medicine, 2001. 215(H4): p. 335-358.

15. McCutchen, C.W., The frictional properties of animal joints. Wear, 1962. 5: p. 1-17.

16. Radin, E.L., D.A. Swann, and P.A. Weisser, Separation of a hyaluronate-free lubricating fraction from synovial fluid. Nature, 1970. 228(5269): p. 377-378.

17. Jay, G.D., et al., Homology of lubricin and superficial zone protein (SZP): products of megakaryocyte stimulating factor (MSF) gene expression by human

synovial fibroblasts and articular chondrocytes localized to chromosome 1q25. Journal of Orthopaedic Research, 2001. 19(4): p. 677-687.

18. MacConaill, M.A., The function of inter-articular fibrocartilages, with special references to the knee and inferior radio-ulnar joints. J Anat 1932. 66: p. 210-227.

19. Dowson, D., Elastohydrodynamic and micro-elastohydrodynamic lubrication. Wear, 1995. 190(2): p. 125-138.

20. Higginso, G. and R. Norman, Model investigation of squeeze-film lubrication in animal joints. Physics in Medicine and Biology, 1974. 19(6): p. 785-792.

21. Hlavacek, M., Squeeze-film lubrication of the human ankle joint with synovial fluid filtrated by articular cartilage with the superficial zone worn out. Journal of Biomechanics, 2000. 33(11): p. 1415-1422.

22. Hlavacek, M., Squeeze-film lubrication of the human ankle joint subjected to the cyclic loading encountered in walking. Journal of Tribology-Transactions of the Asme, 2005. 127(1): p. 141-148.

23. McCutchen, C.W., Sponge-hydrostatic and weeping bearings. Nature, 1959. 184(4695): p. 1284-1285.

24. Walker, P.S., et al., Boosted lubrication in synovial joints by fluid entrapment and enrichment. Annals of the Rheumatic Diseases, 1968. 27(6): p. 512-518.

25. Mow, V.C., et al., Biphasic creep and stress-relaxation of articualr-cartilage in compression - theory and experiments. Journal of Biomechanical Engineering-Transactions of the Asme, 1980. 102(1): p. 73-84.

26. Mow, V.C., M.H. Holmes, and W.M. Lai, Fluid transport and mechanical-properties of articular-cartilage - a review. Journal of Biomechanics, 1984. 17(5): p. 377-394.

27. Ateshian, G.A., A theoretical formulation for boundary friction in articular cartilage. Journal of Biomechanical Engineering-Transactions of the Asme, 1997. 119(1): p. 81-86.

28. Ateshian, G.A. and H. Wang, Rolling resistance of articular cartilage due to interstitial fluid flow. Proceedings of the Institution of Mechanical Engineers Part H-Journal of Engineering in Medicine, 1997. 211(5): p. 419-424.

29. Ateshian, G.A., et al., Finite deformation biphasic material properties of bovine articular cartilage from confined compression experiments. Journal of Biomechanics, 1997. 30(11-12): p. 1157-1164.

30. Krishnan, R., M. Kopacz, and G.A. Ateshian, Experimental verification of the role of interstitial fluid pressurization in cartilage lubrication. Journal of Orthopaedic Research, 2004. 22(3): p. 565-570.

31. Ateshian, G.A., The role of interstitial fluid pressurization in articular cartilage lubrication. Journal of Biomechanics, 2009. 42(9): p. 1163-1176.

32. Dean, D., et al., Nanoscale conformation and compressibility of cartilage aggrecan using microcontact printing and atomic force microscopy. Macromolecules, 2005. 38(10): p. 4047-4049.

33. Pickard, J.E., et al., Investigation into the effects of proteins and lipids on the frictional properties of articular cartilage. Biomaterials, 1998. 19(19): p. 1807-1812.

34. Sarma, A.V., G.L. Powell, and M. LaBerge, Phospholipid composition of articular cartilage boundary lubricant. Journal of Orthopaedic Research, 2001. 19(4): p. 671-676.

35. Martin, R.B. and D.B. Bur, Skeletal Tissue Mechanics. 1998, Springer: New York.

36. Jin, Z.M. and D. Dowson, Elastohydrodynamic Lubrication in Biological Systems. Proceedings of the Institution of Mechanical Engineers, Part J: Journal of Engineering Tribology, 2005. 219(5): p. 367-380.

37. Dowson, D., et al., Design considerations for cushion form bearings in artificial hip joints. Proceedings Of The Institution Of Mechanical Engineers. Part H, Journal Of Engineering In Medicine, 1991. 205(2): p. 59-68.

38. Hlavacek, M., The role of synovial-fluid filtraion by cartilage in lubrication of synovial joints. 4. Squeeze-film lubrication - the central film thickness for normal and inflammatory synovial-fluid for axial symmetry under high loading condictions. Journal of Biomechanics, 1995. 28(10): p. 1199-1205.

39. Caligaris, M. and G.A. Ateshian, Effects of sustained interstitial fluid pressurization under migrating contact area, and boundary lubrication by synovial fluid, on cartilage friction. Osteoarthritis and Cartilage, 2008. 16(10): p. 1220-1227.

40. Hlavacek, M. and J. Novak, The role of synovial-fluid filtration by cartilage in lubrication of synovial joints. 3. Squeeze-film lubrication-axial symmetry under low loading coditions. Journal of Biomechanics, 1995. 28(10): p. 1193-1198.

41. Morrell, K.C., et al., Corroboration of in vivo cartilage pressures with implications for synovial joint tribology and osteoarthritis causation. Proceedings of the

National Academy of Sciences of the United States of America, 2005. 102(41): p. 14819-14824.

42. Bianco, A., Carbon nanotubes for the delivery of therapeutic molecules. Expert Opinion on Drug Delivery, 2004. 1(1): p. 57-65.

43. Kostarelos, K., A. Bianco, and M. Prato, Promises, facts and challenges for carbon nanotubes in imaging and therapeutics. Nat Nano, 2009. 4(10): p. 627-633.

44. Jan, E. and N.A. Kotov, Successful Differentiation of Mouse Neural Stem Cells on Layer-by-Layer Assembled Single-Walled Carbon Nanotube Composite. Nano Letters, 2007. 7(5): p. 1123-1128.

45. Lovat, V., et al., Carbon Nanotube Substrates Boost Neuronal Electrical Signaling. Nano Letters, 2005. 5(6): p. 1107-1110.

46. Khang, D., G.E. Park, and T.J. Webster, Enhanced chondrocyte densities on carbon nanotube composites: The combined role of nanosurface roughness and electrical stimulation. Journal of Biomedical Materials Research Part A, 2008. 86A(1): p. 253-260.

47. Xie, F., et al., Kinetic studies of a composite carbon nanotube-hydrogel for tissue engineering by rheological methods. Journal of Materials Science: Materials in Medicine, 2010. 21(4): p. 1163-1168.

48. Chen, Y., et al., Self-assembled rosette nanotube/hydrogel composites for cartilage tissue engineering. Tissue engineering. Part C, Methods, 2010. 16(6): p. 1233-1243.

49. Kim, J.Y., et al., Decreased macrophage density on carbon nanotube patterns on polycarbonate urethane. Journal of Biomedical Materials Research Part A, 2009. 88A(2): p. 419-426.

50. MacGinitie, L.A., Y.A. Gluzband, and A.J. Grodzinsky, Electric field stimulation can increase protein synthesis in articular cartilage explants. Journal Of Orthopaedic Research: Official Publication Of The Orthopaedic Research Society, 1994. 12(2): p. 151-160.

51. Shvedova, A., et al., Exposure to Carbon Nanotube Material: Assessment of Nanotube Cytotoxicity using Human Keratinocyte Cells. Journal of Toxicology and Environmental Health, Part A, 2003. 66(20): p. 1909-1926.

52. Manna, S.K., et al., Single-Walled Carbon Nanotube Induces Oxidative Stress and Activates Nuclear Transcription Factor-κB in Human Keratinocytes. Nano Letters, 2005. 5(9): p. 1676-1684.

53. Lam, C.-W., et al., Pulmonary Toxicity of Single-Wall Carbon Nanotubes in Mice 7 and 90 Days After Intratracheal Instillation. Toxicological Sciences, 2004. 77(1): p. 126-134.

54. Chen, X., et al., Interfacing Carbon Nanotubes with Living Cells. Journal of the American Chemical Society, 2006. 128(19): p. 6292-6293.

55. Dumortier, H., et al., Functionalized Carbon Nanotubes Are Non-Cytotoxic and Preserve the Functionality of Primary Immune Cells. Nano Letters, 2006. 6(7): p. 1522-1528.

56. Wick, P., et al., The degree and kind of agglomeration affect carbon nanotube cytotoxicity. Toxicology Letters, 2007. 168(2): p. 121-131.

57. Kostarelos, K., et al., Cellular uptake of functionalized carbon nanotubes is independent of functional group and cell type. Nat Nano, 2007. 2(2): p. 108-113.

58. Zhu, Y., et al., Dependence of the cytotoxicity of multi-walled carbon nanotubes on the culture medium. Nanotechnology, 2006. 17(18): p. 4668-4674.

59. Crouzier, T., et al., Modification of Single Walled Carbon Nanotube Surface Chemistry to Improve Aqueous Solubility and Enhance Cellular Interactions. Langmuir, 2008. 24(22): p. 13173-13181.

60. Wu, W., et al., Targeted Delivery of Amphotericin B to Cells by Using Functionalized Carbon Nanotubes. Angewandte Chemie International Edition, 2005. 44(39): p. 6358-6362.

61. Porter, A.E., et al., Uptake of Noncytotoxic Acid-Treated Single-Walled Carbon Nanotubes into the Cytoplasm of Human Macrophage Cells. ACS Nano, 2009. 3(6): p. 1485-1492.

62. Singh, P., et al., Polyamine functionalized carbon nanotubes: synthesis, characterization, cytotoxicity and siRNA binding. Journal of Materials Chemistry, 2011. 21(13): p. 4850-4860.

63. Liu, S., et al., Sharper and Faster "Nano Darts" Kill More Bacteria: A Study of Antibacterial Activity of Individually Dispersed Pristine Single-Walled Carbon Nanotube. ACS Nano, 2009. 3(12): p. 3891-3902.

64. Mutlu, G.k.M., et al., Biocompatible Nanoscale Dispersion of Single-Walled Carbon Nanotubes Minimizes in vivo Pulmonary Toxicity. Nano Letters, 2010. 10(5): p. 1664-1670.

65. Vácha, R., F.J. Martinez-Veracoechea, and D. Frenkel, Receptor-Mediated Endocytosis of Nanoparticles of Various Shapes. Nano Letters, 2011. 11(12): p. 5391-5395.

66. Park, S.H., et al., Cartilage interstitial fluid load support in unconfined compression. Journal of Biomechanics, 2003. 36(12): p. 1785-1796.

67. Bell, C.J., E. Ingham, and J. Fisher, Influence of hyaluronic acid on the time-dependent friction response of articular cartilage under different conditions. Proceedings of the Institution of Mechanical Engineers Part H-Journal of Engineering in Medicine, 2006. 220(H1): p. 23-31.

68. Merkher, Y., et al., A rational human joint friction test using a human cartilage-on-cartilage arrangement. Tribology Letters, 2006. 22(1): p. 29-36.

69. Northwood, E., J. Fisher, and R. Kowalski, Investigation of the friction and surface degradation of innovative chondroplasty materials against articular cartilage. Proceedings of the Institution of Mechanical Engineers Part H-Journal of Engineering in Medicine, 2007. 221(H3): p. 263-279.

70. Northwood, E. and J. Fisher, A multi-directional in vitro investigation into friction, damage and wear of innovative chondroplasty materials against articular cartilage. Clinical Biomechanics, 2007. 22(7): p. 834-842.

71. Katta, J., et al., Biotribology of articular cartilage-A review of the recent advances. Medical Engineering & Physics, 2008. 30(10): p. 1349-1363.

72. Katta, J., et al., Effect of nominal stress on the long term friction, deformation and wear of native and glycosaminoglycan deficient articular cartilage. Osteoarthritis and Cartilage, 2009. 17(5): p. 662-668.

73. Katta, J., et al., Chondroitin sulphate: an effective joint lubricant? Osteoarthritis and Cartilage, 2009. 17(8): p. 1001-1008.

74. Krishnan, R., E.N. Mariner, and G.A. Ateshian, Effect of dynamic loading on the frictional response of bovine articular cartilage. Journal of Biomechanics, 2005. 38(8): p. 1665-1673.

75. Naka, M.H., Y. Morita, and K. Ikeuchi, Influence of proteoglycan contents and of tissue hydration on the frictional characteristics of articular cartilage. Proceedings of the Institution of Mechanical Engineers Part H-Journal of Engineering in Medicine, 2005. 219(H3): p. 175-182.

76. Basalo, I.M., et al., Chondroitin sulfate reduces the friction coefficient of articular cartilage. Journal of Biomechanics, 2007. 40(8): p. 1847-1854.

77. Forster, H. and J. Fisher, The influence of loading time and lubricant on the friction of articular cartilage. Proceedings of the Institution of Mechanical Engineers Part H-Journal of Engineering in Medicine, 1996. 210(2): p. 109-119.

78. Forster, H. and J. Fisher, The influence of continuous sliding and subsequent surface wear on the friction of articular cartilage. Proceedings of the Institution of Mechanical Engineers Part H-Journal of Engineering in Medicine, 1999. 213(4): p. 329-345.

79. Tanaka, E., et al., The effect of experimental cartilage damage and impairment and restoration of synovial lubrication on friction in the temporomandibular joint. Journal of Orofacial Pain, 2005. 19(4): p. 331-336.

80. Jay, G.D., et al., Association Between Friction and Wear in Diarthrodial Joints Lacking Lubricin. Arthritis & Rheumatism, 2007. 56(11): p. 3662-3669.

81. Mori, S., M. Naito, and S. Moriyama, Highly viscous sodium hyaluronate and joint lubrication. International Orthopaedics, 2002. 26(2): p. 116-121.

82. Forsey, R.W., et al., The effect of hyaluronic acid and phospholipid based lubricants on friction within a human cartilage damage model. Biomaterials, 2006. 27(26): p. 4581-4590.

83. Bian, L.M., et al., Influence of chondroitin sulfate on the biochemical, mechanical and frictional properties of cartilage explants in long-term culture. Journal of Biomechanics, 2009. 42(3): p. 286-290.

84. Neu, C.P., et al., Mechanotransduction of bovine articular cartilage superficial zone protein by transforming growth factor β signaling. Arthritis & Rheumatism, 2007. 56(11): p. 3706-3714.

85. DuRaine, G., et al., Regulation of the friction coefficient of articular cartilage by TGF-β1 and IL-1β. Journal of Orthopaedic Research, 2009. 27(2): p. 249-256.

86. Chan, S.M.T., et al., Atomic force microscope investigation of the boundary-lubricant layer in articular cartilage. Osteoarthritis and Cartilage, 2010. 18(7): p. 956-963.

87. Hersey, M.D., Laws of lubrication. Journal of the Washington Academy of Sciences, 1914. 4: p. 542-552.

88. Benz, M., et al., Static forces, structure and flow properties of complex fluids in highly confined geometries. Annals of Biomedical Engineering, 2005. 33(1): p. 39-51.

89. Hlavacek, M., The role of synovial-fluid filtration by cartilage in lubrication of synovial joints. 1. Mixture model of synovial-fluid. Journal of Biomechanics, 1993. 26(10): p. 1145-1150.

90. Hlavacek, M., The thixotropic effect of the synovial fluid in squeeze-film lubrication of the human hip joint. Biorheology, 2001. 38(4): p. 319-334.

91. Hlavacek, M., The role of synovial-fluid filtration by cartilage in lubrication of synovial joints. 2. Squeeze-film lubrication-homemogeneous filtraion. Journal of Biomechanics, 1993. 26(10): p. 1151-1160.

92. Paul, J.P.M., D. A., Forces transmitted at the hip and knee joint of normal and disabled persons during a range of activities. Acta orthopaedica Belgica, 1975. 1(1): p. 78-88.

93. Brizmer, V., Y. Kligerman, and I. Etsion, Elastic-plastic spherical contact under combined normal and tangential loading in full stick. Tribology Letters, 2007. 25(1): p. 61-70.

94. Malamut, S., Y. Kligerman, and I. Etsion, The Effect of Dwell Time on the Static Friction in Creeping Elastic-Plastic Polymer Spherical Contact. Tribology Letters, 2009. 35(3): p. 159-170.

95. Graindorge, S.L. and G.W. Stachowiak, Changes occurring in the surface morphology of articular cartilage during wear. Wear, 2000. 241(2): p. 143-150.

96. Kääb, M.J., et al., Monopolar Radiofrequency Treatment of Partial-Thickness Cartilage Defects in the Sheep Knee Joint Leads to Extended Cartilage Injury. American Journal of Sports Medicine, 2005. 33(10): p. 1472-1478.

97. Stachowiak, G.P., G.W. Stachowiak, and P. Podsiadlo, Automated classification of articular cartilage surfaces based on surface texture. Proceedings of the Institution of Mechanical Engineers -- Part H -- Journal of Engineering in Medicine, 2006. 220(8): p. 831-843.

98. Shields, K.J., J.R. Owen, and J.S. Wayne, Biomechanical and Biotribological Correlation of Induced Wear on Bovine Femoral Condyles. Journal of Heat Transfer, 2009. 131(6): p. 061005-9.

99. Torzilli, P.A., Water-content and equilibrium water partition in immature cartilage. Journal of Orthopaedic Research, 1988. 6(5): p. 766-769.

100. Williams III, P.F., G.L. Powell, and M. LaBerge, Sliding friction analysis of phosphatidylcholine as a boundary lubricant for articular cartilage. Proc Inst Mech Eng H. , 1993. 207(1): p. 59-66.

101. Lewis, P.R. and C.W. McCutchen, Experimental evidence for weeping lubrication in mammalian joints. Nature, 1959. 184(4695): p. 1285-1285.

102. Shi, L., V. Sikavitsas, and A. Striolo, Experimental Friction Coefficients for Bovine Cartilage Measured with a Pin-on-Disk Tribometer: Testing Configuration and Lubricant Effects. Annals of Biomedical Engineering, 2011. 39: p. 132-146.

103. Swann, D.A., H.S. Slayter, and F.H. Silver, The molecular structure of lubricating glycoprotein-I, the boundary lubricant for articular cartilage. Journal of Biological Chemistry, 1981. 256(11): p. 5921-5925.

104. Jay, G., D. Harris, and C.-J. Cha, Boundary lubrication by lubricin is mediated by O-linked β(1-3)Gal-GalNAc oligosaccharides. Glycoconjugate Journal, 2001. 18(10): p. 807-815.

105. Tanner, R.I., An Alternative Mechanism for the Lubrication of Synovial Joints. Physics in Medicine and Biology, 1966. 11(1): p. 109-119.

106. Kawano, T., et al., Mechanical effects of the intraarticular administration of high molecular weight hyaluronic acid plus phospholipid on synovial joint lubrication and

prevention of articular cartilage degeneration in experimental osteoarthritis. Arthritis And Rheumatism, 2003. 48(7): p. 1923-1929.

107. Neu, C.P., et al., Friction coefficient and superficial zone protein are increased in patients with advanced osteoarthritis. Arthritis & Rheumatism, 2010. 62(9): p. 2680-2687.

108. Nugent-Derfus, G.E., et al., PRG4 exchange between the articular cartilage surface and synovial fluid. Journal of Orthopaedic Research, 2007. 25(10): p. 1269-1276.

109. Rhee, D.K., et al., The secreted glycoprotein lubricin protects cartilage surfaces and inhibits synovial cell overgrowth. The Journal of Clinical Investigation, 2005. 115(3): p. 622-631.

110. Rodahl, M., et al., Quartz crystal microbalance setup for frequency and Q factor measurements in gaseous and liquid environments. Review of Scientific Instruments, 1995. 66(7): p. 3924-3930.

111. Croll, T.I., et al., A Blank Slate? Layer-by-Layer Deposition of Hyaluronic Acid and Chitosan onto Various Surfaces. Biomacromolecules, 2006. 7(5): p. 1610-1622.

112. Schneider, A., et al., Layer-by-Layer Films from Hyaluronan and Amine-Modified Hyaluronan. Langmuir, 2007. 23(5): p. 2655-2662.

113. Shi, L., et al., Adsorption Isotherms of Aqueous C12E6 and Cetyltrimethylammonium Bromide Surfactants on Solid Surfaces in the Presence of Low Molecular Weight Coadsorbents. Langmuir, 2009. 25(10): p. 5536-5544.

114. Kumar, P., et al., Role of uppermost superficial surface layer of articular cartilage in the lubrication mechanism of joints. Journal of Anatomy, 2001. 199(3): p. 241-250.

115. Ball, S.T., et al., The Effects of Storage on Fresh Human Osteochondral Allografts. Clinical Orthopaedics and Related Research, 2004. 418: p. 246-252.

116. McCarty, W., et al., An Arthroscopic Device to Assess Articular Cartilage Defects and Treatment with a Hydrogel. Annals of Biomedical Engineering, 2011. 39(4): p. 1306-1312.

117. Szarko, M., K. Muldrew, and J. Bertram, Freeze-thaw treatment effects on the dynamic mechanical properties of articular cartilage. BMC Musculoskeletal Disorders, 2010. 11(1): p. 329-345.

118. Helga, L. and R. Wiltrud, Osteoarthritis: Cellular and molecular changes in degenerating cartilage. Progress in Histochemistry and Cytochemistry, 2006. 40: p. 135-163.

119. Verberne, G., et al., Liposomes as potential biolubricant additives for wear reduction in human synovial joints. Wear, 2010. 268(7-8): p. 1037-1042.

120. Sivan, S., et al., Liposomes Act as Effective Biolubricants for Friction Reduction in Human Synovial Joints. Langmuir, 2009. 26(2): p. 1107-1116.

121. Benz, M., N. Chen, and J. Israelachvili, Lubrication and wear properties of grafted polyelectrolytes, hyaluronan and hylan, measured in the surface forces apparatus. Journal of Biomedical Materials Research Part A, 2004. 71A(1): p. 6-15.

122. Begum, R. and H. Matsuura, Conformational properties of short poly(oxyethylene) chains in water studied by IR spectroscopy. Journal of the Chemical Society, Faraday Transactions, 1997. 93(21): p. 3839-3848.

123. Watterson, J.R. and J.M. Esdaile, Viscosupplementation: Therapeutic Mechanisms and Clinical Potential in Osteoarthritis of the Knee. J Am Acad Orthop Surg, 2000. 8(5): p. 277-284.

124. Mazzucco, D., R. Scott, and M. Spector, Composition of joint fluid in patients undergoing total knee replacement and revision arthroplasty: correlation with flow properties. Biomaterials, 2004. 25(18): p. 4433-4445.

125. Englert, C., et al., Inhibition of integrative cartilage repair by proteoglycan 4 in synovial fluid. Arthritis & Rheumatism, 2005. 52(4): p. 1091-1099.

126. Singh, R., et al., Binding and Condensation of Plasmid DNA onto Functionalized Carbon Nanotubes: Toward the Construction of Nanotube-Based Gene Delivery Vectors. Journal of the American Chemical Society, 2005. 127(12): p. 4388-4396.

127. Podesta, J.E., et al., Antitumor Activity and Prolonged Survival by Carbon-Nanotube-Mediated Therapeutic siRNA Silencing in a Human Lung Xenograft Model. Small, 2009. 5(10): p. 1176-1185.

128. Kam, N.W.S., Z. Liu, and H. Dai, Carbon Nanotubes as Intracellular Transporters for Proteins and DNA: An Investigation of the Uptake Mechanism and Pathway. Angewandte Chemie International Edition, 2006. 45(4): p. 577-581.

129. Samori, C., et al., Enhanced anticancer activity of multi-walled carbon nanotube-methotrexate conjugates using cleavable linkers. Chemical Communications, 2010. 46(9): p. 1494-1496.

130. Al-Jamal, K.T., et al., Cellular uptake mechanisms of functionalised multi-walled carbon nanotubes by 3D electron tomography imaging. Nanoscale, 2011. 3(6): p. 2627-2635.

131. Kang, S., et al., Antibacterial Effects of Carbon Nanotubes: Size Does Matter! Langmuir, 2008. 24(13): p. 6409-6413.

132. Vecitis, C.D., et al., Electronic-Structure-Dependent Bacterial Cytotoxicity of Single-Walled Carbon Nanotubes. ACS Nano, 2010. 4(9): p. 5471-5479.

133. Wallace, E.J. and M.S.P. Sansom, Blocking of Carbon Nanotube Based Nanoinjectors by Lipids: A Simulation Study. Nano Letters, 2008. 8(9): p. 2751-2756.

134. Höfinger, S., et al., A computational analysis of the insertion of carbon nanotubes into cellular membranes. Biomaterials, 2011. 32(29): p. 7079-7085.

135. Rasch, M.R., et al., Hydrophobic Gold Nanoparticle Self-Assembly with Phosphatidylcholine Lipid: Membrane-Loaded and Janus Vesicles. Nano Letters, 2010. 10(9): p. 3733-3739.

136. Karchemski, F., et al., Carbon nanotubes-liposomes conjugate as a platform for drug delivery into cells. Journal of Controlled Release, 2012. 160(2): p. 339-345.

137. Ghosh, S., S.M. Bachilo, and R.B. Weisman, Advanced sorting of single-walled carbon nanotubes by nonlinear density-gradient ultracentrifugation. Nat Nano, 2010. 5(6): p. 443-450.

138. Forlow, S.B., R.P. McEver, and M.U. Nollert, Leukocyte-leukocyte interactions mediated by platelet microparticles under flow. Blood, 2000. 95(4): p. 1317-1323.

139. Yamaguchi, T., et al., Effects of frequency and power of ultrasound on the size reduction of liposome. Chemistry and Physics of Lipids, 2009. 160(1): p. 58-62.

140. Ilker, M.F., et al., Tuning the Hemolytic and Antibacterial Activities of Amphiphilic Polynorbornene Derivatives. Journal of the American Chemical Society, 2004. 126(48): p. 15870-15875.

141. Takeshita, K., S. Okazaki, and H. Kansui, Effect of cholesterol on distribution of stable, hydrophobic perchlorotriphenylmethyl triethylester radical incorporated in lecithin liposomal membranes. Chemical & Pharmaceutical Bulletin, 2011. 59(5): p. 624-628.

142. Oldfield, E. and D. Chapman, Effects of cholesterol and cholesterol derivatives on hydrocarbon chain mobility in lipids. Biochemical and Biophysical Research Communications, 1971. 43(3): p. 610-616.

143. Tan, Y. and D.E. Resasco, Dispersion of Single-Walled Carbon Nanotubes of Narrow Diameter Distribution. The Journal of Physical Chemistry B, 2005. 109(30): p. 14454-14460.

144. Maskrey, B.H., et al., Activated Platelets and Monocytes Generate Four Hydroxyphosphatidylethanolamines via Lipoxygenase. Journal of Biological Chemistry, 2007. 282(28): p. 20151-20163.

145. Pedersen, K.H., et al., Replacement of the foam index test with surface tension measurements. Cement and Concrete Research, 2007. 37: p. 996-1004.

146. Saiyad, A.H., S.G.T. Bhat, and A.K. Rakshit, Physicochemical properties of mixed surfacant systems: sodium dodecyl benzene sulfonate with triton X 100. Colloid & Polymer Science, 1998. 276(10): p. 913-919.

147. Matarredona, O., et al., Dispersion of Single-Walled Carbon Nanotubes in Aqueous Solutions of the Anionic Surfactant NaDDBS. J. Phys. Chem. B, 2003. 107(48): p. 13357-13367.

148. Runtang, W., et al., SWCNT PEG-eggs: Single-walled carbon nanotubes in biocompatible shell-crosslinked micelles. Carbon. 45: p. 2388-2393.

149. Ying, T., et al., Growth of single-walled carbon nanotubes with controlled diameters and lengths by an aerosol method. Carbon. 49: p. 4636-4643.

150. Suttipong, M., et al., Role of Surfactant Molecular Structure on Self-Assembly: Aqueous SDBS on Carbon Nanotubes. The Journal of Physical Chemistry C, 2011. 115(35): p. 17286-17296.

151. Richard, C., et al., Supramolecular Self-Assembly of Lipid Derivatives on Carbon Nanotubes. Science, 2003. 300(5620): p. 775-778.

152. Wu, Y., et al., Coating Single-Walled Carbon Nanotubes with Phospholipids. The Journal of Physical Chemistry B, 2006. 110(6): p. 2475-2478.

153. Uthman, I., J.-P. Raynauld, and B. Haraoui, Intra-articular therapy in osteoarthritis. Postgrad Med J, 2003. 79(934): p. 449-453.

154. Troeberg, L., et al., Calcium pentosan polysulfate is a multifaceted exosite inhibitor of aggrecanases. FASEB J., 2008. 22(10): p. 3515-3524.

155. Takizawa, M., et al., Calcium pentosan polysulfate directly inhibits enzymatic activity of ADAMTS4 (aggrecanase-1) in osteoarthritic chondrocytes. FEBS Letters, 2008. 582(19): p. 2945-2949.

156. Munteanu, S.E., M.Z. Ilic, and C.J. Handley, Calcium pentosan polysulfate inhibits the catabolism of aggrecan in articular cartilage explant cultures. Arthritis & Rheumatism, 2000. 43(10): p. 2211-2218.

157. Momot, K., Diffusion tensor of water in model articular cartilage. European Biophysics Journal, 2011. 40(1): p. 81-91.

158. Utesch, T., G. Daminelli, and M.A. Mroginski, Molecular Dynamics Simulations of the Adsorption of Bone Morphogenetic Protein-2 on Surfaces with Medical Relevance. Langmuir, 2011. 27(21): p. 13144-13153.

159. Chung, S., M.P. Gamcsik, and M.W. King, Novel scaffold design with multi-grooved PLA fibers. Biomedical Materials, 2011. 6: p. 045001-12.

160. Brittberg, M., et al., Treatment of Deep Cartilage Defects in the Knee with Autologous Chondrocyte Transplantation. New England Journal of Medicine, 1994. 331(14): p. 889-895.

161. Liu, H., et al., Large-scale single-chirality separation of single-wall carbon nanotubes by simple gel chromatography. Nat Commun, 2011. 2: p. 309-8.

162. Orsi, M. and J.W. Essex, Permeability of drugs and hormones through a lipid bilayer: insights from dual-resolution molecular dynamics. Soft Matter, 2010. 6(16): p. 3797-3808.

163. Orsi, M., W.E. Sanderson, and J.W. Essex, Permeability of Small Molecules through a Lipid Bilayer: A Multiscale Simulation Study. The Journal of Physical Chemistry B, 2009. 113(35): p. 12019-12029.

164. Fiedler, S.L. and A. Violi, Simulation of Nanoparticle Permeation through a Lipid Membrane. Biophysical Journal, 2010. 99(1): p. 144-152.

165. Paria, S. and K.C. Khilar, A review on experimental studies of surfactant adsorption at the hydrophilic solid-water interface. Advances in Colloid and Interface Science, 2004. 110(3): p. 75-95.

166. Tiberg, F., B. Joesson, and B. Lindman, Ellipsometry Studies of the Self-Assembly of Nonionic Surfactants at the Silica-Water Interface: Kinetic Aspects. Langmuir, 1994. 10(10): p. 3714-3722.

167. Tiberg, F., B. Lindman, and M. Landgren, Interfacial behaviour of non-ionic surfactants at the silica-water interface revealed by ellipsometry. Thin Solid Films, 1993. 234(1–2): p. 478-481.

168. Denoyel, R., Microcalorimetry and ellipsometry in surfactant adsorption studies. Colloids and Surfaces A: Physicochemical and Engineering Aspects, 2002. 205(1–2): p. 61-71.

169. Wall, J.F. and C.F. Zukoski, Alcohol-Induced Structural Transformations of Surfactant Aggregates. Langmuir, 1999. 15(22): p. 7432-7437.

170. Dong, J., G. Mao, and R.M. Hill, Nanoscale Aggregate Structures of Trisiloxane Surfactants at the Solidâˆ’Liquid Interface. Langmuir, 2004. 20(7): p. 2695-2700.

171. Dong, J. and G. Mao, Direct Study of C12E5 Aggregation on Mica by Atomic Force Microscopy Imaging and Force Measurements. Langmuir, 2000. 16(16): p. 6641-6647.

172. Svitova, T., R.M. Hill, and C.J. Radke, Adsorption layer structures and spreading behavior of aqueous non-ionic surfactants on graphite. Colloids and Surfaces A: Physicochemical and Engineering Aspects, 2001. 183–185(0): p. 607-620.

173. Connell, S.D., et al., In Situ Atomic Force Microscopy Imaging of Block Copolymer Micelles Adsorbed on a Solid Substrate. Langmuir, 2003. 19(24): p. 10449-10453.

174. Schniepp, H.C., et al., Surfactant Aggregates at Rough Solid−Liquid Interfaces. The Journal of Physical Chemistry B, 2007. 111(30): p. 8708-8712.

175. Caruso, F., et al., Quartz Crystal Microbalance and Surface Plasmon Resonance Study of Surfactant Adsorption onto Gold and Chromium Oxide Surfaces. Langmuir, 1995. 11(5): p. 1546-1552.

176. Penfold, J., et al., The Adsorption of Mixed Surfactants at the Hydrophilic Silica Surface from Aqueous Solution: Studied by Specular Neutron Reflection. International Journal of Thermophysics, 1999. 20: p. 19-34.

177. Penfold, J., I. Tucker, and R.K. Thomas, Adsorption of Nonionic Surfactant Mixtures at the Hydrophilic Solid−Solution Interface. Langmuir, 2005. 21(14): p. 6330-6336.

178. Penfold, J., I. Tucker, and R.K. Thomas, Polyelectrolyte Modified Solid Surfaces: the Consequences for Ionic and Mixed Ionic/Nonionic Surfactant Adsorption. Langmuir, 2005. 21(25): p. 11757-11764.

179. Velegol, S.B., et al., Counterion Effects on Hexadecyltrimethylammonium Surfactant Adsorption and Self-Assembly on Silica. Langmuir, 2000. 16(6): p. 2548-2556.

180. Manne, S., et al., Direct Visualization of Surfactant Hemimicelles by Force Microscopy of the Electrical Double Layer. Langmuir, 1994. 10(12): p. 4409-4413.

181. Ducker, W.A. and E.J. Wanless, Adsorption of Hexadecyltrimethylammonium Bromide to Mica: Nanometer-Scale Study of Binding-Site Competition Effects. Langmuir, 1998. 15(1): p. 160-168.

182. Schniepp, H.C., et al., Orientational Order of Molecular Assemblies on Rough Surfaces. The Journal of Physical Chemistry C, 2008. 112(38): p. 14902-14906.

183. Patrick, H.N., et al., Self-Assembly Structures of Nonionic Surfactants at Graphite/Solution Interfaces. Langmuir, 1997. 13(16): p. 4349-4356.

184. Grant, L.M., F. Tiberg, and W.A. Ducker, Nanometer-Scale Organization of Ethylene Oxide Surfactants on Graphite, Hydrophilic Silica, and Hydrophobic Silica. The Journal of Physical Chemistry B, 1998. 102(22): p. 4288-4294.

185. Stålgren, J.J.R., J. Eriksson, and K. Boschkova, A Comparative Study of Surfactant Adsorption on Model Surfaces Using the Quartz Crystal Microbalance and the Ellipsometer. Journal of Colloid and Interface Science, 2002. 253(1): p. 190-195.

186. Merta, J., T. Tammelin, and P. Stenius, Adsorption of complexes formed by cationic starch and anionic surfactants on quartz studied by QCM-D. Colloids and Surfaces A: Physicochemical and Engineering Aspects, 2004. 250(1–3): p. 103-114.

187. Naderi, A. and P.M. Claesson, Adsorption Properties of Polyelectrolyte−Surfactant Complexes on Hydrophobic Surfaces Studied by QCM-D. Langmuir, 2006. 22(18): p. 7639-7645.

188. Macakova, L., E. Blomberg, and P.M. Claesson, Effect of Adsorbed Layer Surface Roughness on the QCM-D Response: Focus on Trapped Water. Langmuir, 2007. 23(24): p. 12436-12444.

189. Gutig, C., B.P. Grady, and A. Striolo, Experimental Studies on the Adsorption of Two Surfactants on Solid−Aqueous Interfaces: Adsorption Isotherms and Kinetics. Langmuir, 2008. 24(9): p. 4806-4816.

190. Zana, R., et al., Effect of alcohol on the properties of micellar systems: I. Critical micellization concentration, micelle molecular weight and ionization degree, and solubility of alcohols in micellar solutions. Journal of Colloid and Interface Science, 1981. 80(1): p. 208-223.

191. Abdul, A.S., T.L. Gibson, and D.N. Rai, Selection of Surfactants for the Removal of Petroleum Products from Shallow Sandy Aquifers. Ground Water, 1990. 28(6): p. 920-926.

192. Rouse, J.D., D.A. Sabatini, and J.H. Harwell, Minimizing surfactant losses using twin-head anionic surfactants in subsurface remediation. Environmental Science & Technology, 1993. 27(10): p. 2072-2078.

193. Rouse, J.D., et al., Micellar Solubilization of Unsaturated Hydrocarbon Concentrations As Evaluated by Semiequilibrium Dialysis. Environmental Science & Technology, 1995. 29(10): p. 2484-2489.

194. Wu, J., J.H. Harwell, and E.A. O'Rear, Two-dimensional reaction solvents: surfactant bilayers in the formation of ultrathin films. Langmuir, 1987. 3(4): p. 531-537.

195. Boufi, S. and A. Gandini, Formation of polymeric films on cellulosic surfaces by admicellar polymerization. Cellulose, 2001. 8(4): p. 303-312.

196. Le, D.V., M.M. Kendrick, and E.A. O'Rear, Admicellar Polymerization and Characterization of Thin Poly(2,2,2-trifluoroethyl acrylate) Film on Aluminum Alloys for In-Crevice Corrosion Control. Langmuir, 2004. 20(18): p. 7802-7810.

197. Yuan, W.-L., et al., Nanometer-Thick Poly(pyrrole) Films Formed by Admicellar Polymerization under Conditions of Depleting Adsolubilization. Langmuir, 2002. 18(8): p. 3343-3351.

198. Castano, H., et al., Polypyrrole Thin Films Formed by Admicellar Polymerization Support the Osteogenic Differentiation of Mesenchymal Stem Cells. Macromolecular Bioscience, 2004. 4(8): p. 785-794.

199. Marquez, M., et al., Synthesis of Nanometer-Scale Polymeric Structures on Surfaces from Template Assisted Admicellar Polymerization: A Comparative Study with Protein Adsorption. Langmuir, 2006. 22(19): p. 8010-8016.

200. Lee, C., et al., Two-site adsolubilization model of incorporation of alcohols into adsorbed surfactant aggregates. Langmuir, 1990. 6(12): p. 1758-1762.

201. Høiland, H., et al., Solubilization of 1-hexanol in hexadecyltrimethylammonium bromide, sodium dodecyl sulfate, and sodium decanoate. Journal of Colloid and Interface Science, 1985. 107(2): p. 576-578.

202. Mukerjee, P. and J.R. Cardinal, Benzene derivatives and naphthalene solubilized in micelles. Polarity of microenvironments, location and distribution in micelles, and

correlation with surface activity in hydrocarbon-water systems. The Journal of Physical Chemistry, 1978. 82(14): p. 1620-1627.

203. Nayyar, S.P., D.A. Sabatini, and J.H. Harwell, Surfactant Adsolubilization and Modified Admicellar Sorption of Nonpolar, Polar, and Ionizable Organic Contaminants. Environmental Science & Technology, 1994. 28(11): p. 1874-1881.

204. Esumi, K., K. Sakai, and K. Torigoe, Reexamination of 2-Naphthol Adsolubilization on Alumina with Sodium Dodecyl Sulfate Adsorption. Journal of Colloid and Interface Science, 2000. 224(1): p. 198-201.

205. Esumi, K., N. Maedomari, and K. Torigoe, Mixed Surfactant Adsolubilization of 2-Naphthol on Alumina. Langmuir, 2000. 16(24): p. 9217-9220.

206. Dickson, J. and J. O'Haver, Adsolubilization of Naphthalene and α-Naphthol in CnTAB Admicelles. Langmuir, 2002. 18(24): p. 9171-9176.

207. Okamoto, N., T. Yoshimura, and K. Esumi, Effect of pH on adsolubilization of single and binary organic solutes into a cationic hydrocarbon surfactant adsorbed layer on silica. Journal of Colloid and Interface Science, 2004. 275(2): p. 612-617.

208. Saphanuchart, W., C. Saiwan, and J.H. O'Haver, Temperature effects on adsolubilization of aromatic solutes partitioning to different regions in cationic admicelles. Colloids and Surfaces A: Physicochemical and Engineering Aspects, 2008. 317(1–3): p. 303-308.

209. Sammalkorpi, M., A.Z. Panagiotopoulos, and M. Haataja, Structure and Dynamics of Surfactant and Hydrocarbon Aggregates on Graphite: A Molecular Dynamics Simulation Study. The Journal of Physical Chemistry B, 2008. 112(10): p. 2915-2921.

210. Shah, K., P. Chiu, and S.B. Sinnott, Comparison of morphology and mechanical properties of surfactant aggregates at water–silica and water–graphite interfaces from molecular dynamics simulations. Journal of Colloid and Interface Science, 2006. 296(1): p. 342-349.

211. Tummala, N.R. and A. Striolo, Role of Counterion Condensation in the Self-Assembly of SDS Surfactants at the Water-Graphite Interface. J. Phys. Chem. B, 2008. 112(7): p. 1987-2000.

212. Kovacs, L. and G.G. Warr, Changes in the Adsorbed Layer Structure of Cationic Surfactants on Mica Induced by Adsolubilized Aromatic Molecules. Langmuir, 2002. 18(12): p. 4790-4794.

213. Saphanuchart, W., C. Saiwan, and J.H. O'Haver, Effect of adsolubilized solutes on 2-D structure of cationic admicelles. Colloids and Surfaces A: Physicochemical and Engineering Aspects, 2007. 307(1–3): p. 71-76.

214. Berr, S.S., Solvent isotope effects on alkytrimethylammonium bromide micelles as a function of alkyl chain length. The Journal of Physical Chemistry, 1987. 91(18): p. 4760-4765.

215. Voinova, M.V., et al., Viscoelastic Acoustic Response of Layered Polymer Films at Fluid-Solid Interfaces: Continuum Mechanics Approach. Physica Scripta, 1999. 59(5): p. 391-396.

216. Vogt, B.D., et al., Moisture Absorption and Absorption Kinetics in Polyelectrolyte Films: Influence of Film Thickness. Langmuir, 2004. 20(4): p. 1453-1458.

217. Vogt, B.D., et al., Effect of Film Thickness on the Validity of the Sauerbrey Equation for Hydrated Polyelectrolyte Films. The Journal of Physical Chemistry B, 2004. 108(34): p. 12685-12690.

218. Lubarsky, G.V., M.R. Davidson, and R.H. Bradley, Hydration–dehydration of adsorbed protein films studied by AFM and QCM-D. Biosensors and Bioelectronics, 2007. 22(7): p. 1275-1281.

219. Rosen, M., Surfactants and Interfacial Phenomenon. 3 ed. 2004, New York: Wiley Interscience.

220. Larsson, C., M. Rodahl, and F. Höök, Characterization of DNA Immobilization and Subsequent Hybridization on a 2D Arrangement of Streptavidin on a Biotin-Modified Lipid Bilayer Supported on SiO2. Analytical Chemistry, 2003. 75(19): p. 5080-5087.

221. Keiji Kanazawa, K. and J.G. Gordon Ii, The oscillation frequency of a quartz resonator in contact with liquid. Analytica Chimica Acta, 1985. 175(0): p. 99-105.

222. Kandori, K., R.J. McGreevy, and R.S. Schechter, Solubilization of phenol in polyethoxylated nonionic micelles. Journal of Colloid and Interface Science, 1989. 132(2): p. 395-402.

223. Larson, R.G., Structure and Rheology of Complex Fluid, Chapter 12. 1999, New York: Oxford University Press.

224. Hoffmann, H. and H. Rehage, Surfactant Solutions. 1987, New York: New Methods of Investigation.

225. Tummala, N.R. and A. Striolo, SDS Surfactants on Carbon Nanotubes: Aggregate Morphology. ACS Nano, 2009. 3(3): p. 595-602.

226. Jodar-Reyes, A.B., J. Lyklema, and F.A.M. Leermakers, Comparison between Inhomogeneous Adsorption of Charged Surfactants on Air-Water and on Solid-Water Interfaces by Self-Consistent Field Theory. Langmuir, 2008. 24(13): p. 6496-6503.

227. Tummala, N.R. and A. Striolo, Curvature effects on the adsorption of aqueous sodium-dodecyl-sulfate surfactants on carbonaceous substrates: Structural features and counterion dynamics. Physical Review E (Statistical, Nonlinear, and Soft Matter Physics), 2009. 80(2): p. 021408-10.

228. Nair, N., et al., Dynamics of Surfactant-Suspended Single-Walled Carbon Nanotubes in a Centrifugal Field. Langmuir, 2008. 24(5): p. 1790-1795.

229. O'Connell, M.J., et al., Band Gap Flourescence from Individual Single-Walled Carbon Nanotubes. Science, 2002. 297(5581): p. 593-596.

230. Yurekli, K., C.A. Mitchell, and R. Krishnamoorti, Small-Angle Neutron Scattering from Surfactant-Assisted Aqueous Dispersions of Carbon Nanotubes. J. Am. Chem. Soc., 2004. 126(32): p. 9902-9903.

231. Laughin, R.G., The Aqueous Phase Behavior of Surfactants. 1994, New York: Academic Press.

232. Stalgren, J.J.R., J. Eriksson, and K. Boschkova, A Comparative Study of Surfactant Adsorption on Model Surfaces Using the Quartz Crystal Microbalance and the Ellipsometer. Journal of Colloid and Interface Science, 2002. 253: p. 190-195.

233. Kjellin, U.R.M., P.M. Claesson, and P. Linse, Surface Properties of Tetra(ethylene oxide) Dodecyl Amide Compared with Poly(ethylene oxide) Surfactants. 1. Effect of the Headgroup on Adsorption. Langmuir, 2002. 18(18): p. 6745-6753.

234. Lu, J.R., et al., The Structure of Monododecyl Pentaethylene Glycol Monolayers with and without Added Dodecane at the Air/Solution Interface: A Neutron Reflection Study. The Journal of Physical Chemistry B, 1998. 102(30): p. 5785-5793.

235. Lu, J.R., et al., Neutron Reflection from a Layer of Monododecyl Octaethylene Glycol Adsorbed at the Air-Liquid Interface: The Structure of the Layer and the Effects of Temperature, in The Journal of Physical Chemistry. 1994, American Chemical Society. p. 6559-6567.

236. Lu, J.R., et al., Neutron reflection from a layer of monododecyl hexaethylene glycol adsorbed at the air-liquid interface: the configuration of the ethylene glycol chain. The Journal of Physical Chemistry, 1993. 97(30): p. 8012-8020.

237. Lu, J.R., et al., Structure of Monolayers of Monododecyl Dodecaethylene Glycol at the Airâˆ’Water Interface Studied by Neutron Reflection. The Journal of Physical Chemistry B, 1997. 101(49): p. 10332-10339.

238. Penfold, J., et al., The Structure of the Mixed Nonionic Surfactant Monolayer of Monododecyl Triethylene Glycol and Monododecyl Octaethylene Glycol at the Air-Water Interface. Journal of Colloid and Interface Science, 1998. 201: p. 223-232.

239. Lu, J.R., et al., Adsorption of Dodecyl Sulfate Surfactants with Monovalent Metal Counterions at the Air-Water Interface Studied by Neutron Reflection and Surface Tension. Journal of Colloid and Interface Science, 1993. 158(2): p. 303-316.

240. Lu, J.R., et al., The Composition and Structure of Sodium Dodecyl Sulfate-Dodecanol Mixtures Adsorbed at the Air-Water Interface: A Neutron Reflection Study. Journal of Colloid and Interface Science, 1995. 174(2): p. 441-455.

241. Lu, J.R., et al., Some aspects of the structure of amphiphilic monolayers at the air-liquid interface determined by neutron reflection. Journal of Physics: Condensed Matter, 1994(23A): p. A403-A408.

242. Penfold, J., et al., The structure of mixed surfactant monolayers at the air-liquid interface, as studied by specular neutron reflection. Journal of Physics: Condensed Matter, 1990(S): p. SA411-SA416.

243. Purcell, I.P., et al., Adsorption of SDS and PVP at the air/water interface, in Colloids and Surfaces A: Physicochemical and Engineering Aspects. 1995. p. 125-130.

244. Hiemenz, P.C. and R. Rajagopalan, Principles of Colloid and Surface Chemistry. 3 ed. 1997, New Yrok: Marcel Decker Inc.

245. Dominguez, H. and M.L. Berkowitz, Computer Simulations of Sodium Dodecyl Sulfate at Liquid/Liquid and Liquid/Vapor Interfaces. The Journal of Physical Chemistry B, 2000. 104(22): p. 5302-5308.

246. Luo, M. and L.L. Dai, Molecular dynamics simulations of surfactant and nanoparticle self-assembly at liquid-liquid interfaces. Journal of Physics: Condensed Matter, 2007(37): p. 375109-14.

247. Elworthy, P.H. and K.J. Mysels, The surface tension of sodium dodecylsulfate solutions and the phase separation model of micelle formation. Journal of Colloid and Interface Science, 1966. 21(3): p. 331-347.

248. Dominguez, H. and M. Rivera, Mixtures of Sodium Dodecyl Sulfate/Dodecanol at the Air/Water Interface by Computer Simulations. Langmuir, 2005. 21(16): p. 7257-7262.

249. Hernáinz, F. and A. Caro, Variation of surface tension in aqueous solutions of sodium dodecyl sulfate in the flotation bath. Colloids and Surfaces A: Physicochemical and Engineering Aspects, 2002. 196(1): p. 19-24.

250. Okamura, E., N. Fukushima, and S. Hayashi, Molecular Dynamics Simulation of the Vibrational Spectra of Stearic Acid Monolayers at the Air/Water Interface. Langmuir, 1999. 15(10): p. 3589-3594.

251. Rovillard, S., et al., Monolayer Organization Modeling Using Molecular Dynamics. Langmuir, 1999. 15(8): p. 2749-2754.

252. Dhathathreyan, A. and S.J. Collins, Molecular Dynamics Simulation of (Octadecylamino)dihydroxysalicylaldehyde at Air/Water Interface. Langmuir, 2002. 18(3): p. 928-931.

253. Rodriguez, J., E. Clavero, and D. Laria, Computer Simulations of Catanionic Surfactants Adsorbed at Air/Water Interfaces. The Journal of Physical Chemistry B, 2005. 109(51): p. 24427-24433.

254. Khurana, E., S.O. Nielsen, and M.L. Klein, Gemini Surfactants at the Air/Water Interface: A Fully Atomistic Molecular Dynamics Studyâ€ The Journal of Physical Chemistry B, 2006. 110(44): p. 22136-22142.

255. Clavero, E., J. Rodriguez, and D. Laria, Computer simulations of catanionic surfactants adsorbed at air/water interfaces. II. Full coverage. The Journal of Chemical Physics, 2007. 127(12): p. 124704-7.

256. Yuan, S., et al., Molecular dynamics studies on monolayer of cetyltrimethylammonium bromide surfactant formed at the air/water interface. Colloids and Surfaces A: Physicochemical and Engineering Aspects, 2006. 289(1-3): p. 1-9.

257. Cuny, V., et al., Structural properties and dynamics of C12E5 molecules adsorbed at water/air interfaces: A molecular dynamic study. Colloids and Surfaces A: Physicochemical and Engineering Aspects, 2008. 323(1-3): p. 180-191.

258. Cuny, V., et al., Numerical Analysis of Nonionic Surfactant Monolayers at Water/Air Interfaces. The Journal of Physical Chemistry B, 2004. 108(35): p. 13353-13363.

259. Bandyopadhyay, S. and J. Chanda, Monolayer of Monododecyl Diethylene Glycol Surfactants Adsorbed at the Air/Water Interface: A Molecular Dynamics Study. Langmuir, 2003. 19(24): p. 10443-10448.

260. Chanda, J. and S. Bandyopadhyay, Molecular Dynamics Study of a Surfactant Monolayer Adsorbed at the Air/Water Interface. Journal of Chemical Theory and Computation, 2005. 1(5): p. 963-971.

261. Schweighofer, K.J., U. Essmann, and M. Berkowitz, Simulation of Sodium Dodecyl Sulfate at the Water-Vapor and Water-Carbon Tetrachloride Interfaces at Low Surface Coverage. The Journal of Physical Chemistry B, 1997. 101(19): p. 3793-3799.

262. Andoh, Y. and K. Yasuoka, Two-Dimensional Supercritical Behavior of an Ethanol Monolayer: A Molecular Dynamics Study. Langmuir, 2005. 21(23): p. 10885-10894.

263. Rivera, J.L., et al., Vapor-liquid equilibrium simulations of the SCPDP model of water. Chemical Physics Letters, 2002. 357(3-4): p. 189-194.

264. Rivera, J.L., et al., Polarizable contributions to the surface tension of liquid water. The Journal of Chemical Physics, 2006. 125(9): p. 094712-8.

265. Rivera, J.L., C. McCabe, and P.T. Cummings, Molecular simulations of liquid-liquid interfacial properties: Water-n-alkane and water-methanol-n-alkane systems. Physical Review E, 2003. 67(1): p. 011603-10.

266. Baoukina, S., et al., Pressureâ^'Area Isotherm of a Lipid Monolayer from Molecular Dynamics Simulations. Langmuir, 2007. 23(25): p. 12617-12623.

267. Laing, C., S. Baoukina, and D.P. Tieleman, Molecular dynamics study of the effect of cholesterol on the properties of lipid monolayers at low surface tensions. Physical Chemistry Chemical Physics, 2009. 11(12): p. 1916-1922.

268. Berendsen, H.J.C., J.R. Grigera, and T.P. Straatsma, The missing term in effective pair potentials. J. Phys. Chem., 1987. 91(24): p. 6269-6271.

269. Miyamoto, S. and P.A. Kollman, Settle: An analytical version of the SHAKE and RATTLE algorithm for rigid water models. Journal of Computational Chemistry, 1992. 13(8): p. 952-962.

270. Martin, M.G. and J.I. Siepmann, Novel Configurational-Bias Monte Carlo Method for Branched Molecules. Transferable Potentials for Phase Equilibria. 2. United-Atom Description of Branched Alkanes. The Journal of Physical Chemistry B, 1999. 103(21): p. 4508-4517.

271. Briggs, J.M., T. Matsui, and W.L. Jorgensen, Monte Carlo simulations of liquid alkyl ethers with the OPLS potential functions. Journal of Computational Chemistry, 1990. 11(8): p. 958-971.

272. Jorgensen, W.L., Optimized intermolecular potential functions for liquid alcohols. The Journal of Physical Chemistry, 1986. 90(7): p. 1276-1284.

273. Berk, H., et al., LINCS: A linear constraint solver for molecular simulations. Journal of Computational Chemistry, 1997. 18(12): p. 1463-1472.

274. Ryckaert, J.P. and A. Bellemans, Molecular dynamics of liquid n-butane near its boiling point. Chemical Physics Letters, 1975. 30(1): p. 123-125.

275. Berendsen, H.J.C., D. van der Spoel, and R. van Drunen, GROMACS: A message-passing parallel molecular dynamics implementation. Computer Physics Communications, 1995. 91(1-3): p. 43-56.

276. Lindahl, E., B. Hess, and D. van der Spoel, GROMACS 3.0: a package for molecular simulation and trajectory analysis. Journal of Molecular Modeling, 2001. 7(8): p. 306-317.

277. Van der Spoel, D., et al., GROMACS: Fast, flexible, and free. Journal of Computational Chemistry, 2005. 26(16): p. 1701-1718.

278. Allen, M.P. and D.J. Tildesley, Computer Simulation of liquids. 1987, Oxford: Oxford University Press.

279. Essmann, U., et al., A smooth particle mesh Ewald method. Journal of Chemical Physics, 1995. 103(19): p. 8577-8593.

280. Jamadagni, S.N., et al., How Interfaces Affect Hydrophobically Driven Polymer Folding. Journal of Physical Chemistry B, 2009. 113(13): p. 4093-4101.

281. Godawat, R., S.N. Jamadagni, and S. Garde, Characterizing hydrophobicity of interfaces by using cavity formation, solute binding, and water correlations. Proceedings of the National Academy of Sciences of the United States of America, 2009. 106(36): p. 15119-15124.

282. Garde, S., et al., Molecular dynamics simulation of C8E5 micelle in explicit water: structure and hydrophobic solvation thermodynamics. Molecular Physics, 2002. 100(14): p. 2299-2306.

283. Stewart, E., R.L. Shields, and R.S. Taylor, Molecular Dynamics Simulations of the Liquid/Vapor Interface of Aqueous Ethanol Solutions as a Function of Concentration. The Journal of Physical Chemistry B, 2003. 107(10): p. 2333-2343.

284. Bai, H., et al., Non-covalent functionalization of graphene sheets by sulfonated polyaniline. Chemical Communications, 2009(13): p. 1667-1669.

285. Alejandre, J., et al., Force field of monoethanolamine. Journal of Physical Chemistry B, 2000. 104(6): p. 1332-1337.

286. Carless, J.E., R.A. Challis, and B.A. Mulley, Nonionic surface-active agents. Part V. The effect of the alkyl and the polyglycol chain length on the critical micelle concentration of some monoalkyl polyethers. Journal of Colloid Science, 1964. 19(3): p. 201-212.

287. Dahanayake, M., A.W. Cohen, and M.J. Rosen, Relationship of structure to properties of surfactants. 13. Surface and thermodynamic properties of some oxyethylenated sulfates and sulfonates. The Journal of Physical Chemistry, 1986. 90(11): p. 2413-2418.

288. Nath, S.K., F.A. Escobedo, and J.J. de Pablo, On the simulation of vapor--liquid equilibria for alkanes. The Journal of Chemical Physics, 1998. 108(23): p. 9905-9911.

7. Appendices

Appendix A: Adsorption Isotherms of Aqueous $C_{12}E_6$ and CTAB Surfactants on Solid Surfaces in the Presence of Low-Molecular-Weight Co-Adsorbents

The material presented below was published in 2009 in volume 25, issue 10, of the journal 'Langmuir'. Some modifications have been made after the paper has been published.

A.1 Abstract

In this work, we evaluate the effects of the low-molecular-weight compounds toluene, phenol and 1-hexanol on the adsorption of two surfactants on one solid surface. The surfactants are CTAB (cationic) and $C_{12}E_6$ (non-ionic). The surface is gold, although x-ray photoelectron spectroscopic analysis reveals the presence of a large number of oxygenated sites that render the surface hydrophilic (contact angle 10°). Adsorption isotherms are measured using a quartz crystal microbalance with dissipation monitoring (QCM-D). Although our measurements do not allow the determination of the morphology of the aggregates directly, we rationalize our results by referring to AFM images from the literature. Based primarily on the dissipative signal and on AFM studies done by others, our results are consistent with CTAB forming a patchy cylindrical structure, and $C_{12}E_6$ likely yielding a monolayer structure. The presence of co-solutes almost doubles the mass of surface aggregates and increases the rigidness of

the aggregates for CTAB, consistent with a morphological change from cylinders to flat bilayers. Part of the increase in adsorbed mass is likely due to increased surface area covered by admicelles. For $C_{12}E_{6,}$ co-solutes cause small changes in the mass adsorption and essentially no change in the flexibility of surface aggregates.

A.2 Introduction

Surfactant adsorption on solid surfaces plays an important role in detergency, mineral flotation, corrosion inhibition, solid dispersion, oil recovery, etc.[165] Ellipsometry,[166-168] atomic force microscopy,[169-174] surface plasmon resonance,[175] and specular neutron reflection[176-178] have all been used to study surfactant adsorption at solid-liquid interfaces.

Using atomic force microscopy (AFM), Velegol et al.[179] concluded that CTAB on hydrophilic silica forms a combination of long and short rod-like structures; rod-like structures are also found on graphite[180] and mica.[181] For the latter, with no added electrolyte the preferred aggregate morphology is a flat layer; although rod-like structures form at short times and become the preferred shape in the presence of swamping electrolyte. Very recent AFM work for CTAB adsorption on gold indicates rod-like structures as well. On rough surfaces, the characteristic morphology of CTAB aggregates remains hemicylindrical, although the aggregates became much shorter and in some cases almost hemispherical.[174, 182]

AFM data have been reported on the ethylene oxide nonionic surfactants with the general structure $C_mE_{n,}$[183] although none, to our knowledge, has been reported for

$C_{12}E_6$. On hydrophilic silica, globular aggregates were imaged for $C_{10}E_6$ and $C_{14}E_6$.[184] For the latter surfactant, a flat bilayer was imaged if the distance from the tip to the surface was large, suggesting perhaps that flat layers are the equilibrium morphology and that when the tip approaches the surface it disrupts the surfactant structure. On graphite, $C_{14}E_6$ formed rod-like structures while $C_{10}E_6$ formed a flat layer; on an organic hydrophilic surface both surfactants formed flat layers.

Adsorption isotherms from aqueous solution on solid surfaces have also been investigated using the quartz crystal microbalance (QCM).[185-189] Stalgren et al.[185] found that QCM overestimates the adsorption of the nonionic surfactant $C_{14}E_6$ on both a hydrophobic and a hydrophilic surface compared to ellipsometry results. Similarly, Macakova et al.[188] reported that QCM overestimates the adsorption of the cationic surfactants cetyltrimethylammonium bromide (CTAB) and didodecyltrimethylammonium bromide (DTAB) on solid surfaces when compared to optical reflectometry data. To explain these discrepancies the authors suggested that the QCM measurements also include water immobilized within or near the adsorbed surfactant aggregates.

The majority of previous studies on surfactant adsorption were conducted from pure water, or aqueous solutions of carefully controlled pH and ionic strength. However, in most applications adsorption occurs in the presence of low-molecular-weight compounds. For example, one important application is the use of surfactants to enhance subsurface remediation of hydrocarbon contamination and the related enhanced oil recovery.[190-193] It has also been proposed to take advantage of the adsolubilization of compounds within the surface surfactant aggregates (also known as

‘admicelles’) to design separation processes such as ‘admicellar chromatography. More recently, the phenomenon of adsolubilization has been exploited in admicellar polymerization, during which monomers are adsolubilized within surfactant aggregates and then polymerized to yield polymers on surfaces.[194-198] Recent developments of such techniques allowed Marquez et al.[199] to produce nano-structured polymeric films on surfaces. Understanding how various co-solutes partition between the supernatant bulk phase and the admicellar phase is expected to contribute to the further development of these, and other applications.

Lee et al.[200] used solution-depletion methods to study the adsolubilization of alcohols in SDS admicelles formed on alumina. At SDS concentrations below the cmc the presence of alcohols increased the adsorbed amount typically by a factor of 10. At SDS concentrations above the cmc, however, all the adsorption isotherms (the alcohols considered were 1-propanol, n-butanol, n-pentanol, n-hexanol, and n-heptanol) collapsed onto one single curve, which was not very different to that measured for SDS alone. In the case of alkanes adsolubilization in SDS it was found that the adsolubilization in admicelles was very similar to the solubilization in bulk micelles,[201] and that the alkane partition coefficient within the admicelles increases as the adsorbed surfactant amount increases.[113] To interpret the results, Lee et al. proposed a two-site adsolubilization model for the adsorption of alcohols.[200] According to this model alcohols can adsorb on the palisade of the admicelles, but also along the edges of patchy structures. Another two-site solubilization model was proposed earlier by Mukerjee and Cardinal[202] to rationalize the solubilization of benzene within micelles. Benzene could dissolve in the hydrophobic core of the

micelles, as well as adsorb in the polar micelle surface. The availability of various solubilization sites within micelles was further proved by Rouse et al.[193] Nayyar et al.[203] studied the adsolubilization of naphthalene, 4-amino-1-naphthalene sulfonic acid (ANSA), and naphthol within SDS admicelles on alumina. The study was conducted at bulk SDS concentrations below the cmc, and provided partition coefficients for the co-solutes between the bulk aqueous phase and the admicelles. Naphthalene, hydrophobic, was easily adsolubilized at low SDS concentrations, but as the SDS concentration increased naphthalene was solubilized by both SDS micelles and admicelles. The adsolubilization of naphthol, an alcohol, was very large at low SDS concentrations, and decreased as the SDS concentration increased, as expected based on the two-site adsolubilization model. The third co-solute, ANSA, was strongly adsorbed on alumina in the absence of SDS, and increasing SDS concentration induced a competition between ANSA and SDS molecules for surface adsorption sites, resulting in decreased ANSA adsorption.

Those pioneering studies have been periodically revisited[204] and extended.[205-208] Additional insights are expected from molecular simulations,[209-211] which are at present hindered by the enormous computational resources required. Particularly relevant to this manuscript is the work of Wall and Zukoski,[169] who reported an AFM study of alcohol-induced structural transformations of CTAB aggregates adsorbed on mica. The supernatant aqueous bulk solution contained 10mM KCl and 9mM CTAB. They found that as the concentration of 1-hexanol increased in the bulk solution, the morphology of surface CTAB aggregates changes from cylindrical to spherical, and eventually becomes flat when the 1-hexanol concentration is larger than 20mM. A

switch from a curved morphology to a flat bilayer, has been found for other solvent/surfactant/surface combinations.[212, 213] It is likely that the incorporation of co-solutes into the admicelle causes this morphological transformation because a flat bilayer has a much greater capacity for adsolubilization. However, AFM does not give any information about the adsorbed mass.

The goal of this work is to assess the effects of the presence of co-solutes on the adsorption of two surfactants on a solid surface in terms of total adsorbed mass and dissipation as a function of bulk surfactant and co-solute concentration. Dissipation was measured to monitor the flexibility of the admicelles, which, based on our data, seems to be an indirect measurement of admicelle morphology. Surfactants considered were CTAB (cationic), and hexaethylene glycol monododecyl ether, $C_{12}E_6$ (non-ionic). The surface was gold, although XPS analysis revealed the presence of a large number of oxygen atoms that render the surface hydrophilic.[189] Co-solutes were toluene (hydrophobic), phenol, and 1-hexanol (partially hydrophilic).

A.3 Materials and Methods

A.3.1 Instrumentation

Adsorption isotherms were measured at T=25±0.05°C by a quartz crystal microbalance with dissipation (QCM-D), model E4, purchased from Q-Sense AB. Data reproducibility was checked by performing independent measurements, with a quartz crystal microbalance with impedance monitoring (QCM-Z500, KSV Instruments Ltd., Finland). In these control experiments the temperature of the measuring chamber was

kept at 20.0°±0.1°C with a Peltier unit, the room temperature was 21°C with an average relative humidity of 46%.

A.3.2 Reagents

For all the experiments discussed herein CTAB was purchased from Sigma-Aldrich (cetyl-trimethyl-ammonium bromide, minimum 99%). After purification,[214] a 10 mM stock solution of CTAB was prepared. $C_{12}E_6$ was purchased from Sigma-Aldrich (hexaethylene glycol monododecyl ether, semisolid) and used as received. A 3.414 mM stock solution was prepared. Toluene (spectrophotometric grade, 99.7+%) was purchased from Alfa Aesar. Phenol solution (maximum impurities and specifications 88% phenol, 12% water) was purchased from EM Science. And 1-hexanol (Puriss plus, >99.5% GC) was purchased from Sigma-Aldrich. 18.2 MΩ cm resistivity water was used to prepare the aqueous surfactant solution.

All substrates used were gold 50 nm (QSX 301), purchased from Q-Sense AB. Before any experiment, the crystal surfaces are cleaned following the standard cleaning protocols proposed by Q-Sense. XPS analysis reveals that after the cleaning process a large number of oxygen atoms are present on the crystal surfaces. Thus the surfaces used in our experiments are hydrophilic as confirmed by a 10° contact-angle. According to the AFM analysis shown in Figure 7-1, the surface of the gold crystal is fairly smooth. Nominal surface area of the gold crystal is used in this report.

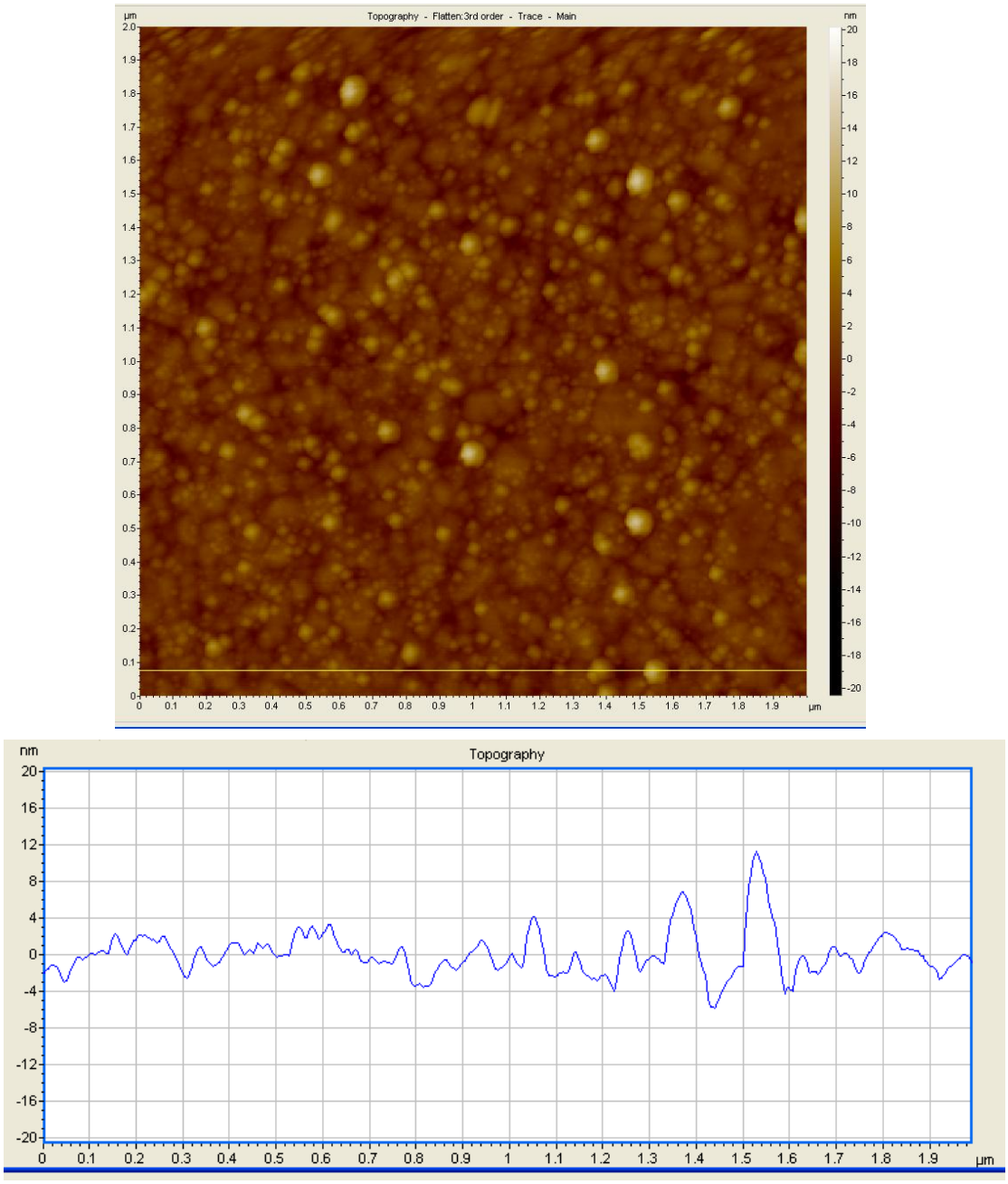

Figure 7-1 AFM image and section analysis of the surface structure of the gold crystal after the cleaning procedure.

A.3.3 Methods

A schematic of our experimental setup is given in our previous paper.[189] Every measurement started by first obtaining a baseline for each crystal in contact with the solvent solution, i.e. no surfactant. In our experiment, five aqueous solutions were used. They were nanopure water, 0.47g/L saturated toluene aqueous solution, 0.47g/L 1-hexanol aqueous solution, 0.47g/L and 1.88g/L phenol aqueous solution. The 0.47 g/L was chosen because this is the maximum solubility of toluene in water at room conditions; 1.88 g/L was chosen because it is much larger than 0.47 g/L. An adsorption isotherm measurement consisted of increasing the bulk surfactant concentration from 0 to approximately 1.5*cmc in steps of ~0.1*cmc. At each concentration, surfactant solution was pumped through the instrument using an Ismatec peristaltic pump at a constant flow rate of 0.1mL/min for 1 h. The flow rate of the peristaltic pump quickly decreased compared to the nominal flow rate due to tube aging. To avoid complications the flow rate of the peristaltic pump was assessed before each experiment and the tubing replaced on the average every three experiments. To reach equilibrium, it was necessary to wait, sometimes for up to 2-3 h. Equilibrium was confirmed by allowing the system to equilibrate overnight for some data points throughout the adsorption isotherms. Between adsorption isotherm measurements, we found it necessary to clean the system using a 2% (69 mM) aqueous sodium dodecyl sulfate solution in order to obtain more consistent and reproducible results; presumably SDS is able to remove all residual surfactant and solute. SDS was fluxed through the tubing for 1 hour and then nanopure water was fluxed through the modules for 3 hours to remove SDS traces. With this procedure, the blank QCM measurement, i.e. the measurement with only water flowing

through the system, was returned to its starting point. It is possible that other procedures (e.g., flowing chloroform or aqueous solutions of ethanol) would provide satisfactory cleaning of crystal surfaces and tubings. SDS solutions were a natural choice for us, thus no attempt was made to optimize the cleaning procedure.

The solution pH was monitored before and after the adsorption measurements by an Oakton pH meter (pH 510 series). When adsorption occurs from pure water and from the toluene solution, the pH remained approximately neutral. When adsorption occurs from solutions containing alcohols, the pH decreased as the phenol concentration increased. For 1.88g/L phenol solution, the pH decreased to ~5.9. For adsorption from the 0.47g/L phenol and 1-hexanol solutions the pH remained at ~6.3 during the entire experiment.

A.3.4 Theory

QCM-D measures two quantities, frequency and dissipation, simultaneously in real-time, as molecular layers form on the sensor surface. When a mass, Δm, adsorbs on the sensor surface, the resonant frequency of the crystal sensor, f, decreases from its in nominal value f_0. If the mass adsorption is evenly distributed, rigidly attached to the crystal and small compared to the mass of the crystal, then $\Delta f = f - f_0$ can be related to the adsorbed mass per unit area, Δm, using the Sauerbrey relation

$$\Delta m = \frac{C\Delta f}{n} \tag{7-1}$$

In equation (7-1) C is the mass sensitivity constant ($C=-17.7\ ng\cdot cm^{-2}\cdot Hz^{-1}$ for the crystals used in our experiment at 5MHz) and n is the overtone number (n=1, 3, …). For the crystals used herein, all with nominal fundamental oscillation frequency 5MHz,

the actual fundamental oscillation frequency reduces to as little as 4.95MHz, in which case C should be about -18. Because each crystal used has a different fundamental oscillation frequency (due to small variations in mass, etc.), for consistency we used C=-17.7 in all our calculations, introducing an uncertainty of ~2%. This is well within the experimental uncertainty introduced by other factors.

Variations in the oscillation frequency Δf were measured by neglecting the data corresponding to the first overtone (the results of which tend to be erratic), and by considering 3^{rd}, 5^{th}, 7^{th}, 9^{th}, 11^{th}, and 13^{th} overtones. In some cases, the data corresponding to a particular overtone were erratic, and therefore discarded.

The dissipation factor, which reflects the viscoelasticity of the adsorbed films, is defined as

$$D = \frac{E_{diss}}{2\pi E_{stor}} \tag{7-2}$$

where E_{diss} is the dissipated energy and E_{stor} is the stored energy during the oscillation cycle. With the QCM-D, the change in the dissipation factor, $\Delta D = D - D_0$, is measured, where D is the dissipation factor at any given time during the experiment and D_0 is the dissipation factor of a clean crystal immersed in the solvent. A large value for ΔD is representative of a large energy loss, which is typical for a soft film attached to the quartz crystal. A small ΔD is representative of a rigid adsorbed structure. The exact limits of this qualitative discrimination depend on the ratio between viscosity and elasticity of the adsorbed film.[215] It is in general assumed that the Sauerbrey model is not expected to hold when the dissipation increases above $2*10^{-6}$,[216] although recent reports suggest that the model works as long as the adsorbed film is 'thin'.[217] When surfactant adsorption is studied by QCM, it is in general assumed that the

Sauerbrey relation is sufficiently accurate because the change in dissipation is generally low (below 10^{-6}). At larger dissipation values, the Sauerbrey relation may underestimate the adsorbed mass, and alternative models that adopt a viscoelastic description of the adsorbed film[179] could be used.[218]

A.4 Results and Discussions

A.4.1 Bulk Properties

Critical micelle concentrations (cmc) were obtained from the surface tension/log concentration plot as the intersection point of the two best linear fitting for low and high concentrations. Surface tension measurements were carried out with a static tensiometer (SIGMA70, KSV Instruments Ltd, Finland) using the Du Noüy ring method. All measurements were performed at constant temperature of 25.0 ± 0.5°C. The sample was progressively diluted by adding the appropriate amount of solvent. Before starting the measurement, the sample was stirred for 1 min and equilibrated for 10 mins.

Table 7-1 Critical micelle concentrations (mM) of CTAB and $C_{12}E_6$ in the various aqueous solutions considered here.

	Water	*0.47g/L Toluene*	*0.47g/L 1-hexanol*	*0.47g/L Phenol*	*1.88g/L Phenol*
CTAB	0.88±0.01	0.89±0.02	0.84±0.01	0.79±0.03	0.64±0.02
$C_{12}E_6$	0.072±0.004	0.073±0.001	0.076±0.003	0.068±0.001	0.046±0.001

A.4.2 Adsorption isotherms from pure water

In Figure 7-2 we report the adsorption isotherms of $C_{12}E_6$ and CTAB from pure water on gold. In the case of CTAB (▲), the adsorption isotherm follows a typical L-shape adsorption isotherm. The amount adsorbed at low bulk concentrations is quite large. The value at 0.1 cmc is about 110 ng/cm^2, almost half of the highest mass adsorption for this surfactant. As the bulk concentration increases above 0.6*cmc, the mass adsorption increases slowly. This is in agreement with the third stage of typical L4 Somasundaran-Fuerstenau-type adsorption isotherms for ionic surfactants on oppositely-charged surfaces. In this third stage electrostatic hindrance due to interfacial charge reversal delays the rate of surfactant adsorption. When the bulk concentration is increased above 1.0*cmc, the mass adsorption, as measured by QCM-D, reaches the plateau of 250 ng/cm^2 and does not increase further.

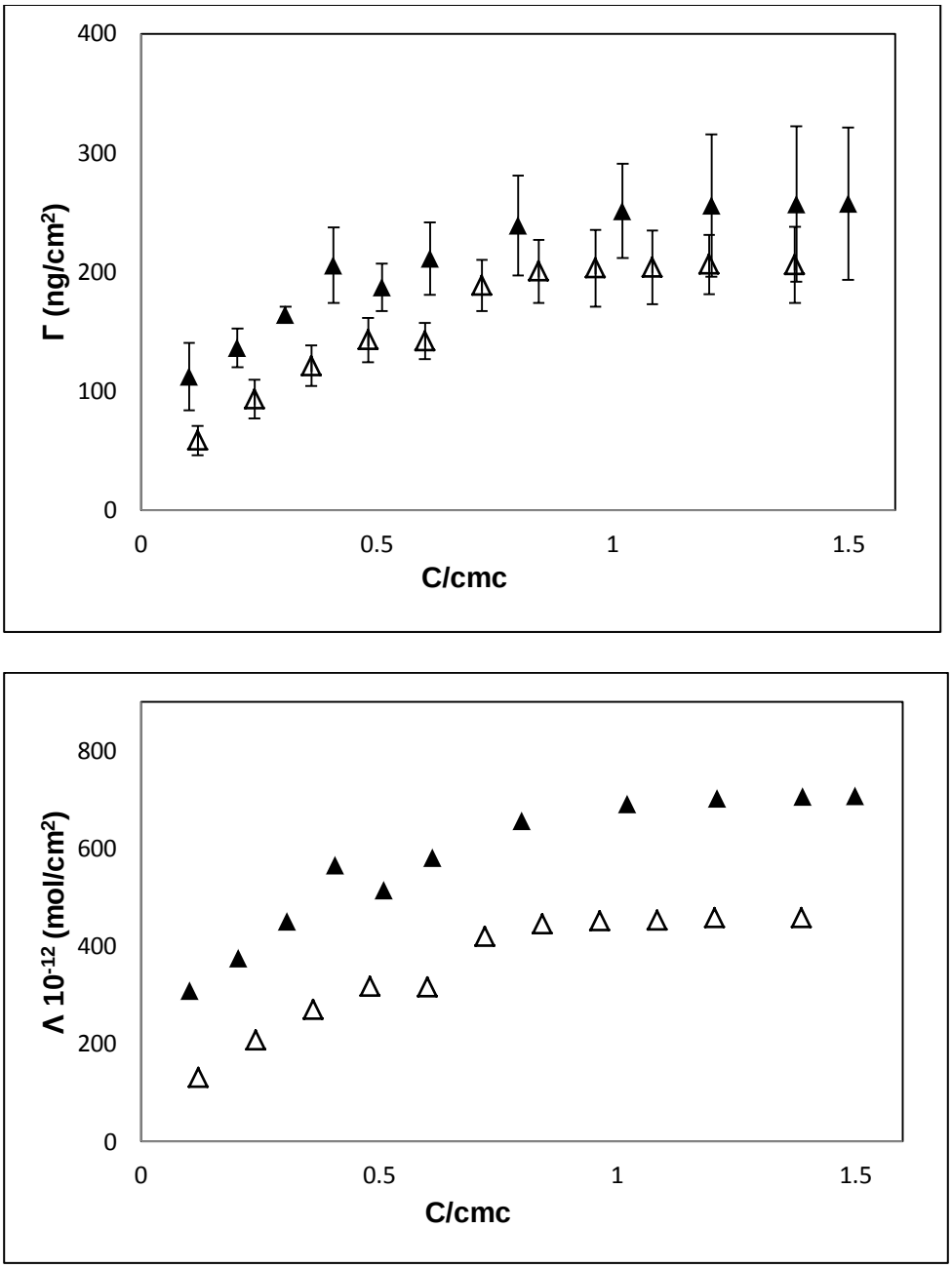

Figure 7-2 Experimental adsorption isotherms for CTAB(▲) and $C_{12}E_6$ (△) on gold at 25±0.05 ^{o}C. Top panel is the mass adsorption showing the error associated with our experiments, which was determined by 4 to 8 experiments. The bottom panel is the calculated mole adsorption, in which the error bars are not shown for clarity.

In contrast to ionic CTAB, the results for nonionic $C_{12}E_6$ (△) exhibits an S shape adsorption isotherm, as discussed by Clunie and Ingram. The amount adsorbed increases gradually at low concentrations and shows a sharp increase at about 0.6*cmc. We point out that the adsorption of $C_{12}E_6$ is less than that of CTAB at low bulk surfactant concentrations. The maximum measured mass adsorption remains ~200 ng/cm^2 even as the bulk concentration increases above the cmc.

Adsorption isotherms are also expressed in terms of mole of surfactants per unit surface area as shown in the bottom panel of Figure 7-2. Our results are similar to those reported previously by our group, except that previous data showed continuing surfactant adsorption when the bulk surfactant concentration increased above 1.0*cmc. The discrepancy is likely due to the more careful experimental adsorption isotherms measured for the present manuscript and is clearly an indication of the difficulty typically encountered in measuring accurate adsorption isotherms.

The surface area per head groups available from literature[219] are ~0.46 nm^2 for CTAB and ~0.52nm^2 for $C_{12}E_6$. Although these values are obtained at the water-air interface, they allow us to calculate the total number of moles adsorbed on each crystal. The calculated amount of CTAB or $C_{12}E_6$ necessary to form one monolayer on the crystal surfaces used in our experiments correspond to ~0.29 and ~0.26 nmol, respectively. Our experimental results indicate that, in correspondence of the cmc, ~0.55 and ~0.35 nmol of CTAB and $C_{12}E_6$ adsorb on the crystals. Considering that QCM-D may little overestimate the adsorption,[185, 188] our data indicate the formation of a monolayer-like structure for $C_{12}E_6$ and a 3/2 layer-like structure for CTAB. We use the terms monolayer-like because our measurements do not allow us to

discriminate between the morphology of the aggregates. Note, as stated earlier the area per head group is an estimate since it was calculated from the air-liquid interface.

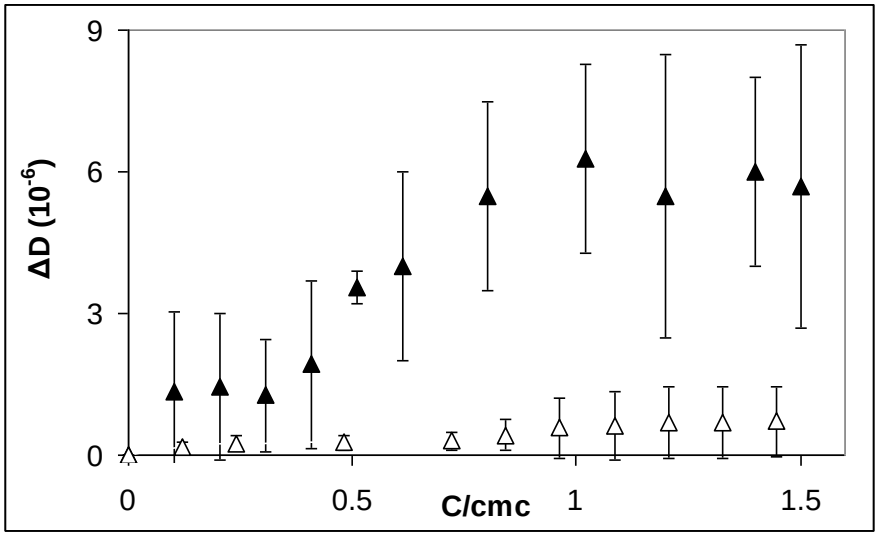

Figure 7-3 Measured change in dissipation factor for CTAB(▲) and $C_{12}E_6$ (△) surfactant aggregates adsorbed on gold corresponding to the adsorption isotherms shown in Figure 7-2.

QCM-D also measures the change in dissipation parameter, which enables the assessment of the change in flexibility of the surface aggregates. In Figure 7-3, ΔD for both CTAB and $C_{12}E_6$ is shown as a function of bulk concentration. In both cases ΔD is small at low bulk concentrations and increases as the bulk concentration approaches the cmc. At concentrations above 1.0*cmc, both changes in dissipation factors stop increasing, indicating a stable, likely equilibrated, surface structure. For CTAB, ΔD is larger than for $C_{12}E_6$ at any measured concentration which indicates that the CTAB surface aggregates are much more flexible than the $C_{12}E_6$ ones.

Based on previous AFM analysis, CTAB is likely to form cylindrical aggregates on our crystals. Because our estimates for the adsorbed amount suggest the formation of 3/2 of a monolayer, it is possible that some surface regions are not covered by CTAB cylindrical aggregates. This may be a consequence of both surface roughness and chemical heterogeneity. In any case, cylindrical aggregates that do not completely cover the surface seem to be consistent with large dissipations, as shown in Figure 7-3. Unfortunately, however, large dissipations and non-homogeneous surface coverages both limit the applicability of the Sauerbrey model, as we will discuss shortly.

As opposed to the data for CTAB, our results for $C_{12}E_6$ suggest the formation of a complete monolayer. Such structure is expected to be rigid, which is consistent with low dissipations, as shown in Figure 7-3. Thus, limited to our systems, it appears that large dissipations (above $2\text{-}3*10^{-6}$) are signature of cylindrical aggregates, while low dissipations ($\sim 1*10^{-6}$) are signature of monolayers. The aggregate morphologies that we expect form on our crystals above the cmc are shown in the top panels of Figure 7-4.

The large dissipation values measured in the CTAB experiments approach the limits of validity of the Sauerbrey model. We attempted to assess the measured amount using the Voigt viscoelastic model, as described in Ref.[65] The implementation of the model requires as input the density of the adsorbed film, and density and viscosity of the supernatant solution to yield the total adsorbed mass.[220] Using reasonable estimates (1.09 g/cm^3 for the density of the adsorbed film, 1 g/cm^3 and 0.001 Kg/(m•s) for density and viscosity of the supernatant), we obtained an adsorbed mass slightly larger than that reported in Figure 7-2, top panel, for each bulk CTAB concentration. If dissipation values larger than the average data reported in Figure 7-3 are used, then

larger adsorbed masses are obtained, which imply unrealistic thicknesses of the adsorbed film. Because it is likely that the viscoelastic model accounts for solvent not only trapped within the admicelles, but also near them, we consider the values obtained from the Sauerbrey model more realistic because surfactant films are expected to be quite thin.

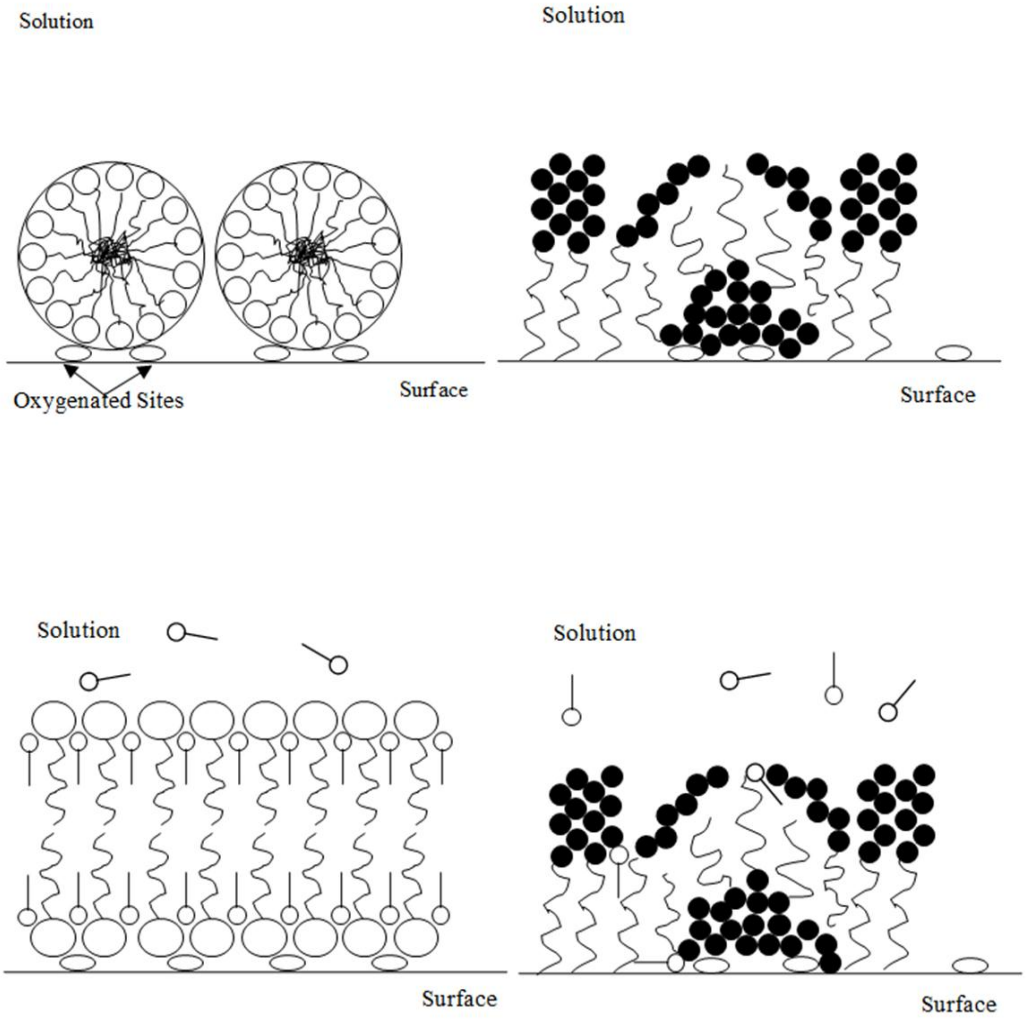

Figure 7-4 Expected structures of CTAB (left panels) and $C_{12}E_6$ (right panels) admicelles on gold crystals. The top panels represent the admicelles formed from pure water, the bottom ones represent those formed in the presence of co-solutes. For clarity surface roughness is not shown.

A.4.3 Co-Solute Effects: CTAB

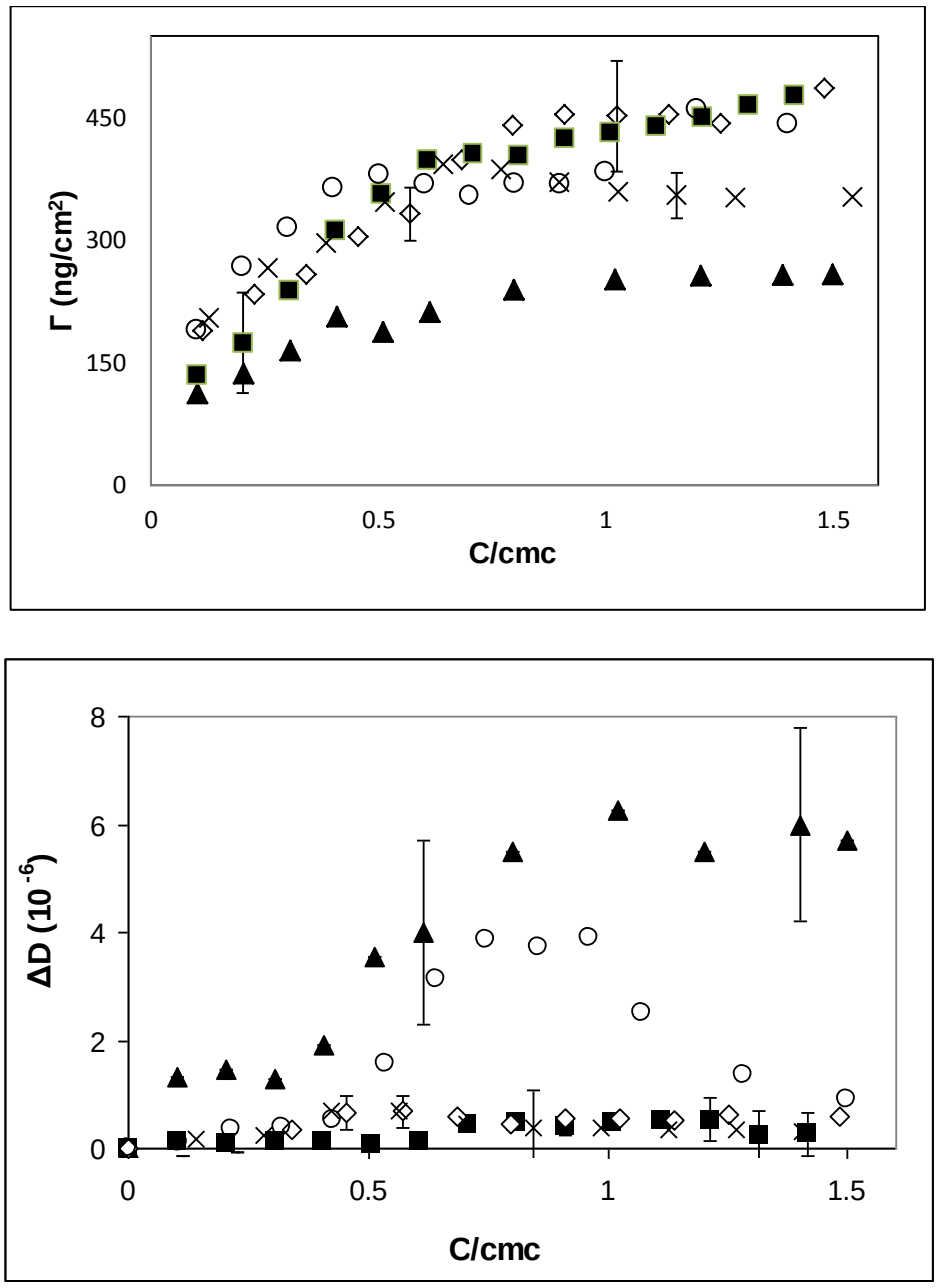

Figure 7-5 Experimental adsorption isotherms (top) and measured change in dissipation factor (bottom) for CTAB adsorbed on gold from pure water (▲), 0.47g/L aqueous solution of toluene (■) , 0.47g/L 1-hexanol (o) , 0.47g/L phenol (◊) and 1.88g/L aqueous solution of phenol (x). For clarity, only representative error bars are reported.

In Figure 7-5 are reported adsorption isotherms for CTAB on gold in the presence of co-solutes. The shapes of the adsorption isotherms are similar to that of CTAB from pure water (▲), except that the presence of co-solutes yields larger adsorbed amounts at every surfactant bulk concentration. This observation is consistent with the data reported by Lee at al.[200] for alcohols adsolubilization in SDS admicelles, as well as for those of Nayyar et al.[203] for naphthalene and naphthol. The main difference, however, is that the adsorption isotherms do not collapse into a single one as the CTAB concentration increases above its cmc, as was observed in those papers.

Adsorption with toluene and phenol is around 300ng/cm^2 at 1.0*cmc and is approximately constant above the cmc, although with toluene the amount adsorbed may increase slightly. In the case of 0.47g/L (4.6 mM) 1-hexanol aqueous solution, the adsorption at low concentrations is a little larger than that observed from the phenol solution at the same concentrations. When the bulk surfactant concentration increases to above 0.6*cmc the obtained mass adsorption becomes smaller than that measured from 0.47g/L phenol solution. When the concentration of phenol is increased to 1.88g/L (18mM), our results indicate that the adsorbed amount below the cmc does not change vs. the 0.47 g/L phenol, suggesting that the admicelles at those conditions are saturated with phenol. Once the CTAB concentration increases above the cmc, however, there is a reduction in adsorbed amount vs. the 0.47 g/L phenol, possibly suggesting that, at this high concentration, phenol competes with surfactant for adsorption sites on gold.

The measured ΔD values (Figure 7-5, bottom) show that, except when the 1-hexanol solution is used, co-solutes reduce ΔD significantly compared to the value

measured in pure water. Note that the measured ΔD are in most cases within the limits of applicability of the Sauerbrey model. In the case of 1-hexanol, the results for ΔD are very similar to those measured from water at low bulk surfactant concentrations; i.e., they show an increase in ΔD as the bulk surfactant concentration increases to ~0.8*cmc. However, when the surfactant concentration increases further ΔD decreases to the low values observed for all the other systems in the presence of co-solutes. As co-solutes are added to the system, our data suggest that, above the cmc, dissipation for CTAB aggregates decreases compared to that measured in pure water for all co-solutes (Figure 7-5, bottom panel). With the knowledge from previously discussed AFM studies that on flat surfaces the addition of low molecular weight compounds causes a change in CTAB aggregates from a morphology that is approximately cylindrical to one that is flat,[169, 212, 213] our observations are consistent with a morphological change from cylindrical to flat bilayer structures in the case of CTAB upon the addition of co-solutes. The proposed admicelle morphology is sketched in Figure 7-4, bottom left panel.

The explanation just provided, however, does not account for the unusual behavior observed for the dissipation of CTAB aggregates in the presence of 1-hexanol (Figure 7-5, bottom panel). The molecular architecture of 1-hexanol, a linear hydrophobic chain with a small polar head, may be responsible for the different behavior compared to the other co-solutes. The dissipation data suggests that with 1-hexanol, admicelles formed at low CTAB concentration maintain the same morphology as those formed with CTAB alone. However, when CTAB concentration increases above 0.8*cmc, the admicelles begin to change morphology and probably become flat. The fact that the transition from cylindrical to lamellar morphology occurs over a range of bulk surfactant

concentrations suggests that bilayers coexist with cylindrical micelles at some surfactant concentrations. This likely is an indicator that surface roughness and heterogeneous composition influence the admicelle morphology.

A.4.4 Co-Solute Effects: $C_{12}E_6$

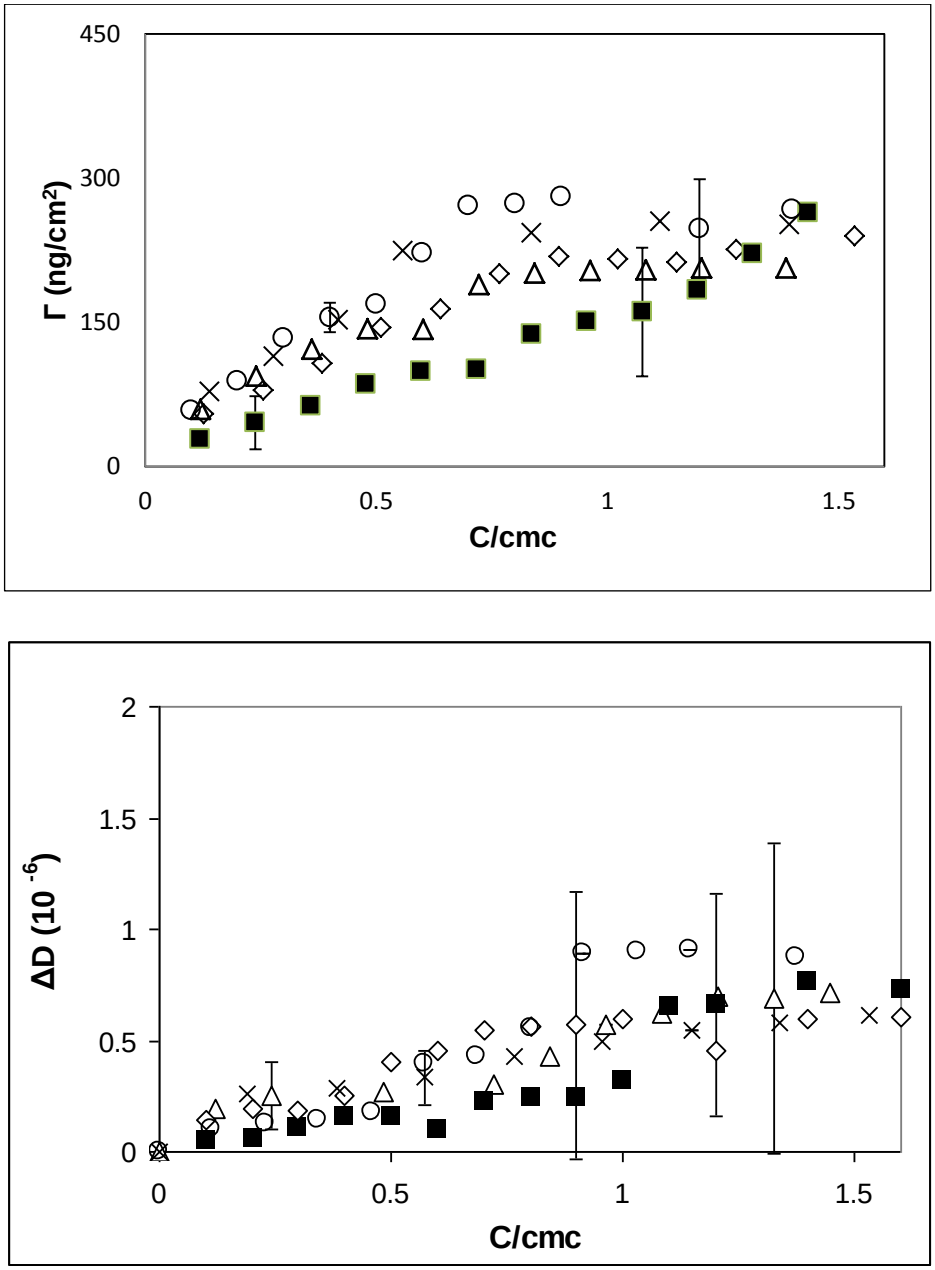

Figure 7-6 Experimental adsorption isotherms (top) and measured change in dissipation factor (bottom) for $C_{12}E_6$ on gold from pure water (△), 0.47g/L aqueous solution of toluene (■), 0.47g/L 1-hexanol (o), 0.47g/L phenol (◊) and 1.88g/L phenol (x). For clarity only representative error bars are shown.

In Figure 7-6 are reported the data for $C_{12}E_6$ adsorption in the presence of co-solutes. All the observed adsorption isotherms show the classic S shape, with a sudden increase at around 0.6*cmc, except in the case of adsorption from aqueous solutions of toluene. In this latter case, the measured adsorbed amount keeps increasing as the bulk $C_{12}E_6$ concentration increases even above 1.0*cmc. Toluene is the only co-solute in the presence of which the measured adsorption isotherm lies below that measured for $C_{12}E_6$ from pure water. Both these observations can be explained by a pronounced toluene adsorption on the solid substrate before the addition of $C_{12}E_6$ to the system.

To rationalize these results we point out that in each experiment the baseline was obtained before beginning to measure the adsorption isotherm. These baselines were obtained by exposing the crystals to the aqueous solution of interest without surfactants present. When we compared the resonance frequency when pure water was substituted with the other four aqueous solutions we found that the resonance frequency decreased by an average of 3 Hz for aqueous solution of toluene, 1.5 Hz for 0.47g/L aqueous solution of phenol or 1-hexanol and 2.5 Hz for 1.88g/L aqueous solutions of phenol. According to the Kanazawa relation,[221] these small changes in oscillation frequency are consistent with small changes in density and viscosity of the aqueous solutions due to the addition of the co-solutes. However, they could also indicate some co-solute adsorption on the crystals. Because the largest baseline shift is observed for toluene, it is likely that this co-solute adsorbs on the surfaces. The fact that the $C_{12}E_6$ adsorption isotherm in the presence of toluene is below that measured from pure water, as well as the continuous increase of the adsorbed amount observed as $C_{12}E_6$ concentration increases, are both consistent with a competitive adsorption between toluene and $C_{12}E_6$

for adsorption sites on the surface. As the $C_{12}E_6$ bulk concentration increases more and more toluene is replaced by the surfactant, and when micelles are available toluene can be solubilized in their interior. Similar effects were observed by Nayyar et al.[203] in the case of co-adsorption of ANSA and SDS on alumina.

Adsorption isotherms from solutions containing 1-hexanol and phenol at high concentration show an enhancement in the adsorbed amount for surfactant concentrations between 0.5 and 1.5 times the cmc. The results obtained from low concentration phenol are statistically indistinguishable from those obtained in pure water. Comparing the two phenol results suggests that the partition coefficient for phenol depends on phenol concentration at surfactant concentrations above 0.5 cmc.

The observations above can be quantified by evaluating the number of co-solute molecules that are adsolubilized at 1.0*cmc for $C_{12}E_6$ (Table 7-2). In the presence of 0.47g/L 1-hexanol, 1.3 1-hexanol molecules are adsolubilized per each $C_{12}E_6$ molecule. In the presence of phenol at the same concentration, only 0.4 phenol molecules adsolubilize per each $C_{12}E_6$. The difference between data obtained for phenol and 1-hexanol is probably due to the structural difference between the two co-solutes. 1-hexanol is a rather straight molecule while phenol contains an aromatic ring. Thus 1-hexanol encounters less steric hindrance when it adsolubilizes in the palisade of $C_{12}E_6$ admicelles.

The results obtained for changes in dissipation factor (Figure 7-6, bottom) indicate that, under the conditions considered herein, admicelles obtained from aqueous $C_{12}E_6$ on our crystals do not change in flexibility when toluene, 1-hexanol, of phenol are present as co-solutes. Thus our data are consistent with no substantial morphological

change in the case of $C_{12}E_6$ admicelles. The expected admicelle morphology for $C_{12}E_6$ admicelles in the presence of co-solutes is sketched in Figure 7-3, bottom right panel.

A.3.5 Comparison and Interpretation

To further compare the co-solute effects on the surface aggregates for both $C_{12}E_6$ and CTAB we report in Figure 7-7 the total mass adsorbed and the change in dissipation factor measured in correspondence to bulk surfactant concentration equal to the cmc. In Table 7-2 we also report the net adsorption of co-solutes per surfactant molecule from different aqueous solutions assuming that all of the increase in mass is due to solute adsorption (i.e. the amount of surfactant adsorbed remains constant). First we should consider hexanol and phenol at 0.47 g/L. The most obvious observation is that the amount of solute adsorbed for CTAB is much larger than that for $C_{12}E_6$. It is not clear why the number of molecules adsolubilized per adsorbed surfactant molecule by CTAB appear to be so much larger. One very distinct possibility is that the larger apparent values are due to both solute adsorption and an increase in CTAB adsorption due to spreading of the admicelles over a wider surface caused by the change in morphology from cylinders to bilayers. If we assume that the fractional surface coverage for CTAB changes from 75% to 100% (amount covered by the flat layer of $C_{12}E_6$), then the amount of adsolubilized solute per surfactant molecule is roughly identical for the two surfactants. A patchy bilayer for pure $C_{12}E_6$ would not allow this argument to be made, and an alternate, likely unsatisfying, explanation would be required for explaining the data in Table 7-2. Based on Table 7-2, some quantitative comparisons are possible. Kandori et al.[222] reported that the maximum number of binding sites of phenol

molecules per ethylene oxide unit in micelles at 25°C is 0.19. Using this value, and with the assumption the value should be the same for admicelles, the expected adsolubilized phenol molecules are 1.14 per each $C_{12}E_6$ molecule, in reasonable agreement with our data at 1.88g/L phenol which indicates 1.3 phenol molecules adsolubilize per each $C_{12}E_6$.

Another question that should be explored is why toluene showed evidence of competitive adsorption for $C_{12}E_6$ and not for CTAB. This different behavior is probably due to the fact that $C_{12}E_6$ and CTAB surfactants adsorb preferentially on different surface sites. Toluene seems to compete for those sites that are favorable to $C_{12}E_6$ adsorption, and less so for those favorable for CTAB adsorption. Further, why was the amount adsorbed for CTAB from the 1.88 g/L phenol solution above the cmc less than that adsorbed from the 0.47 g/L phenol solution? It is likely that at this large concentration phenol manages to substitute for some of the CTAB surfactant molecules in the admicelles. The same phenomenon does not happen in the case of $C_{12}E_6$ because not much phenol adsolubilizes within those admicelles.

It remains to be discussed how changes in density and viscosity of the various solutions upon dissolution of surfactant affects the estimated adsorbed amounts. As pointed out by many authors,[223, 224] the viscosity changes almost imperceptibly in the surfactant concentration range considered in the present work. The viscosity increases as surfactant is added, and then decreases steeply at the cmc at which point the viscosity increases with added surfactant once again. Above the cmc, a hard sphere model [i.e., the relative viscosity=1+2.5·(volume fraction of micelles)] provides a reasonable estimate for the solution viscosity. Under this approximation, the highest

viscosity in the systems considered herein would occur at 1.5 cmc, with a micelle volume fraction of ~0.2% for CTAB, and much lower for $C_{12}E_6$. Below the cmc, we could not find data for our surfactants (these measurements are extremely difficult because of the very small changes in viscosity). Density changes due to surfactants dissolution are estimated in approximately 0.5% at most. Assuming that both solution viscosity and solution density change by ~0.5% each, the estimated difference between the actual amount adsorbed and that estimated from the Kanazawa equation becomes negligible when compared to the experimental errors typical of our measurements.

Table 7-2 Low-molecular-weight co-solute molecules adsorbed per adsorbed surfactant molecule at cmc. *These values are believed not to be statistically relevant (i.e., they should be ~0).

	0.47g/L Toluene	*0.47g/L 1-hexanol*	*0.47g/L Phenol*	*1.88g/L Phenol*
CTAB	2.7	2.6	2.9	1.6
$C_{12}E_6$	--*	1.3	0.4	1.3

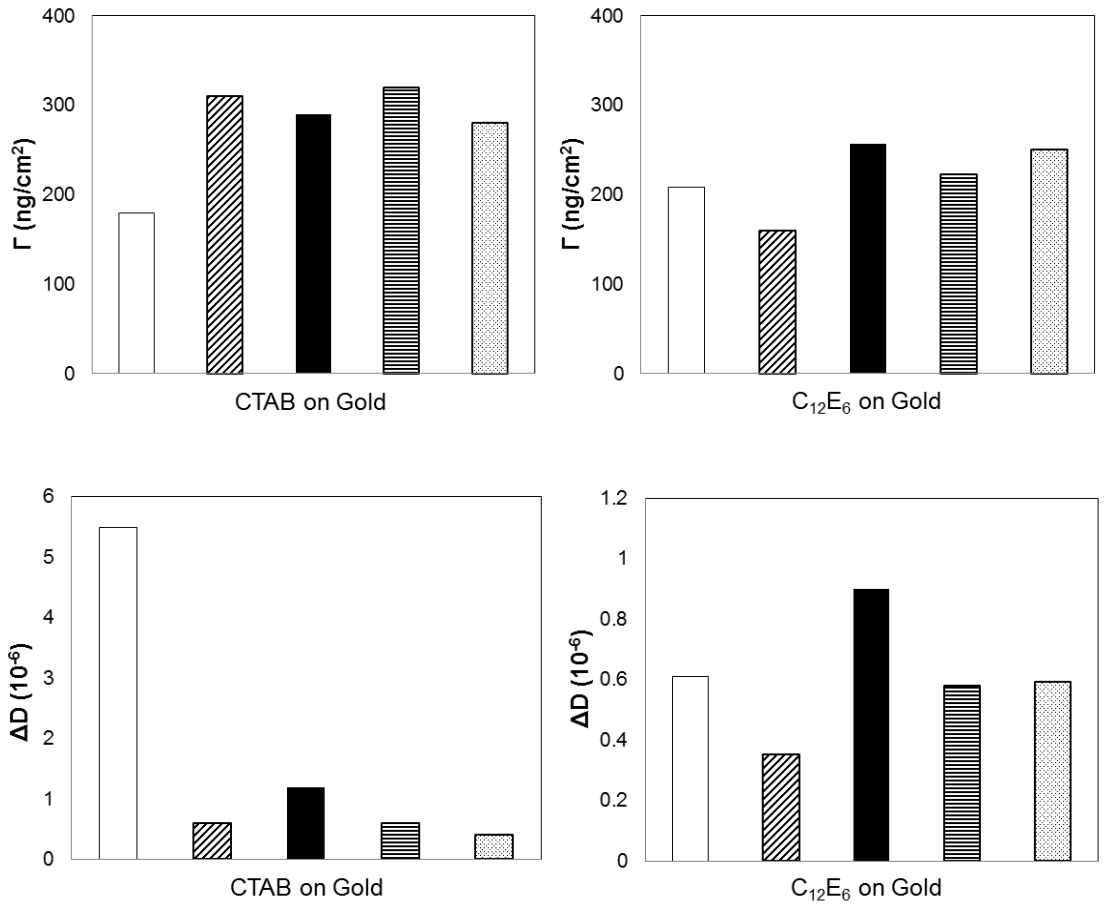

Figure 7-7 Comparison among adsorption amounts and change in dissipation factor of CTAB and $C_{12}E_6$ observed at 1.0 cmc from pure water (white), 0.47g/L toluene (right upward diagonal), 1-hexanol (black), 0.47g/L phenol (dark horizontal) and 1.88g/L phenol (dotted diamond).

A.6 Conclusion

Using a QCM-D, experimental data were measured for the adsorption of aqueous CTAB and $C_{12}E_6$ surfactants on hydrophilic gold surfaces in the presence of the low-molecular-weight co-solutes toluene, 1-hexanol, and phenol. In the case of CTAB a significant increase in the adsorbed mass was observed compared to that measured from

pure water for all the co-solutes considered. In the case of $C_{12}E_6$ our data show little changes compared to those obtained from pure water, except when toluene is present, in which case competitive adsorption is observed. This data suggests that CTAB admicelles change from cylindrical to flat bilayers in the presence of co-solutes, and likely cover larger portions of the surface. On the contrary, $C_{12}E_6$ admicelles do not show any significant morphological change due to the presence of co-solutes. Experimental values for the dissipation factor further strengthen the hypothesis that CTAB yields cylindrical admicelles while $C_{12}E_6$ yields flat monolayers. Our interpretation is consistent with AFM data reported by others on various substrates, and are beneficial for the improvement of admicellar polymerization techniques in which one of the critical steps is the solubilization of monomers within surfactant admicelles.

Appendix B: $C_{12}E_6$ and SDS Surfactants Simulated at the Vacuum-Water Interface

The material presented below was published in 2010 in volume 8, issue 26, of the journal 'Langmuir'.

B.1 Abstract

The effect of surface coverage on the aggregate structure for the nonionic hexaethylene glycol monododecyl ether ($C_{12}E_6$) and anionic sodium dodecyl sulfate (SDS) surfactants at vacuum-water interface has been studied using molecular dynamics simulations. We report the aggregate morphologies and various structural details of both surfactants as a function of surface coverage. Our results indicate that $C_{12}E_6$ tail groups orient less perpendicularly to the vacuum-water interface compared to SDS ones. Interfacial $C_{12}E_6$ shows a transition from gas-like to liquid-like phases as the surface density increases. However, even at the largest coverage considered, interfacial $C_{12}E_6$ aggregates show more disordered structures compared to SDS ones. Both surfactants exhibit a non-monotonic change in the planar mobility as the available surface area per molecule varies. The results are interpreted on the basis of the molecular features of both surfactants, with particular emphasis on the properties of the surfactant heads, which is nonionic, long, and flexible for $C_{12}E_6$, as opposed to ionic, compact, and rigid for SDS.

B.2 Introduction

The surfactant behavior at interfaces plays an important role in many applications, including detergency, mineral flotation, corrosion inhibition, solid dispersion, oil recovery, nanoparticle dispersion, etc.[165] All these applications continue to motivate efforts towards describing surfactant aggregates and surfactant monolayers at various interfaces.[169, 170, 176, 189, 211, 225-227] Surfactant adsorption properties depend on the balance between hydrophilic and hydrophobic forces, which in turn are governed by the ratio between the properties of tail and head groups. Thus it is important to understand the influence of the head groups' features on the aggregation properties of surfactants not only for molecular-based understanding of the observed phenomena, but also to design surfactants for specific applications, such as the stabilization of carbon nanotube dispersions.[225, 227-230] Molecular simulations are ideal for these purposes because each molecular parameter can be changed at will.

In this work we compare the behavior of hexaethylene glycol monododecyl ether ($C_{12}E_6$) and sodium dodecyl sulfate (SDS) at vacuum-water interfaces. $C_{12}E_6$ belongs to the family of alkylpolyethylene glycol ethers, known as C_mE_n.[231] These surfactants have chemical formula $C_mH_{2m+1}(OC_2H_4)_nOH$, with a nonpolar hydrocarbon tail group C_mH_{2m+1} (C_m) and a polar nonionic and long hydrophilic head group $(OC_2H_4)_nOH$ (E_n). C_mE_n is atoxic and widely used for detergency, cosmetics and pharmaceutical formulations. The other surfactant employed in this work is the anionic SDS. The tail groups of SDS and $C_{12}E_6$ are identical. As opposed to the long nonionic head group of

$C_{12}E_6$, in SDS the head group consists of one anionic sulfate group. The counter-ion is sodium.

A number of experiments have been conducted to study C_mE_n surfactants at solid-liquid interfaces.[113, 183, 184, 232, 233] Grant et al.[184] reported that on graphite $C_{14}E_6$ forms rod-like structures while $C_{10}E_6$ forms flat layers; on an organic hydrophilic surface both surfactants form flat layers. Our group[113, 189] has studied adsorption isotherms of $C_{12}E_6$ on hydrophilic gold surfaces using the quartz crystal microbalance. The results suggest the formation of monolayer-like structures. Less is known about the structure of C_mE_n surfactants at air-liquid interfaces. Among the few experimental results available, Thomas and co-workers[234-238] successfully employed neutron reflection to assess the structure of adsorbed $C_{12}E_n$ aggregates at the air-water interface in a wide concentration range, from dilute conditions to the critical micelle concentration (cmc). The experiments were performed on surfactants with different number of ethylene oxide groups, from n=1 to n=12 ("E_n"). It was observed that the extent of overlap between the alkyl chain and ethylene group increases as n increases, the surfactant layers are molecularly rough, and that both alkyl and glycol groups are tilted at the interfaces. Thomas and co-workers also studied the interfacial properties of SDS at interfaces using neutron reflection.[239-243] At the air-water interface it has been reported that the SDS tail groups are oriented less perpendicularly to the interface than dodecanol tail groups, and also that the thickness of interfacial dodecanol layer is larger than that of SDS.[240]

Of particular importance in surfactant studies is the concept of surface tension, γ. The γ-A, or π-A, isotherm diagram, in which the surface pressure π is a function of the

surface area per head group, A, represents the phase diagram for the self-assembled surfactant aggregates. Several phases are typically observed, including dilute gas-like (G), liquid-like (L), liquid-condensed (LC) and solid-like (S) phases. The various phases are characterized by different morphologies of the two-dimensional fluid, which strongly affects the surface tension.[244]

Lu et al.[235, 236] conducted a number of experiments, correlating the surface tension at the air-water interface to the C_mE_n concentration, from infinite dilution to the cmc. SDS, as any other surfactant, reduces the surface tension at air-water interfaces as its concentration increases.[245, 246] Strangely, however, it has been noticed that SDS solutions reach the minimum surface tension at concentrations larger than the cmc.[242, 247-249] Several molecular dynamics (MD) simulation studies have assessed the properties of surfactants at various interfaces.[250-256] Cuny et al.[257, 258] investigated the structural and dynamic properties of $C_{12}E_5$ aggregates at air-water interfaces. They reported that both polar glycol head groups and alkyl chains are mobile and exhibit tilted orientations, consistent with neutron reflection experiments.[235] Chanda and Bandyopadhyay simulated complete monolayers of $C_{12}E_2$[259] and $C_{12}E_{6[260]}$ at air-water interfaces for 3 and 5.5 ns, respectively. They found that the longer polar glycol surfactants head groups are more tilted towards the aqueous phase than the shorter ones, because of hydrogen-bonded structures formed between water molecules and oxygen atoms of the head groups. SDS at air-water and water-CCl_4 interfaces has been studied using molecular dynamics by Berkowitz and coworkers.[245, 261] MD simulations are also capable of predicting surface tension.[262-265] Baoukina et al.[266] and Laing et al.[267] conducted large scale and

long time MD simulations to study π-A isotherms of dipalmitoyl-phosphatidylcholine lipid monolayers, obtaining comparable results with experiments. To the best of our knowledge, no MD simulation result has been reported for the surface tension of $C_{12}E_6$ at the air-water interface.

In this work we employ MD simulations to study $C_{12}E_6$ and SDS surfactants at vacuum-water interfaces for a large range of interface coverages (surface area per molecule). The results, in general agreement with experiments, are discussed in terms of morphological and dynamical properties, as well as of surface tension. Differences between the results obtained for $C_{12}E_6$ and those for SDS are interpreted based on the atomic-scale properties of the surfactants head groups.

B.2 Simulation Methodology

MD simulations were performed at the vacuum-water interface. Water molecules were modeled using the extended simple point charge (SPC/E) potential.[268] Bond lengths and angles were maintained fixed using the SETTLE algorithm.[269] The nonionic $C_{12}E_6$ surfactant contains one hydrophobic tail (T) of 12 alkyl groups, and one hydrophilic head (H) of 6 ethylene oxide (EO) moieties and 1 terminal OH group (see Figure 7-8). The alkyl groups were modeled as united atoms, whereas the oxygen atoms in the EO groups as well as oxygen and hydrogen atoms in the terminal OH groups were modeled explicitly. The tail alkyl groups were modeled by the TRaPPE-UA force field.[270] The oxyethylene groups were modeled implementing the OPLS force field.[271, 272] Following Berkowitz,[261] we allowed bonds and angles to oscillate

from their equilibrium values, thus modifying the original TRaPPE-UA and OPLS recipes.

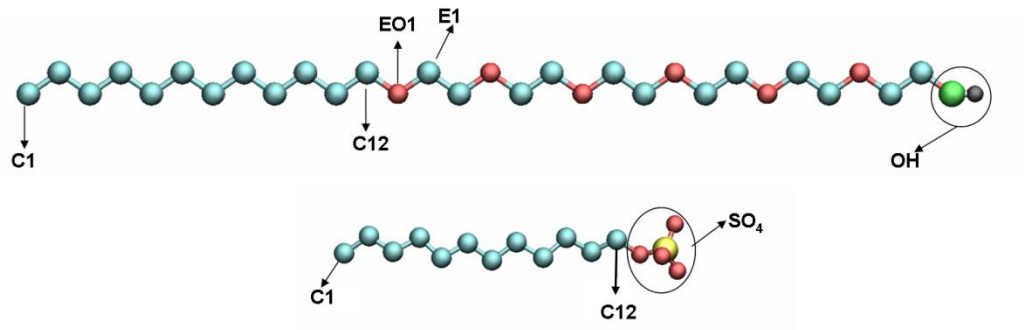

Figure 7-8 Schematic representations of $C_{12}E_6$ (top) and SDS (bottom) surfactants according to the ball-and-stick formalism. Top: C1 represents the 1st alkyl group in the tail, C12 is the 12th alkyl group in tail, EO1 is the oxygen in the 1st ethylene glycol group, E1 is the ethylene in the first ethylene glycol group, and OH is the terminal OH group. Bottom: SDS has the same number of alkyl groups in its tails $C_{12}E_6$ does, but its head group is composed by one sulfur and four oxygen atoms. Color code: the alkyl groups in SDS and $C_{12}E_6$ and ethylene groups in $C_{12}E_6$ are represented as cyan spheres; the oxygen atoms in the ethylene oxide chain of $C_{12}E_6$ and in the sulfate group of SDS are represented as red spheres; the sulfur atom in SDS is a yellow sphere; the oxygen and hydrogen atoms of the terminal OH group in $C_{12}E_6$ are green and black spheres, respectively.

Harmonic potentials were used to model bond stretching:

$$E_{bond} = K_b (r - r_O)^2 \quad . \tag{7-3}$$

In Eq. (7-3), K_b is the elastic constant, r is the instantaneous distance between the bonded atoms, and r_O is the equilibrium distance between them.

The harmonic potential was used to model angle bending potentials:

$$E_{ang} = K_\theta (\theta - \theta_O)^2 \quad . \tag{7-4}$$

In Eq. (7-4), E_{ang} is the bending energy, K_θ is the force constant, θ_O and θ are the equilibrium and the instantaneous angles, respectively. The force constants in the harmonic bond stretching and angle bending potentials were borrowed from Ref.

[[261]]. The bond lengths and angles involving the terminal OH group in $C_{12}E_6$ surfactants were held fixed by the LINCS algorithm.[273]

Following the Ryckaert-Bellemans (RB)[274] dihedral implementation, dihedral angles in the tail groups and the terminal OH group were constrained according to:

$$E_{dihedral} = \sum_{k=0}^{3} c_k \cos^k(\phi) \ . \tag{7-5}$$

The dihedral angles involving oxyethylene group were constrained using harmonic potentials:

$$E_{dihedral} = K_\phi(1+\cos(n\phi - \phi_s)) \quad . \tag{7-6}$$

In Eq. (7-6) n is an integer, ϕ_s is the equilibrium dihedral angle. All the force field parameters employed in our simulations are described in Table 7-4.

The force field implemented for SDS is described in our previous article.[211]

The GROMACS [275-277] MD simulation package was used to integrate the equations of motion using the leap-frog algorithm[278] with a time step of 2 fs. All simulations were conducted in the canonical ensemble in which the number of particles (N), the box volume (V) and the temperature (T) were kept constant. T was maintained constant using the Nose-Hoover thermostat with a relaxation time of 100 fs. All simulations were conducted at T=300 K. Dispersive forces were computed using the Lennard-Jones potential with an inner cutoff of 0.8 nm and outer cutoff of 1.0 nm. Long range electrostatic interactions were treated using the Particle Mesh Ewald (PME) method.[279] Periodic boundary conditions were employed in all three dimensions. 15,000 water molecules were inserted in a simulation box of size 10.08x9.60x30.00 (see Figure 7-9). All simulations were carried out for 32 ns. Equilibration was considered completed when no change was observed in the calculated density profiles within a 2 ns

interval. We found that 30 ns of simulation were necessary to equilibrate the system at the largest surfactant concentrations considered, although shorter runs were sufficient for systems at low surfactant concentration. For consistency, the production run consisted in the last 2ns of each simulation, although we used the last 10ns of simulations to calculate the mean square displacement for the simulated surfactants. During production, the positions of the surfactant atoms were stored every 2 ps and used for all subsequent calculations.

Table 7-3 Parameters used to implement the force fields in Eqs. (7-3, 4, 5 and 6).

Lennard-Jones and Electrostatic Interaction Potential Parameters

ATOMS (or GROUPS)	σ (Angstrom)	ε (Kcal mole^{-1})	*q (e)*
CH_3	3.905	0.175000	0.0000
CH_2	3.905	0.118000	0.0000
CH_2 (in -O-CH_2- CH_2-)	3.905	0.118000	0.2500
CH_2 (in -CH_2-O-H)	3.905	0.118000	0.2650
O (in -O-CH_2- CH_2-)	3.000	0.170000	-0.5000
O (in -OH)	3.070	0.170000	-0.7000
H (in -OH)	0.000	0.000000	0.4350
H (in H_2O)	0.000	0.000000	0.4238
O (in H_2O)	3.166	0.155402	-0.8476

Bond Stretching Potential Parameters Bond

Bond	K_b (kcal mol^{-1} $Å^{-2}$)	r_o (Angstroms)
CH_3-CH_2	620.000	1.540
CH_2-CH_2	620.000	1.540
CH_2-O	600.000	1.410
CH_2-O (in CH_2-O-H)	900.000	1.430
O-H	N/A	0.945

Angle Bending Potential Parameters

ANGLE	K_θ(kcal mol^{-1} rad^{-2})	Θ_O(deg)
CH_3-CH_2-CH_2	124.190	114.000
CH_2-CH_2-CH_2	124.190	114.000
CH_2-CH_2-O	124.190	112.000
CH_2-O-CH_2	124.190	112.000
CH_2-CH_2-O (O in OH)	124.190	108.000
CH_2-O-H	N/A	108.500

Bond Torsion Potential Parameters

DIHEDRAL	K (Kj mol^{-1})	n	φ	
O-CH_2-CH_2-O	4.184	3	0.0	
CH_2-CH_2-O-CH_2	3.138	3	0.0	
DIHEDRAL	C_1(Kj mol^{-1})	C_2	C_3	C_4
CHn-CH2-CH2-CH2	8.3970	16.7854	1.1339	-26.3160
CH2-CH2-O-H	2.8220	2.9430	0.1160	-6.25090

We report in Figure 7-9 one representative simulation snapshot. We conducted a number of simulations with varying number of surfactants on the two interfaces. The surface coverages of surfactants are randomly chosen from infinite dilution to the concentration necessary to form a monolayer. The thickness of the water film is large enough to prevent undesired interactions between surfactant molecules adsorbed in the opposing vacuum-water interfaces from occurring. The surface areas per $C_{12}E_6$ molecules considered are: 9684, 1936, 691, 358, 293, 179, 136, 115, 92, 77, 64, and 52 $Å^2$ per surfactant. 52 $Å^2$ per surfactant corresponds to full coverage.[219] We performed simulations for SDS at 4 surface coverages (~700, 196, 96 and 52 $Å^2$ per surfactant). The full SDS coverage corresponds to ~40-45 $Å^2$ per surfactant, conditions simulated previously by Schweighofer et al.[261]

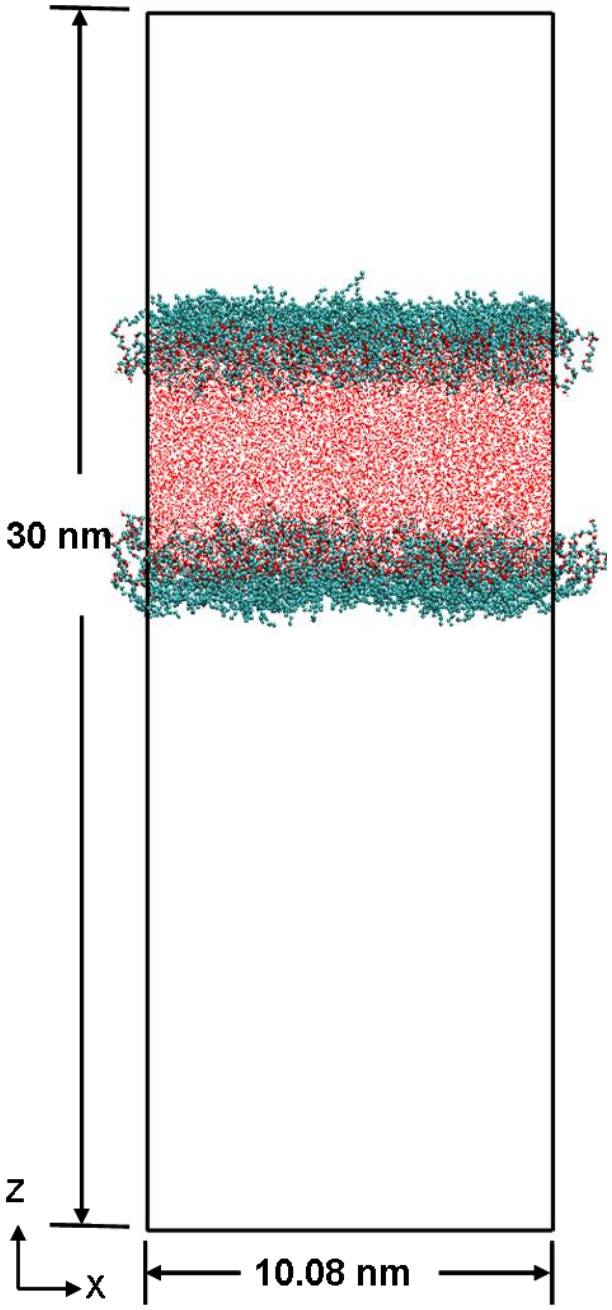

Figure 7-9 Schematic representation of the simulation box. The color code is the same as in Figure 7-8. Additionally, the red dots between the two surfactant layers represent water in the wireframe formalism.

B.4 Results and Discussions

B.4.1 Density Profiles

We provide the number density profiles of entire $C_{12}E_6$ chains (E), heads (H) and tails (T) as a function of the distance along the z direction in Figure 7-10. The density profiles for the entire surfactants (E) correspond to the density profiles of the surfactants center of mass. The density profiles for heads (H) and tails (T) are instead the density distributions of head and tail segments, respectively. The z=0 position corresponds to the center of mass of the simulated systems.

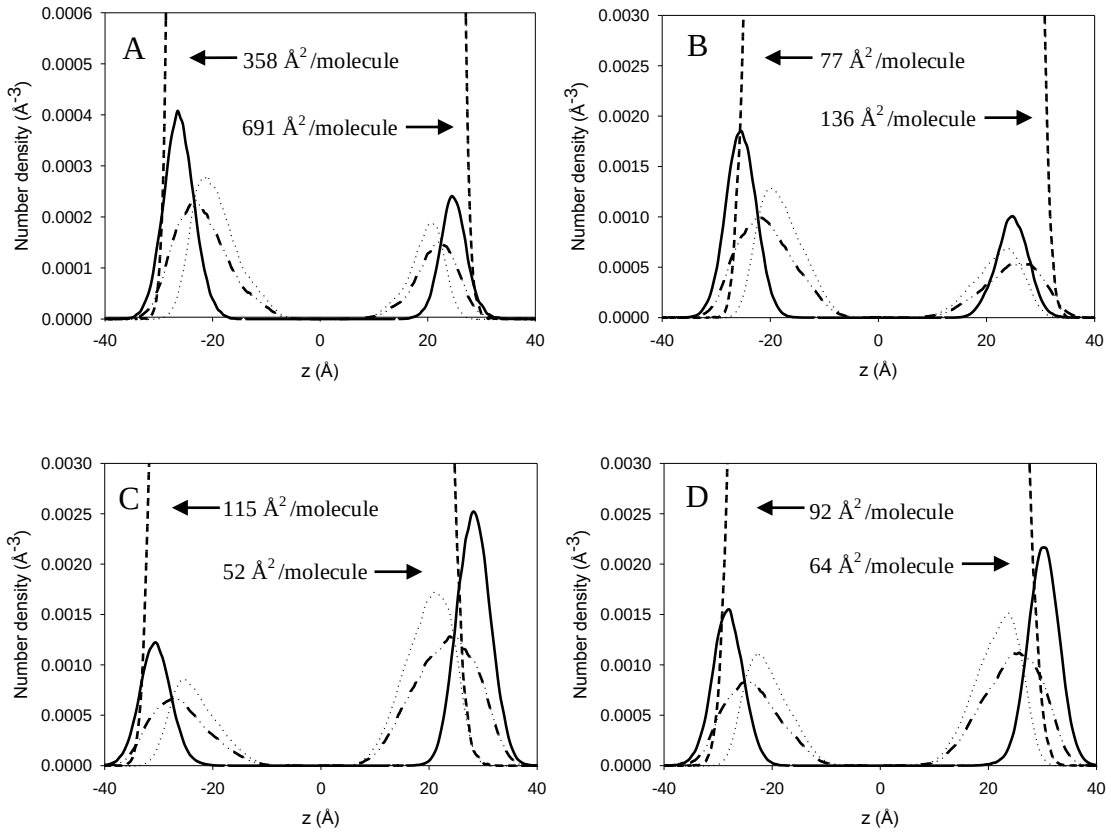

Figure 7-10 Number density profiles perpendicular to the vacuum-water interface at equilibrium for representative systems at different surface coverage: water (dashed line); tails (solid line); heads (dot line); and entire $C_{12}E_6$ surfactants (dot-dot-dash line). The water number density reaches ~ 0.033 Å^{-3} in the center of each system considered (not shown).

For brevity, only the number density profiles obtained from 4 systems (8 interfaces) are shown. It is clear that the surfactant molecules accumulate at both vacuum-water interfaces with the head groups at contact with the water phase and the tail groups away from it. The intensity of the peaks increases as the surface area per molecule decreases (the interface coverage increases). At high surface area per surfactant (691 Å^2/molecule) some alkyl groups of the surfactant tails remain at contact

with the water phase (right part of panel A), which is due to the low surface coverage considered. At low surface area per head group (52 $Å^2$/molecule) the tail groups are found away from the water phase, towards the gas phase (right part of panel C). The atomic number density for water reaches about 0.033 $Å^{-3}$ in the center of the simulation box (not shown), consistent with the density of bulk liquid water at ambient conditions.

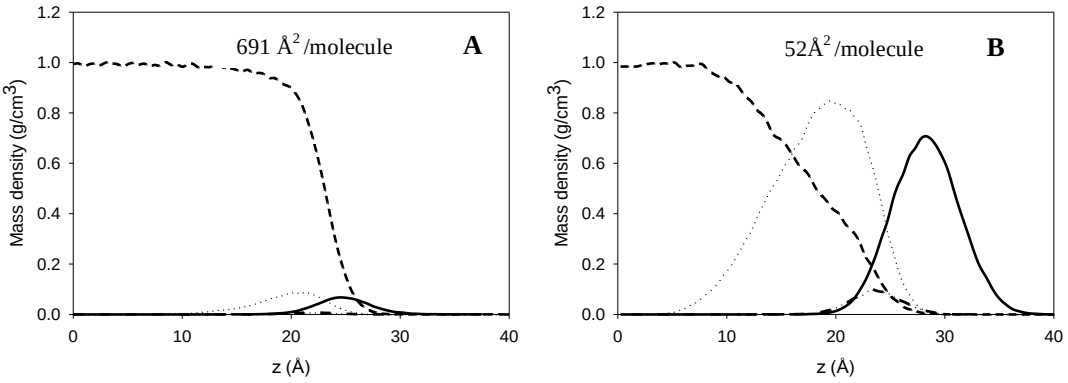

Figure 7-11 Mass density profiles for $C_{12}E_6$ at 691 $Å^2$/molecule (panel A) and 52 $Å^2$/molecule (panel B). Results are for water (dashed line); tails (solid line); heads (dot line); and EO1 groups (dot-dot-dash line).

Because of the large size difference of water molecules compared to $C_{12}E_6$ surfactants, we calculated the mass density profiles of $C_{12}E_6$ at 691 $Å^2$/molecule and 52 $Å^2$/molecule to obtain a better visualization of the interfacial behavior. The results are shown in Figure 7-11. At low surface coverage (691 $Å^2$/molecule, panel A), the surfactant tail groups are close to the water phase. At high surface coverage (52 $Å^2$/molecule, panel B), not only the majority of tail groups are out of the water phase, but even part of the head groups are pulled away from water, towards the hydrophobic vacuum. We point out that at high surface coverage (panel B) the mass density profile for water decreases from the bulk value to zero smoothly, but the curve shows a small, yet noticeable change in inflection within the surfactant layers, probably because of

surfactant head-water excluded-volume effects. In Figure 7-11 we also report the density profile observed for the EO1 group (see Figure 7-8 for details). This group roughly identifies the molecular mid-point for the $C_{12}E_6$ surfactant. Our results show that when the surfactant surface concentration is 52 $Å^2$/molecule the EO1 group is located in between the interfacial layers formed by the head and the tail groups. At lower surface concentration, e.g., 691 $Å^2$/molecule, the EO1 group position fluctuates significantly along the z direction. This is because the surfactant molecules possess more degrees of freedom at low surface coverage. Some simulation snapshots collected at low surfactant concentration even show configurations in which some surfactants form hairpin-type turns. To visualize these results, representative simulation snapshots for $C_{12}E_6$ surfactants at the vacuum-water interface at 691 $Å^2$/molecule and 52 $Å^2$/molecule are shown in Figure 7-12 (center and bottom panels, respectively). At high surface coverage the tail groups of $C_{12}E_6$ effectively pull away the long, partially hydrophobic $C_{12}E_6$ head groups from the water phase. Simultaneously, as can be seen from the bottom panel in Figure 7-12, packing of the long $C_{12}E_6$ head groups squeezes water away from the surfactant heads (i.e., because more surfactant head groups are present, less room is available for interfacial water). At 1936 $Å^2$/molecule (top panel in Figure 7-12) we highlight the formation of hairpin turns by the $C_{12}E_6$ surfactant. For clarity, only 2 of the total 5 $C_{12}E_6$ surfactants present at the interface are shown in the top panel.

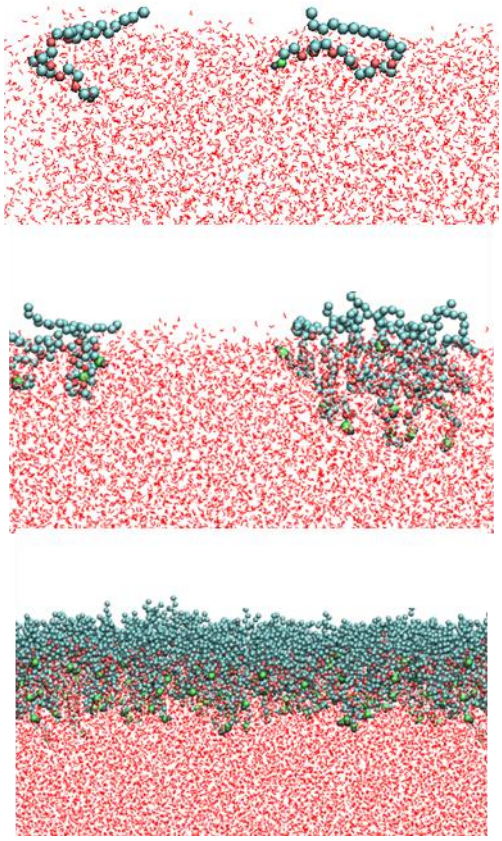

Figure 7-12 Representative simulation snapshots for $C_{12}E_6$ at vacuum-water interface. The top panel shows hairpin-type surfactants observed at 1936$Å^2$/molecule, the center panel is for 691$Å^2$/molecule, and the bottom panel for 52$Å^2$/molecule.

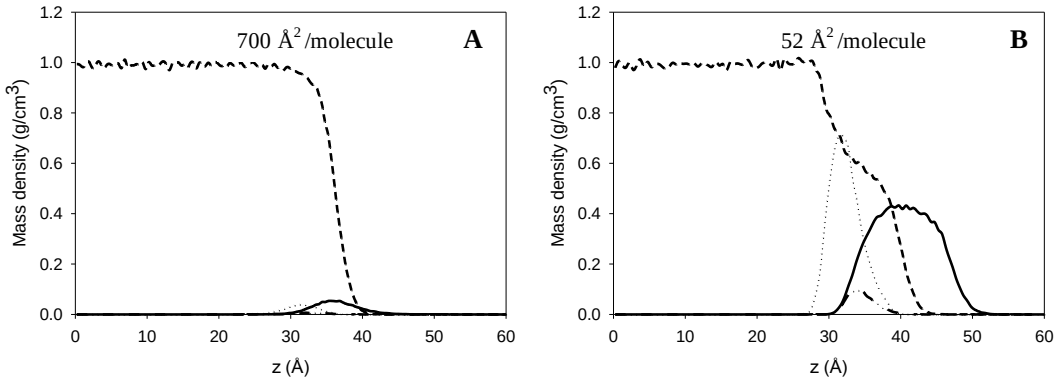

Figure 7-13 Mass density profiles for SDS at 700 Å^2/molecule (panel A) and 52 Å^2/molecule (panel B). Data are shown for water (dashed line); tails (solid line); heads (dot line); and C12 groups (dot-dot-dash line).

For comparison, we calculated the mass density profiles for SDS surfactants at 700 Å^2/molecule and 52 Å^2/molecule. The results are shown in Figure 7-13. At high surface area per molecule the results are qualitatively similar to those observed for $C_{12}E_6$. At low surface area per head group, contrary to that observed for $C_{12}E_6$, the SDS head groups are fully immersed in water and only the surfactant tail groups move away from the water phase. This observation denotes the different hydration properties between the head groups of $C_{12}E_6$ and SDS. The sulfate groups of SDS heads have strong hydration due to electrostatic interactions. The $C_{12}E_6$ head contains both hydrophilic (oxygenated groups) and hydrophobic (ethylene groups) parts. When the $C_{12}E_6$ molecules pack together to form a monolayer, the ethylene groups in the center of the surfactants may repel water molecules, and consequently water molecules are squeezed out of the interfacial region. The different features between $C_{12}E_6$ and SDS head groups result in a different water density profile, which decreases rather gradually

from liquid-like to zero across the interface in the case of $C_{12}E_6$, and more abruptly in the case of SDS. In Figure 7-13 we also report the density profile for the C12 group (see Figure 7-8 for details). As in the case of the group EO1 for $C_{12}E_6$ (see Figure 7-11), the position of the C12 group helps us identify where the SDS head and tail groups meet. Consistent with our previous data for $C_{12}E_6$, the density profiles for the C12 group peak in the region between the interfacial layers formed by SDS head and tail groups. More interestingly, the position of the C12 group corresponds to a significant change in inflexion in the water density profile, suggesting that this unexpected feature of the water density is due to excluded-volume effects near the SDS head groups. To compare SDS vs. $C_{12}E_6$ surfactants, in Figure 7-14 we provide representative simulation snapshots for SDS surfactants self-assembled at the vacuum-water interface. Because the head group of SDS is shorter and over-all less flexible than that of $C_{12}E_6$, no hairpin-type configuration is observed for the former even at low surfactant concentration.

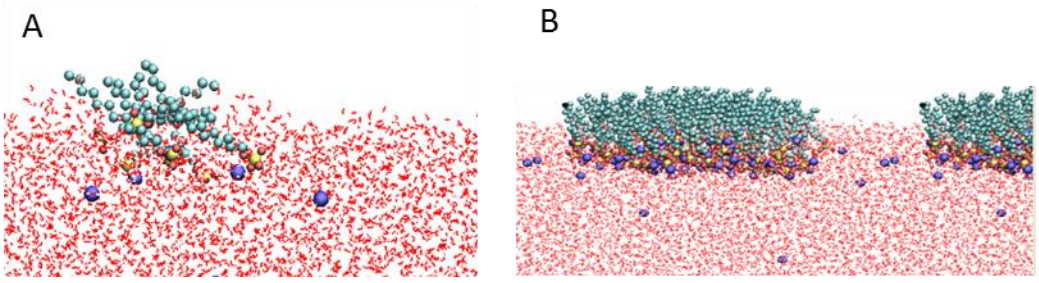

Figure 7-14 Representative simulation snapshots for SDS at vacuum-water interface. Panel A is for 700 $Å^2$/molecule; panel B is for 52$Å^2$/molecule.

In all cases considered, for both $C_{12}E_6$ and SDS, our results show that the density profiles for tail groups overlap those of head groups, reflecting the lack of complete segregation between heads and tails. The reason for this behavior was found to be the fluctuation of surfactants along the direction perpendicular to the interface. These fluctuations occur at all conditions considered because of thermal motion. This observation is consistent with recent quantifications on the density fluctuations for water at hydrophobic interfaces.[280, 281] Such density fluctuations become even more pronounced at vapor-liquid interfaces. Structural fluctuations for micelles of C_8E_5 surfactants in water have been observed by Garde et al., who reported that such fluctuations are so pronounced that they lead the C_8E_5 tail group to frequently come in contact with the head groups, and sometimes even with water molecules.[282]

In Figure 7-15 we compare representative simulation snapshots obtained for $C_{12}E_6$ (panel A) and SDS (panel B) at the largest coverage simulated here (52 $Å^2$/molecule in both cases). Note that at this surface coverage $C_{12}E_6$ yields a complete monolayer while SDS forms a monolayer at 40-45 $Å^2$/molecule, a situation studied by Schweighofer et al.[261] For clarity, only parts of the surfactant head groups are shown. In the case of $C_{12}E_6$, we only show EO1 and E1 groups (see Figure 7-8 for details), in the case of SDS the entire head groups are shown. The results highlight the staggering of surfactant head groups along the direction perpendicular to the interface. The staggering of head groups along the direction perpendicular to the interface occurs within a region of ~ 1 nm for $C_{12}E_6$, and of ~0.5 nm in the case of SDS. The reason for the wider staggering amplitude in the case of $C_{12}E_6$ is related to the chemical nature of its head groups. For example, the E1 group, which is located between the tail and the head (see Figure 7-8

for details, and Figure 7-11 for the density distribution results), can interact with any hydrophobic ethylene groups in either the surfactant head or the surfactant tail. On the contrary, the SDS head group is composed by only one sulfate group, and it can only associate favorably with other sulfates. Also of importance is the flexibility and length of the $C_{12}E_6$ head groups as opposed to the compactness and rigidity of SDS heads. Because of their flexibility, the $C_{12}E_6$ head groups can rearrange easily at the vacuum-water interface, while the SDS ones cannot. This different aggregate packing at the interface is probably responsible for the different propensity of the two surfactants to lower the surface tension.

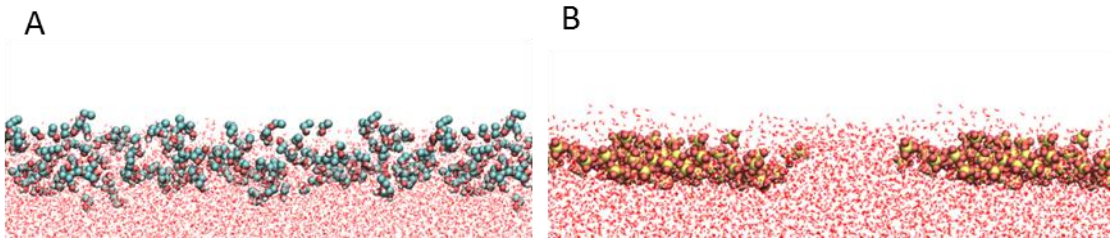

Figure 7-15 Expanded side view of representative simulation snapshots that highlight the surfactant head groups at vacuum-water interface. Results are for EO1 and E1 of $C_{12}E_6$ surfactants in panel A; sulfate groups of SDS surfactants in panel B.

In order to quantify the characteristics of the interfacial structure, we fit the density profiles of entire $C_{12}E_6$ chains (E), head groups (H), and tail groups (T) to Gaussian functions:[283]

$$\rho(z) = n^0 \exp\left[\frac{-4\ln 2(z - z^0)^2}{\sigma^2}\right]. \qquad (7\text{-}7)$$

In Eq. (7-7) n^0, σ and z^0 are the distribution height, distribution width at half-height, and peak position, respectively. The presence of a small asymmetry in the

density profiles introduces a bias in fitting the curves to a single Gaussian function, which we consider not relevant for our analysis. The values of σ_E, σ_H, and σ_T as a function of surface area per surfactant head group are reported in Figure 7-16. As the distribution width increases, the surfactants yield a thicker layer at the vacuum-water interface. The results show that all values for σ decrease as the surface area per surfactant increases. However, particularly in the case of σ_E, the thickness of the entire surfactant layer and therefore the most important of the results shown in Figure 7-16, the change is not monotonic and the curve can be divided into 3 regions with decreasing surface area per head group. In region I, the value of σ increases almost linearly from an infinite dilute interface coverage to ~293 $Å^2$ / $C_{12}E_6$ molecule. In Region Π, from ~293 $Å^2$ / molecule to ~77 $Å^2$ / molecule, the value of σ remains ~ constant. In region III, when the surface area per head group is lower than ~77$Å^2$/molecule, we observe a significant increase of σ as the surface area per molecule decreases (this is particularly evident when data for σ_E are considered). We relate this observation to the classic π-A isotherm.[244] Region I corresponds to the "gas-like" (G) phase, where the available area per molecule is large compared to the dimensions of the surfactant. Region III, in which the surface is almost completely covered by $C_{12}E_6$, corresponds to L, LC or S phases. Based on the distribution of $C_{12}E_6$ observed in our snapshots (Figure 7-12 and Figure 7-15), we argue that region III corresponds to a liquid-like phase for $C_{12}E_6$ surfactants. Between regions I and III, the plateau region observed in Figure 7-16 indicates a liquid-gas phase transition. Unfortunately, we did not collect sufficient data to provide the entire σ-A phase diagram for SDS.

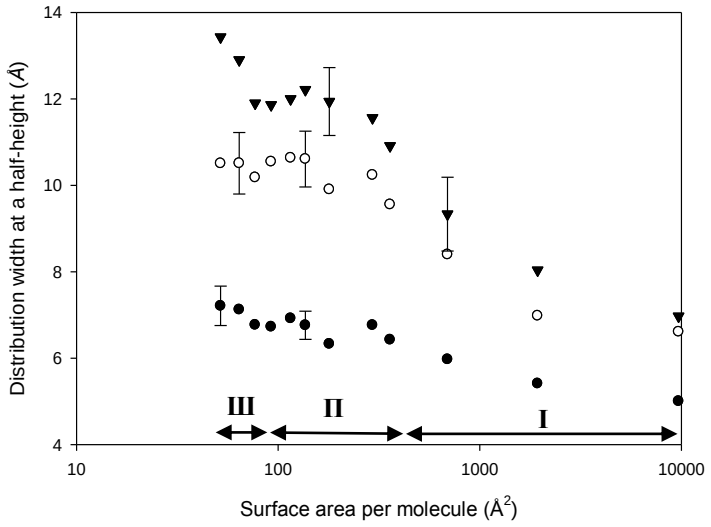

Figure 7-16 Values of the distribution widths at half-height as a function of surface area per molecule. Results shown are for the entire surfactant layer, σ_E, the head groups, σ_H, and the tail groups, σ_T. Symbols ▼, ○, and ● are for σ_E, σ_H, and σ_T, respectively.

The thickness of the self-assembled surfactant structure at the largest surface coverage considered is comparable to those obtained from neutron reflection experiments. At 55 $Å^2$ per surfactant the experimental data for the width of the surface aggregate reported by Lu et al. is 13.5 ±1 Å, which is close to the value of 13.4±0.9 Å found in our simulation for the system with 52 $Å^2$/molecule.[236, 237] Good agreement between experiments and simulations is also found for the thickness of head and tail layers, as summarized in Table 7-4 (note that the thicknesses reported in Table 7-4 are twice the widths reported in Figure 7-16). Analyzing the results we notice that the sum of the head and tail thicknesses is greater than the thickness of the layer formed by $C_{12}E_6$, which is also in agreement with the experimental data of Lu et al.[236, 237, 284] This is due to the extensive interpenetration of head and tail layers within the surface

aggregates. The main difference between our results and experimental data comes from the thickness of the layer formed by the tail groups. The value reported in Table 7-4 was obtained by Lu et al. fitting the experimental data by a single uniform-layer model. When a Gaussian function was used to fit the experimental data, a thickness of ~16±1 Å was obtained for the layer of surfactant tails.[236] This discrepancy is due, in part, to the difficulty of interpreting uniquely the accurate experimental data. When we consider that the fully-extended length of the $C_{12}E_6$ tail group is ~16 Å and that the tails are slant at the interfaces (see below), we believe that our estimates of ~15.2±0.9 Å for the thickness of the layer of surfactant tails is quite reasonable.

Table 7-4 Comparison of the thickness of formed by head, tail groups and full $C_{12}E_6$ surfactant obtained from our simulations as opposed to those from neutron reflection experiments.

	Experiment (Å) [236, 237]	**MD Simulation (Å)**
Entire Surfactant	26.5±2	26.8±1.8
Tails	19±1	15.2±0.9
Heads	19.5±1	21±1.6

B.4.2 Surfactant End-to-End Distance

The calculated distribution width at half-height shown in Figure 7-16 only provides information of interfacial aggregate thickness along the z direction. To obtain more detailed information, we calculated the average end-to-end distance for the surfactants (details are shown schematically in Figure 7-17).

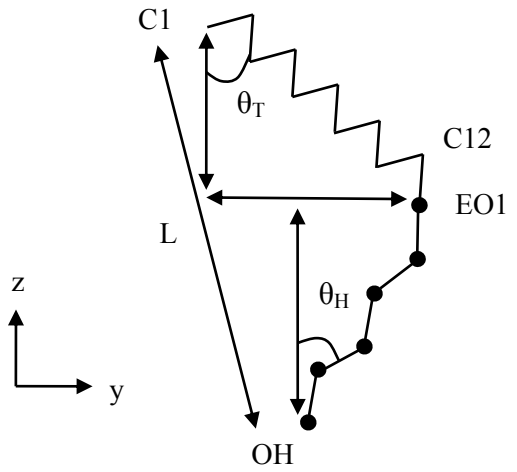

Figure 7-17 Schematic representation for a $C_{12}E_6$ surfactant at the water (bottom)-vacuum (top) interface. L is the end-to-end distance of $C_{12}E_6$ surfactant molecules; θ_T and θ_H are the tail and head tilt angles with respect to the direction z, perpendicular to the interface.

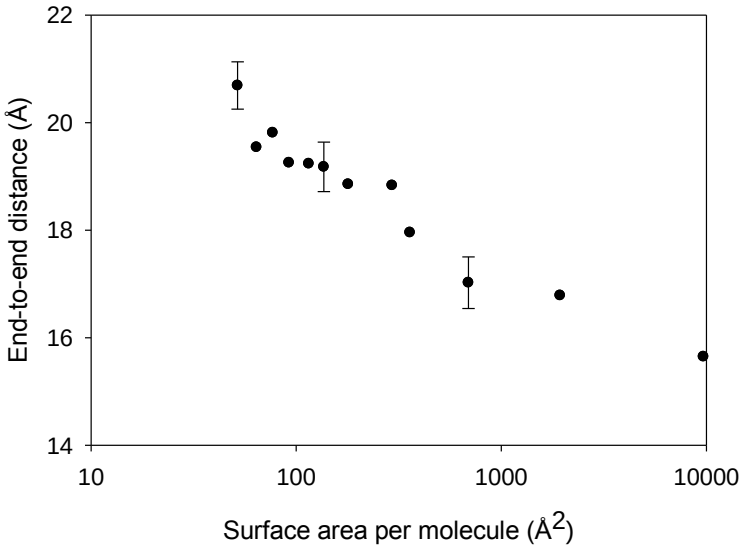

Figure 7-18 Average end-to-end distances for $C_{12}E_6$ surfactants at the vacuum-water interface as a function of the surface area per molecule. Only representative error bars are shown for clarity.

We report the average end-to-end distance of $C_{12}E_6$ molecules as a function of the surface area per molecule in Figure 7-18. The end-to-end distance increases from 15.8 Å at lowest surface coverage to 20.8Å at full monolayer coverage, i.e., the end-to-end distance increases as the surface area available for $C_{12}E_6$ decreases. The results in Figure 7-18 follow a trend similar to that observed in Figure 7-16, although the identification of liquid-like and gas-like phases is obscured by statistical uncertainty. We reiterate that, because the surfactants are staggered along the z direction, the end-to-end distance (which is an average property for the single surfactant molecules) is always shorter than the thickness of the surfactant aggregate (which is a collective property of the aggregate).

B.4.3 Surfactant Orientation at the Interface

Tilt angles for both head groups and alkyl tails (θ_H and θ_T) are defined in Figure 7-17. The values of θ_H and θ_T are between 0° and 90°. When θ is equal to 0°, the group is perpendicular to the vacuum-water interface. When θ equals to 90°, the group is parallel to the interface. The tilt angles for SDS tail groups are calculated by considering the C1 and the sulfur atom of the head group rather than the C1 and C12 groups as in the case of $C_{12}E_6$. θ_H cannot be calculated for SDS due to the geometry of its head group.

In Figure 7-19 we report the average tilt angles of head and tail groups as a function of surface area per $C_{12}E_6$ molecule. The tilt angles of both head and tail groups decrease as the surface area per $C_{12}E_6$ molecule decreases, indicating that at low surface coverage both heads and tails lie nearly parallel to the vacuum-water interface and that the head and tail groups become more perpendicular to the interface as the surface

coverage increases. The tail groups tilt angles are always larger than those of head groups, indicating that the surfactant heads are more perpendicular to the interface than the tails are. This is due to the flexibility of the hydrophilic glycol groups in water, which assume several conformations to increase the system entropy without losing favorable interactions with water. The results in Figure 7-19 show a change in slope as a function of surface coverage, which is consistent with the results of Figure 7-16. This corroborates a change in aggregation structure for the interfacial surfactants as the coverage varies. At high coverage, the average value of the tilt angle of tail groups, 54º, is slightly larger than the experimental value, 45º.[237] Cuny et al.[257] studied the monolayer structure of the nonionic surfactant $C_{12}E_5$ by simulation and found that when A=64 $Å^2$/molecule, $\theta_T \approx 63º$ and $\theta_H \approx 51º$, which is in reasonable good agreement with our results at 64 $Å^2$/molecule (θ_T = ~58º and θ_H = ~51º), when we consider that our simulations are for $C_{12}E_6$ surfactants.

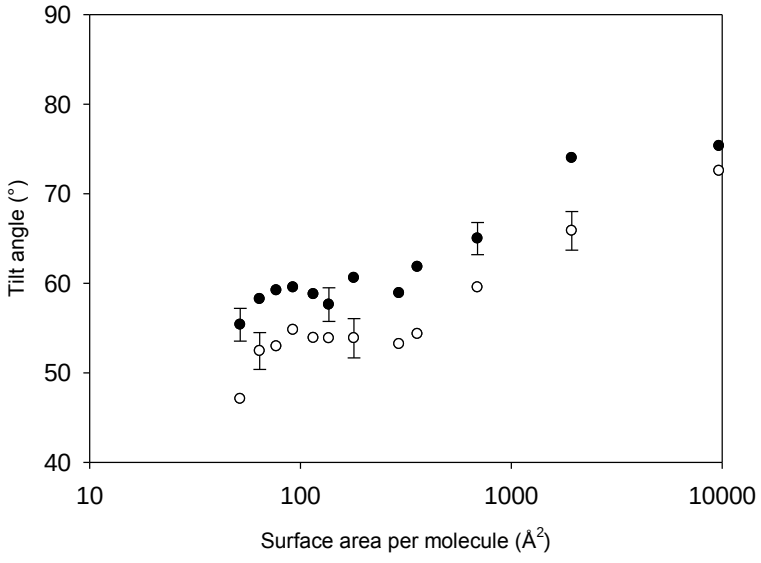

Figure 7-19 Average tilt angles for $C_{12}E_6$ tail and head groups as a function of surface area per molecule. Filled and empty circles stand for θ_T and θ_H, respectively. Only representative error bars are shown for clarity.

In Figure 7-20 we compare the simulation results for θ_T obtained for $C_{12}E_6$ to those obtained for SDS as a function of surface coverage. When the surface area available per molecule is large, the tail groups of both surfactants remain quite parallel to the interface. As the surface area per surfactant decreases, the tilt angle of SDS tail groups drops much more dramatically compared to $C_{12}E_6$ surfactants, indicating that the SDS tail groups become more quickly perpendicular to the interface than $C_{12}E_6$ ones do as the surface coverage increases. This different behavior is probably due to the different properties of the surfactant head groups, and how they interact with the aqueous film. The compact, rigid, and charged SDS head groups, because of counter-ion condensation phenomena,[211] strongly associate with each other as soon as their surface density allows them to. This aggregation forces the SDS tail groups to become perpendicular to the interface because of excluded-volume effects. On the contrary, the long, flexible, and nonionic $C_{12}E_6$ head groups easily interact with water molecules, but do not yield a compact self-assembled aggregate. Consequently the $C_{12}E_6$ tails do not need to orient perpendicularly to the interface until the surface coverage is very large, approaching the value necessary to form a complete monolayer. The different packing of SDS vs. $C_{12}E_6$ surfactants at the interface is probably responsible for differences observed in surface tensions, as discussed below. When SDS and $C_{12}E_6$ surfactants are compared one should remember that the head group of $C_{12}E_6$ is much larger than that of SDS (see Figure 7-8). The head group of SDS may be comparable in size to that of $C_{12}E_3$ (both surfactants yield a complete mono-layer at surface densities of ~40-45 $Å^2$ per surfactant).[219] However, the experimental data reported by Lu et al. show that the

alkyl chain thickness at the air-water interfaces remains ~constant for $C_{12}E_n$ surfactants with n<8 as long as the experiments are performed at the same area per molecule.[235] Thus, the structural properties obtained for the tail groups of $C_{12}E_6$ surfactants should be similar to those obtained for $C_{12}E_3$ ones.

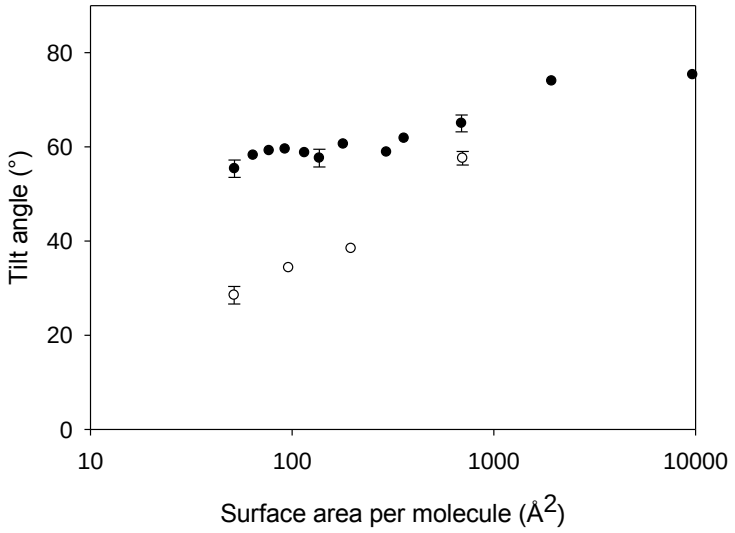

Figure 7-20 Average tilt angles of tail groups as a function of surface area per head group. Filled and empty symbols represent results for $C_{12}E_6$ and SDS, respectively. Only representative error bars are shown for clarity.

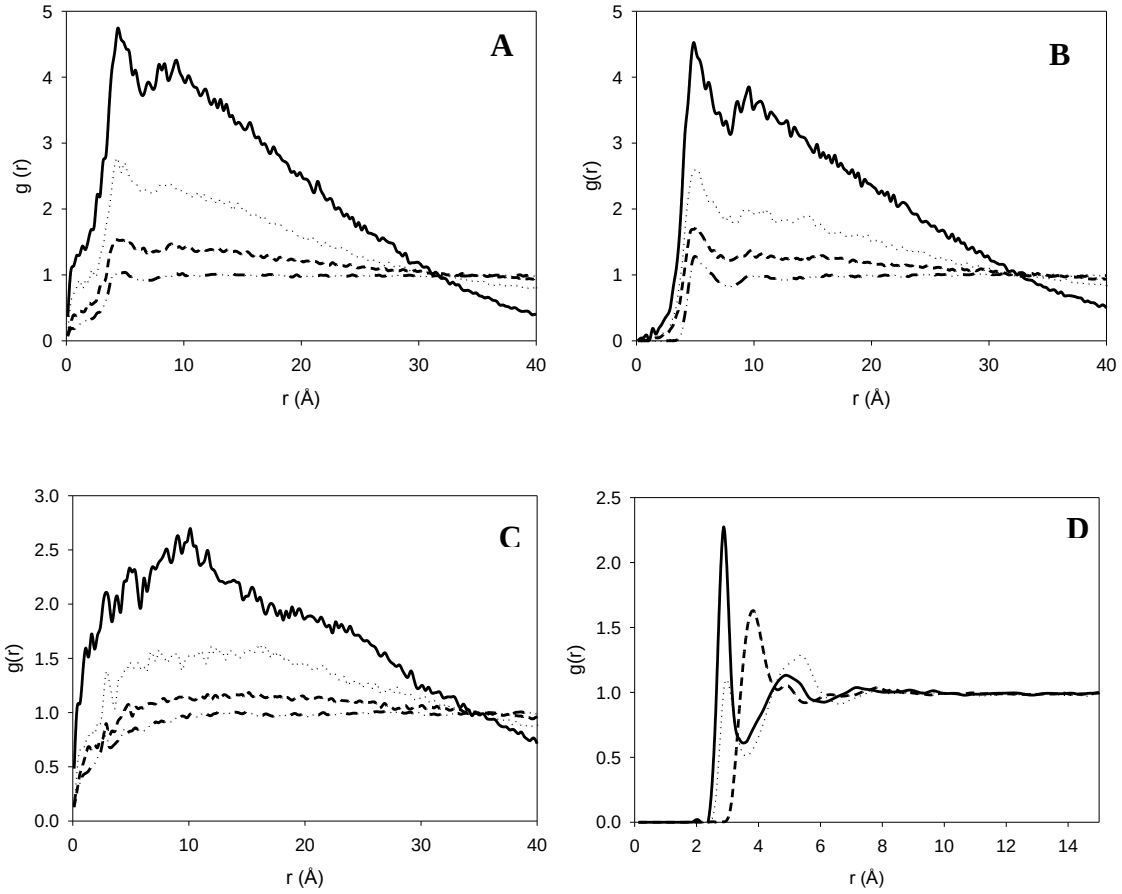

Figure 7-21 Two-dimensional radial distribution functions between surfactants' functional groups at the vacuum-water interface. For clarity, only 3 functional groups are shown: C1-C1 (panel A); EO1-EO1 (panel B) and OH-OH (panel C). See Figure 7-8 for molecular details. Results are obtained at various surface coverages: 293 $Å^2$/molecule (solid line); 179 $Å^2$/molecule (dot line); 92 $Å^2$/molecule (dashed line); and 52 $Å^2$/molecule (dash-dot-dot line). In panel D we report the 2D RDF between $C_{12}E_6$ terminal head groups and the oxygen atom in water at 52 $Å^2$/molecule. Results are shown for OH-water (solid line); EO6-water (dot line); E6-water (dashed line).

B.4.4 Surfactant Aggregates Structure

To quantify the interfacial aggregate morphology we calculated two-dimensional radial distribution functions (2D RDF) between functional groups of $C_{12}E_6$ and SDS surfactants. Representative results obtained as a function of surface coverage are

reported in Figure 7-21. Panels A, B and C report the 2D RDFs for C1-C1, EO1-EO1 and OH-OH groups of interfacial $C_{12}E_6$ aggregates, respectively. At low surface coverage the 2D RDFs are representative of gas-like structures. We also observe that the 2D RDF is less than unity at large distances. This happens because at low surface coverage $C_{12}E_6$ surfactants are not evenly distributed, but rather form small interfacial aggregates (see snapshot in panel A of Figure 7-12). As the surface area per $C_{12}E_6$ decreases (i.e., as the surface coverage increases), the 2D RDFs change from gas-like to condensed-phase-like ones. However, $C_{12}E_6$ aggregates never yield crystalline 2D RDFs, not even at the largest surface coverage considered (52 $Å^2$/molecule). The lack of long-range order in the 2D RDFs shown in Figure 7-21 corroborates our earlier interpretation that region III in Figure 7-16 corresponds to a 2D liquid-like phase. Comparing the 2D RDFs in panel A, B, and C of Figure 7-21 at the largest coverage considered (dot-dot-dash line), we find that the functional groups in the center of the surfactant molecules (EO1-EO1) show 2D RDFs with more intense first peaks than the functional groups at either ends of the surfactants (C1-C1 and OH-OH). This result suggests that the surfactants are relatively closely packed in their middle sections, and quite sparse at their extremities. This is clearly due to the flexibility of the $C_{12}E_6$ surfactants.

To understand why terminal OH groups in $C_{12}E_6$ surfactant do not densely pack, the 2D RDFs between water and terminal OH, EO6 and E6 are shown in panel D of Figure 7-21. For water and terminal OH group only the oxygen atoms are considered. The solid line (water-OH) shows a clear first peak at about 2.8Å, representative of the first hydration shell. The dot line (water-EO6) shows a small peak at the same position,

whose intensity is weaker than that for water-OH. The first peak of the dashed line (water-E6) moves to larger distances due to the hydrophobic nature of ethylene and because of excluded-volume effects. These data are consistent with the formation of a well defined hydration layer around the $C_{12}E_6$ head groups. The hydration layers form easily because the head groups are loosely packed with each other, a consequence of their high flexibility. Our simulations suggest that this hydration layer is in part responsible for preventing the terminal OH groups from densely packing at the interface.

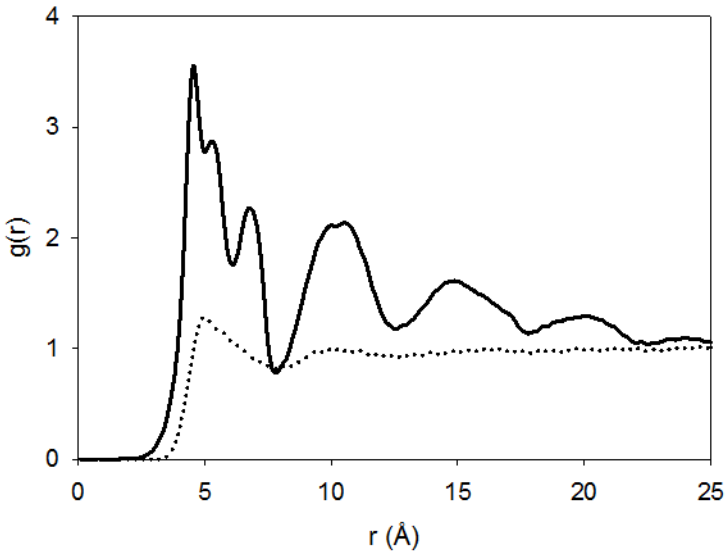

Figure 7-22 Two-dimensional radial distribution functions between head groups of SDS (solid line) and between the EO1 groups of $C_{12}E_6$ surfactants (dot line) at 52 $Å^2$ per head group.

For comparison, we calculated the 2D RDF between sulfur groups of SDS. The results, including those from $C_{12}E_6$, are shown in Figure 7-22. Contrary to what observed for $C_{12}E_6$, the 2D RDF for SDS aggregates shows regular peaks as r increases,

suggesting a more densely packed structure than that obtained with $C_{12}E_6$. The seemingly periodic peaks at 5, 10, 15, and 20 Å suggest a solid-like structure, almost hexagonal (visual inspection of simulation snapshots, not shown for brevity, confirms the formation of a regular structure, but excludes that of a perfect crystalline arrangement). Even though the SDS coverage is not sufficient to form one complete monolayer, the 2D RDF data in Figure 7-22 corroborate the propensity of the SDS head groups to strongly self assemble, because of counter-ion condensation effects.[211] Even though $C_{12}E_3$ has the similar head group size as SDS, the counterion condensation phenomenon responsible for close packing of SDS aggregates is not possible with any $C_{12}E_n$ surfactants, and hence we believe that the intensity of the peak observed for head groups of $C_{12}E_n$ would not be comparable to that observed for SDS head groups.

B.4.5 Surface Tension

The surface tension, γ, was computed from our simulations as:[285]

$$\gamma = (\frac{L_Z}{2})\left[< P_{zz} > -(\frac{< P_{xx} > - < P_{yy} >}{2}) \right] \quad . \tag{7-8}$$

In Eq. 7-8, L_Z is the box size along the direction z, perpendicular to the vacuum-water interface. The factor $1/2$ outside the bracket takes into account the fact that there are two interfaces in the system. $P_{\alpha\alpha}$ are pressure tensors along the α direction.[265] To calculate the surface tension the simulated systems were arranged so that the same number of surfactants was placed on both vacuum-water interfaces (see Figure 7-9). The corresponding surface pressure-area isotherm (π-A) was obtained as:

$$\pi(A) = \gamma_0 - \gamma(A) \quad , \tag{7-9}$$

where γ_0 denotes the surface tension of the vacuum-water interface.

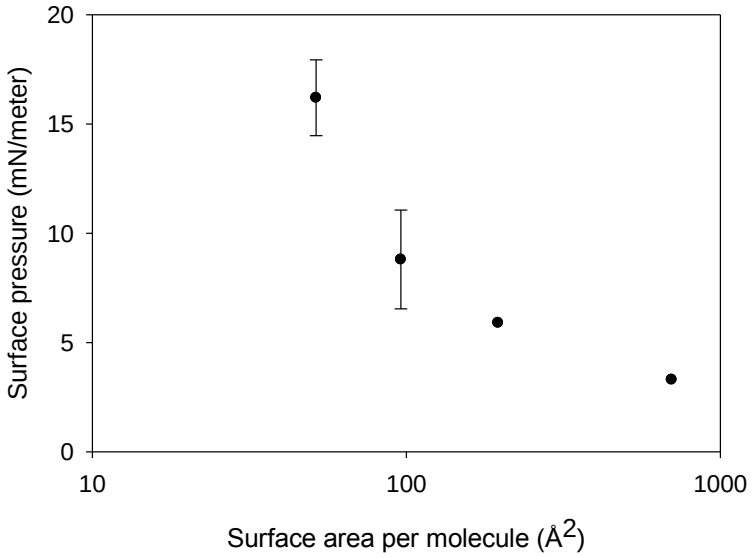

Figure 7-23 Surface pressure as a function of surface area per SDS surfactant.

The results for SDS are shown in Figure 7-23. The surface pressure increases as the surface area per head group decreases, in semi-quantitative agreement with experimental data.[249] On the contrary, our calculation for the surface tension in the presence of $C_{12}E_6$ surfactants showed values only slightly smaller than those obtained at the vacuum-water interface at all surfactant concentrations considered. Although experimental data show that SDS is more effective in reducing the water-air surface tension than $C_{12}E_6$ (surface tension of SDS at cmc is 32.5 mN/m whereas $C_{12}E_6$ yields a value of 41 mN/m),[286, 287] we were expecting to observe a more significant effect for our simulated $C_{12}E_6$ systems than those obtained. One possible reason for the discrepancy between simulated and experimental data could be the size of the simulation box. However, several simulation results are available in the literature that

report data for biological systems and other surfactants that are in good agreement with experiments despite using simulation boxes significantly smaller than those used herein.[262, 265, 266] Prior simulation results showed that appropriately accounting for long-ranged electrostatics is necessary to achieve good agreement between simulated and experimental surface tension data.[265] Because our results for SDS (anionic surfactants) are in good agreement with experiments, and because $C_{12}E_6$ is overall a neutral molecule, it appears that our treatment of long-ranged electrostatics forces is satisfactory. The last possible explanation for the unexpected results for $C_{12}E_6$ is to be found in deficiencies in the implemented force fields. For example, it has been reported previously that although TRaPPE force field parameters yield satisfactory structural and thermodynamic properties, they not always accurately predict interfacial and surface tensions.[285] To test if this was the reason for our unexpected results, we conducted sample simulations in which only the tail groups of $C_{12}E_6$ surfactants (i.e., only dodecane) were simulated at the water-vacuum interface. At surface coverages correspondent to 52 $Å^2$ per dodecane we obtained a ~4% decrease in the surface tension compared to that of the vacuum-water interface, indicating that the TRaPPE force field, used to model the surfactants tails, yields reasonable, yet not always accurate estimates for the surface tension (the NERD force field is known to perform better).[288] On the contrary the force field we implemented to simulate the $C_{12}E_6$ head groups (OPLS, although with some modifications) does not provide good surface tension predictions. We note that the sulfate group parameters used to simulate SDS were fitted to predict the free energy of solvation, along with other thermodynamic properties,[81] while those implemented to describe the $C_{12}E_6$ head groups were fitted to other

thermodynamic properties without explicitly considering solvation.[271] Hence we attribute our failure to reproduce experimental surface tension data for $C_{12}E_6$ systems to inefficiency of the employed force field. Necessary calculations should be performed to increase the accuracy of force fields before any attempts are undertaken to compute the surface tension data for C_mE_n systems.

B.4.6 Surfactant Mobility

To evaluate the surfactant mobility at the vacuum-water interface we calculated the two-dimensional mean square displacement (2D MSD) for surfactants along the plane parallel to the interface.

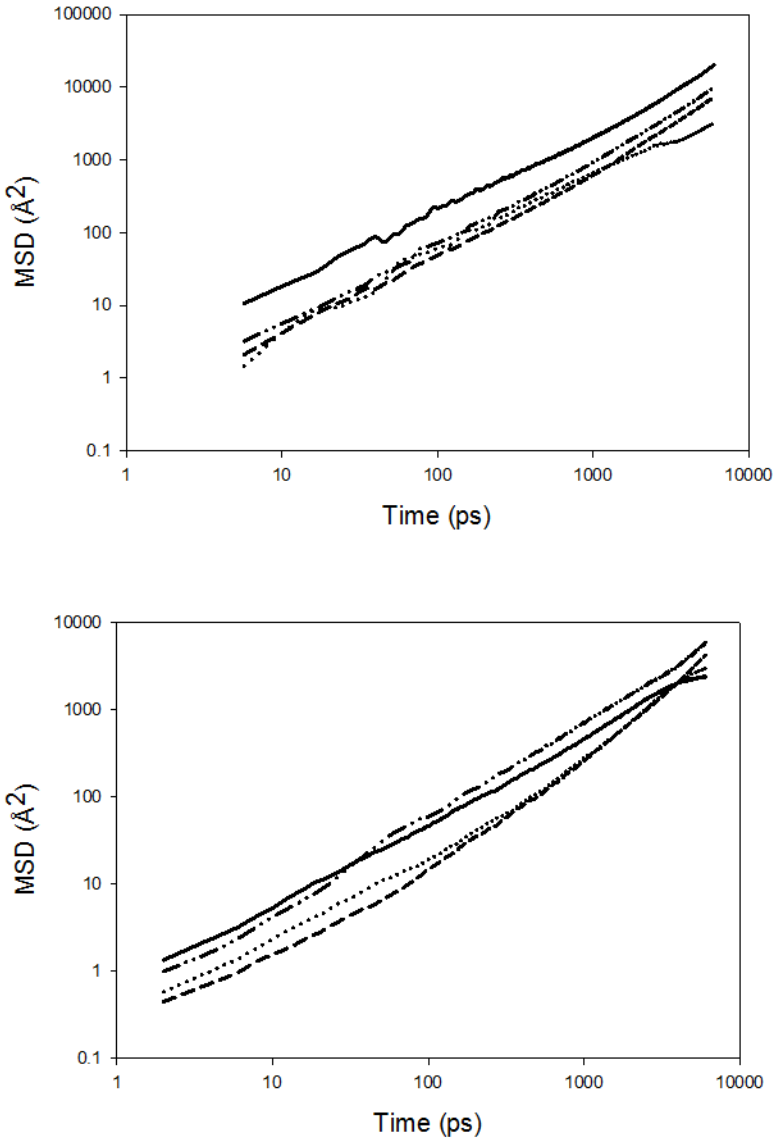

Figure 7-24 Two-dimensional mean square displacement for surfactants as a function of time. The top panel is for $C_{12}E_6$ surfactants at various surface coverages [9684 $Å^2$/molecule (solid line); 358$Å^2$/molecule (dot line); 92$Å^2$/molecule (short dashed line); 52$Å^2$/molecule (dot-dot-dash line)].The bottom panel is for SDS at various coverages [700 $Å^2$/molecule (solid line); 196$Å^2$/molecule (dot line); 96$Å^2$/molecule (dashed line); 52 $Å^2$/molecule (dot-dot-dash line)].

In Figure 7-24 we report the results obtained for $C_{12}E_6$ and SDS surfactants at different surface coverages. Our analysis extends to much longer simulation times and to a wider range of surface coverages compared to previous data reported by Chanda[260] and Bandyopadhyay.[259] Our data suggest that Fickian-type diffusion is established when only 1 surfactant is at the interface, and when a full monolayer is simulated. When the surfactants are simulated at concentrations at which small aggregates form, the diffusion is anomalous because the surfactants are effectively 'confined' within the surface aggregates. More interesting, however, is the fact that the results in the top panel of Figure 7-24 show that at the lowest surface coverage (correspondent to only 1 $C_{12}E_6$ at the interface) the 2D MSD increases more quickly as a function of time than at any other surface coverage considered. These data suggest that the surfactants move on the interface very quickly when they are not associated with other surfactants. As the surfactant aggregates increase in size, each individual surfactant in the aggregate shows slower mobility because the entire aggregate needs to move simultaneously to avoid disaggregation. When the surfactant aggregate is large enough to span the entire interface, then the individual surfactants can easily move within the aggregate and the slope of the 2D MSD as a function of time increases. Our findings are in apparent contradiction with those of Cuny et al.,[257] who reported that the mobility of interfacial surfactants (expressed as the slope of 2D MSD vs. time) does not change as the surface coverage varies. However, we point out that Cuny et al.[257] considered coverages close to those necessary to form a complete surfactant monolayer, whereas we consider surface coverages ranging from very low, to the one necessary to form the complete monolayer. Because at the largest coverage considered here the

results for 2D MSD vs. time are similar to those reported by Cuny et al.,[257] our simulations complement rather than contradict those reported earlier. On the bottom panel of Figure 7-24 we report the data obtained for SDS. Although we do not have data for 1 SDS chain at the surface, the behavior is qualitatively similar to that described for $C_{12}E_6$, suggesting that the properties of the surfactant head groups do not affect significantly the surfactant mobility. Our results seem to suggest that the hydrophobic tails are responsible for the formation of surfactant self-assemblies at the vacuum-water interface, that the hydrophilic head groups determine the morphological properties of the aggregates, and that the size of the self-assembled aggregate is responsible for the mobility of the individual surfactant molecule at the interface.

B.5 Conclusion

We employed MD simulations to characterize the behavior of $C_{12}E_6$ and SDS surfactants at the vacuum-water interface. The aggregate structures of $C_{12}E_6$ at the interface predicted from our simulations are in agreement with data obtained from neutron scattering experiments. Our simulations also indicate that the surfactant structure at the vacuum-water interface strongly depends on the surface density. At high surface area per molecule, the tail groups of $C_{12}E_6$ lie almost parallel to the interface and are located in close proximity to the water phase. At low surface area per molecule, the tail groups remain almost completely segregate from the water phase and show a tilt angle of about 50°. The head groups orient more perpendicularly to the vacuum-water interface than tail groups do at all coverages. At low surface area per head group, not

only the tail groups of $C_{12}E_6$ remain out of the water phase, but also part of the ethylene oxide groups at the center of the surfactant molecules move away from the aqueous phase. The tail groups of SDS are more perpendicular to the vacuum-water interface in comparison with $C_{12}E_6$ ones, and the sulfate head groups of SDS are always immersed in water. An overlap between the interfacial layers formed by head and tail groups is observed for all surface coverages studied for both $C_{12}E_6$ and SDS surfactants, indicating that the surfactant aggregates fluctuate along the direction perpendicular to the interface. Due to these fluctuations the observed thickness of the interfacial surfactant layer is larger than the surfactant end-to-end distance. Due to its long, flexible and partially hydrophobic head groups, the packing of $C_{12}E_6$ head groups is less dense compared to that of SDS head groups.

The surfactants mobility at the vacuum-water interface depends strongly on surface coverage. The mobility is high at infinite dilution, decreases as the surfactant aggregates increase in size, reaches a minimum, and increases when the surface coverage is sufficiently large that the surfactant aggregates cover, albeit with some defects, the entire vacuum-water interface.

Appendix C: Additional Figures

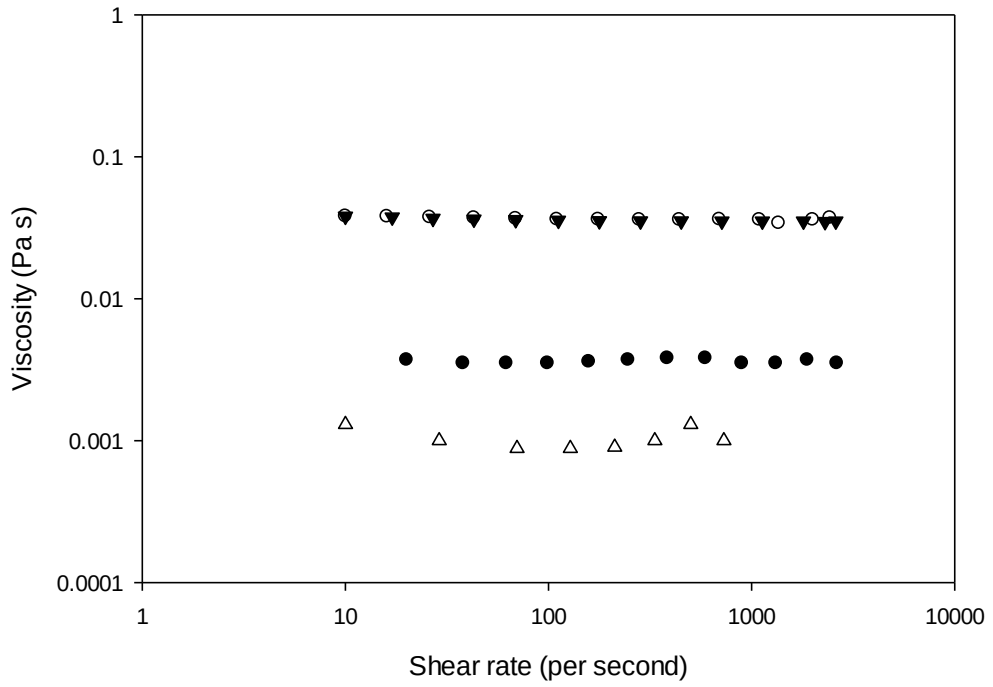

Figure 7-25 Viscosity vs. shear rate of lubricant solutions in section 2. Empty circles are 100mg/ml 100,000 MW PEO solution; black circles are 100mg/ml 10,000 MW PEO solution; black inverse triangles are 100mg/ml CS solution; empty triangles are PBS. Viscosity was measured using a SR5000 stress-controlled rheometer from Rheometric Scientific.

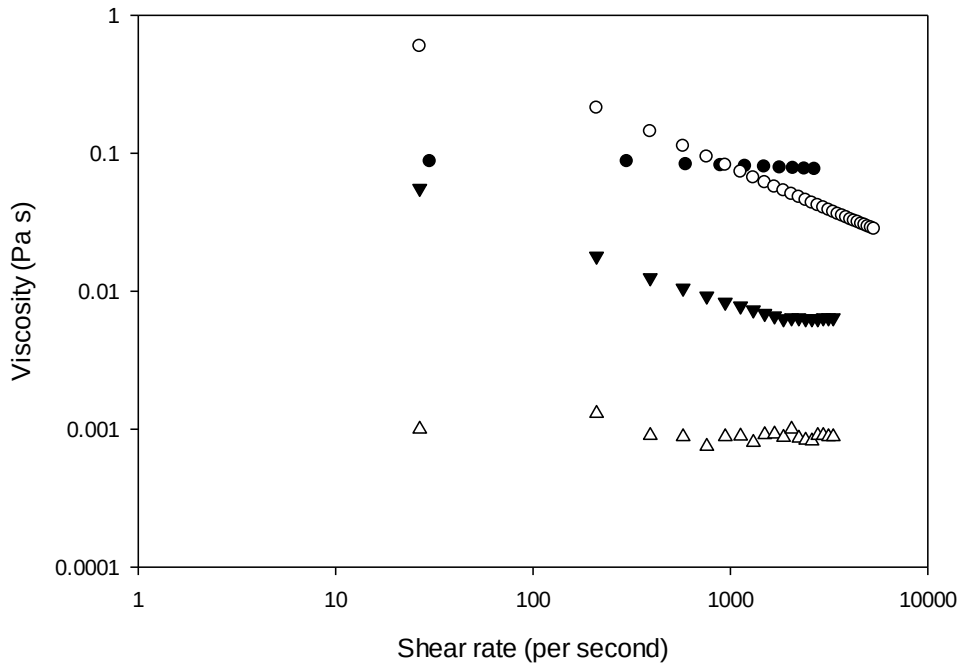

Figure 7-26 Viscosity vs. shear rate of lubricant solutions in section 3. Empty circles are 10mg/ml HA solution; black circles are 100mg/ml 100,000 MW PEO solution; black inverse triangles are SF; empty triangles are PBS. Viscosity was measured using a MERLIN self-contained rotational viscometer (REOLOGICA Instruments, Borden Town, NJ).